

Further evidence for large central mass-to-light ratios in early-type galaxies: the case of ellipticals and lenticulars in the Abell 262 cluster¹

G. A. Wegner²

Department of Physics and Astronomy, 6127 Wilder Laboratory, Dartmouth College, Hanover, NH 03755-3528, USA

E. M. Corsini

Dipartimento di Fisica e Astronomia ‘G. Galilei’, Università di Padova, vicolo dell’Osservatorio 3, 35122 Padova, Italy

INAF–Osservatorio Astronomico di Padova, vicolo dell’Osservatorio 2, 35122 Padova, Italy

J. Thomas

Max-Planck-Institut für extraterrestrische Physik, Giessenbachstraße, D-85748 Garching, Germany

R. P. Saglia

Max-Planck-Institut für extraterrestrische Physik, Giessenbachstraße, D-85748 Garching, Germany

R. Bender

*Max-Planck-Institut für extraterrestrische Physik, Giessenbachstraße, D-85748 Garching, Germany
Universitäts-Sternwarte München, Scheinerstraße 1, D-81679 München, Germany*

S. B. Pu

The Beijing No. 12 High School, No. 15, YiZe Road, FengTai District, 100071 Beijing, China

ABSTRACT

We present new radially resolved spectroscopy of 8 early-type galaxies in the Abell 262 cluster. The measurements include stellar rotation, velocity dispersion, H_3 and H_4 coefficients of the line-of-sight velocity distribution along the major and minor axes and an intermediate axis as well as line-strength index profiles of Mg, Fe and H β . The ionized-gas velocity and velocity dispersion is measured for 6 sample galaxies along different axes. We derive dynamical mass-to-light ratios and dark matter densities from orbit-based dynamical models, complemented by the galaxies’ ages, metallicities, and α -elements abundances from single stellar population models. The ionized-gas kinematics gives a valuable consistency check for the model assumptions about orientation and intrinsic shape of the galaxies. Four galaxies have a significant detection of dark matter and their halos are about 10 times denser than in spirals of the same stellar mass. Calibrating dark matter densities to cosmological simulations we find assembly redshifts $z_{\text{DM}} \approx 1–3$, as previously reported for Coma. The dynamical mass that follows the light is larger than expected for a Kroupa stellar initial mass function (IMF), especially in galaxies with high velocity dispersion σ_{eff} inside the effective radius r_{eff} . This could indicate a ‘massive’ IMF in massive galaxies. Alternatively, some of the dark matter in massive galaxies could follow the light very closely. In combination with our comparison sample of 1 Coma early-type galaxies, we now have 5 of 24 galaxies where (1) mass follows light to $1–3 r_{\text{eff}}$, (2) the dynamical mass-to-light ratio of all the mass that follows the light is large ($\approx 8–10$ in the Kron-Cousins R band), (3) the dark matter fraction is negligible to $1–3 r_{\text{eff}}$. Unless the IMF in these galaxies is particularly ‘massive’ and somehow coupled to the dark matter content, there seems to be a significant degeneracy between

1. Introduction

The distribution of dark matter surrounding elliptical galaxies as well as the dynamical structure of these systems is not known in general. While the dynamical structure contains information about the assembly mechanism of elliptical galaxies, the mass distribution can be used to constrain the assembly epoch. For example, the simple spherical collapse model predicts that the central dark matter density scales with $(1 + z_{\text{DM}})^3$, where z_{DM} is the assembly redshift of the halo. Numerical simulations likewise predict a close relationship between halo concentration and assembly epoch (Wechsler et al. 2002).

Dynamical modeling of stellar kinematics allows the reconstruction of both the orbital structure and the mass distribution in elliptical galaxies, and, thus offers crucial information about when and how elliptical galaxies formed. In the past years we published a series of papers (Thomas et al. 2004, 2005b, 2007b,a, 2009a,b, 2011) studying the distribution of dark matter and the dynamical structure of the elliptical galaxies of the Coma cluster. For the dynamical analysis we employed a refined three-integral axisymmetric orbit superposition code to model the systems of stars in order to determine their mass compositions and orbital structures. For each trial potential on a grid systematically probing a mass component that follows the light (with mass-to-light ratio Υ_*) and different dark matter profiles, we determined an orbit superposition that best matched the kinematic data published by Mehlert et al. (2000), Wegner et al. (2002), and Corsini et al. (2008) with the additional requirement of maximizing the model's entropy. The optimal entropy maximalization and fit to the data were calibrated using Monte-Carlo simulations of observationally motivated galaxy models. These simulations revealed that from typical Coma data, the mass distribution can be reconstructed with an accuracy of $\approx 15\%$. The comparison with the masses derived through strong gravitational

lensing for elliptical galaxies with similar velocity dispersion confirmed this result.

We compared Υ_* to the mass-to-light ratio Υ_{SSP} predicted by the best-fit single stellar population (SSP) models to the line-strength indices as in Mehlert et al. (2003). We found that at face value a Salpeter initial mass function (IMF, Salpeter 1955) gives on average the best agreement between Υ_* and Υ_{SSP} . However, several arguments favor a Kroupa IMF (Kroupa 2001) for the underlying true stellar mass distribution.

We derived dark matter densities for the Coma ellipticals that are on average at least 13 times higher than in spirals of the same stellar mass, consistent with the findings of Gerhard et al. (2001) for round galaxies. We concluded that elliptical galaxy halos have assembled earlier, around $z_{\text{DM}} \approx 1 - 3$. This agrees with the predictions of the semi-analytic galaxy formation models (SAMs) of De Lucia et al. (2006), with simulated ellipticals in a Coma-like cluster environment. Halos form hierarchically – less massive halos first. In contrast, studies on the star formation histories based on line indices (Nelan et al. 2005; Thomas et al. 2005a) show that stars form anti-hierarchically – the least massive galaxies have the youngest stellar populations. This would result from star formation following the hierarchical mass assembly to the time that the available gas is consumed or expelled; early star formation would occur in low-mass systems that subsequently merge forming massive systems and today, low-mass galaxies are generally late-assembling galaxies with younger stellar populations. We found that in a third of our Coma galaxies star-formation and halo assembly redshifts match. The youngest galaxies must have experienced some star-formation after the main halo-assembly epoch – in line with their orbital structure being inconsistent with collisionless N -body mergers with no star formation of disk galaxies (Thomas et al. 2009b).

The Coma cluster represents a high density local cluster sample. In lower-density local environments, the stellar populations of ellipticals are formed at $z_* \leq 1$ (Wegner & Grogin 2008) and have a greater spread of ages – the oldest are about as old as cluster ellipticals, but the youngest are much younger (Collobert et al. 2006). Dark matter densities of ellipticals there are predicted to

²Visiting Astronomer, MDM Observatory, Kitt Peak, Arizona, operated by a consortium of Dartmouth College, the University of Michigan, Columbia University, the Ohio State University, and Ohio University.

¹Based on data collected with the 2.4-m Hiltner Telescope.

be lower, because they assemble later. These predictions need now to be verified by models of real galaxies.

Here we present the new data set we collected for a sample of early-type galaxies of the nearby poor cluster Abell 262. The results of the dynamical analysis we performed are compared to the Coma cluster case. Abell 262 is one of the most conspicuous condensations in the Pisces-Perseus supercluster. The center of the cluster coincides with the position of the cD galaxy NGC 708. Abell 262 is far less densely populated than the Coma cluster and is comparable to the Virgo cluster. Indeed, it falls into richness class 0 (Abell et al. 1989). The cluster redshift of $z = 0.0163$ (Struble & Rood 1999) results in a distance of 70 Mpc, assuming $H_0 = 70 \text{ km s}^{-1} \text{ Mpc}^{-1}$. At this redshift the angular distance $1''$ corresponds to 339 pc. The cluster mass within the virial radius ($R_{\text{vir}} = 1^\circ 52$ corresponding to 1.9 Mpc) and calculated from the line-of-sight velocity dispersion of the cluster galaxies ($\sigma = 548 \pm 35 \text{ km s}^{-1}$) is $M_{\text{vir}} = (2.5 \pm 0.5) \times 10^{14} M_\odot$. It is in agreement with the mass estimated from X-ray data assuming hydrostatic equilibrium (Neill et al. 2001). The low X-ray luminosity (David et al. 1993), low temperature of the hot intracluster medium (Sato et al. 2009) with a complex structure (Clarke et al. 2009), and a central cooling flow (Blanton et al. 2004) are the typical signatures of a less evolved, dynamically young cluster.

The structure of the paper is as follows. In Sec. 2 we present the galaxy sample. We discuss the observations, data reduction and analysis of the imaging dataset in Sec. 3 and of the spectroscopic dataset and the SSP analysis of the line-strength indices in Sec. 4. A summary of the dynamical modeling technique is given in Sec. 5 and a comparison with the gas kinematics and strong gravitational lensing masses follows in Sec. 6. The results are presented in Sec. 7 and the implications discussed in Sec. 8. A summary of the paper follows in Sec. 9.

2. Galaxy sample

All the sample galaxies in Abell 262 were studied within the EFAR (Ellipticals FAR away) project. The latter was aimed at construct-

ing an accurate and homogeneous photometric and spectroscopy database for a large sample of early-type galaxies at redshift between 6000 and 15000 km s^{-1} and distributed in 85 clusters in the Hercules-Corona Borealis and Perseus-Pisces-Cetus regions. Details about the selection of the EFAR galaxy and cluster sample are given by Wegner et al. (1996). Saglia et al. (1997b) and Wegner et al. (1999) presented the photometric and spectroscopic databases, respectively. Results addressed the galaxy structural parameters (Saglia et al. 1997a), the properties of the stellar populations (Colless et al. 1999), the fundamental plane, peculiar velocities, and bulk motions (Saglia et al. 2001; Colless et al. 2001).

The galaxies studied here were selected to be round and classified as early-type (cD, E, and E/S0) in Wegner et al. (1996). Their basic properties which include morphological type, structural parameters, total magnitude, velocity dispersion, and redshift can be found in Table 1.

3. Observations, data reduction, and analysis: imaging

3.1. Observations and data reduction

As part of the HST Snapshot Proposal 10884 (P.I. G. A. Wegner), the galaxies NGC 679, NGC 687, NGC 708, NGC 759, and UGC 1308 were observed with Wide Field Planetary Camera 2 (WFPC2) on board the HST between 2007 July 14 and 2008 September 27. For each galaxy two 300-s exposures were taken with the filter F622W. All exposures were performed with the telescope guiding in fine lock, which typically gave an rms tracking error of $0''.003$. The centers of the galaxies were positioned on the Planetary Camera chip (PC) in order to get the best possible spatial resolution. This consists of 800×800 pixels of $0''.0455 \times 0''.0455$ each, yielding a field of view of about $36'' \times 36''$. The two pointings were shifted along the pixel diagonal by $0''.3535$. This pattern corresponds to a shift of 5.5×5.5 pixels on the PC chip.

In the following our photometric analysis is limited to the PC chip, since the nuclear surface brightness profiles were matched to available radially extended ground-based photometry. Indeed, all the sample galaxies were observed in the R band of the Kron-Cousins system as a part of the

Table 1: Properties of the sample galaxies

Object (1)	Alt. Name (2)	Type (3)	r_{eff} (arcsec) (4)	$\langle \mu \rangle_{\text{eff}}$ (mag arcsec $^{-1}$) (5)	R_T (mag) (6)	P.A. ($^{\circ}$) (7)	cz (km s $^{-1}$) (8)	σ (km s $^{-1}$) (9)	d (Mpc) (10)
IC 171	Abell 262 E	E	30.31	20.47	11.16	108	5346	178	1.22
NGC 679	Abell 262 D	E	10.37	18.80	11.79	85	5036	229	0.88
NGC 687	Abell 262 C	E/S0	12.79	19.19	11.74	...	5086	224	0.61
NGC 703	Abell 262 I	E/S0	9.41	19.45	12.65	47	5584	180	0.04
NGC 708	Abell 262 A	cD	33.03	21.00	11.48	39	4845	194	0
NGC 712	Abell 262 F	E/S0	10.31	19.18	12.19	83	5330	221	0.82
NGC 759	Abell 262 G	E/S0	16.24	19.72	11.74	...	4644	241	1.27
UGC 1308	Abell 262 B	E	23.88	19.44	10.63	140	5227	216	0.50

NOTE.—Col. 1: Name. Col. 2: Alternative name from Wegner et al. (1996). Col. 3: Morphological type from Wegner et al. (1996). In spite of the cD classification, the properties of NGC 708 are not particularly extreme with respect to the other Abell 262 galaxies listed here. Col. 4: Effective radius obtained by Saglia et al. (1997b) in the Kron-Cousins R band. Col. 5: Average surface brightness within the effective radius obtained by Saglia et al. (1997b) in the Kron-Cousins R band after applying the Galactic absorption, K_R , and cosmological dimming corrections. Col. 6: Total magnitude measured by Saglia et al. (1997b) in the Kron-Cousins R band after applying the Galactic absorption and K_R corrections. Col. 7: Major-axis position angle measured North through East from HyperLeda catalog (Paturel et al. 2003). Col. 8: Heliocentric systemic velocity from Wegner et al. (1999). Col. 9: Velocity dispersion measured by Wegner et al. (1999) after applying the correction to the standard metric aperture of 0.54 h^{-1} kpc in radius. Col. 10: Projected distance from NGC 708.

EFAR project (Colless et al. 1993; Saglia et al. 1997b).

The WFPC2 images were reduced using the CalWFPC reduction pipeline in IRAF² maintained by the Space Telescope Science Institute. Reduction steps include bias subtraction, dark current subtraction, and flat-fielding, as described in detail in the WFPC2 instrument and data handbooks (Baggett & McMaster 2002; McMaster & Biretta 2008). Subsequent analysis was performed using IRAF standard tasks. The bad pixels were corrected by means of a linear one-dimensional interpolation using the data quality files and the WFIXUP task. For each galaxy, the alignment of the images was checked by comparing the centroids of stars in the field of view. The images were aligned to an accuracy of a few hundredths of a pixel using IMSHIFT and knowledge of the offsets. They were then combined with IMCOMBINE. A check was done to verify that the alignment and combination did not introduce a significant blurring of the data. To this aim,

the full-width at half maximum (FWHM) of the Gaussian fitting to the field stars was measured in the original and combined frames. It was found that they did not change to within a few percent. In combining the images, pixels deviating by more than three times the local standard deviation (calculated from the combined effect of Poisson and read-out noise) were flagged as cosmic rays and rejected. The residual cosmic rays and bad pixels were corrected by manually editing the resulting image with IMEDIT.

3.2. Isophotal analysis

The reduced EFAR images were available to one of us (RPS). To calibrate the images the photometric zero-points in Saglia et al. (1997b) were adopted and their coefficients were applied to correct the measured magnitudes for Galactic absorption and K_R correction and to correct the measured surface brightnesses for Galactic absorption, K_R correction, and cosmological dimming. The EFAR images were used to determine the zero-points and calibrate the WFPC2 images.

To this aim, the isophotal profiles of the galaxies were measured by fitting the isophotes in the WFPC2 and EFAR images with ellipses using the isophotal shape algorithm described by

²Imaging Reduction and Analysis Facilities (IRAF) is distributed by the National Optical Astronomy Observatories which are operated by the Association of Universities for Research in Astronomy (AURA) under cooperative agreement with the National Science Foundation.

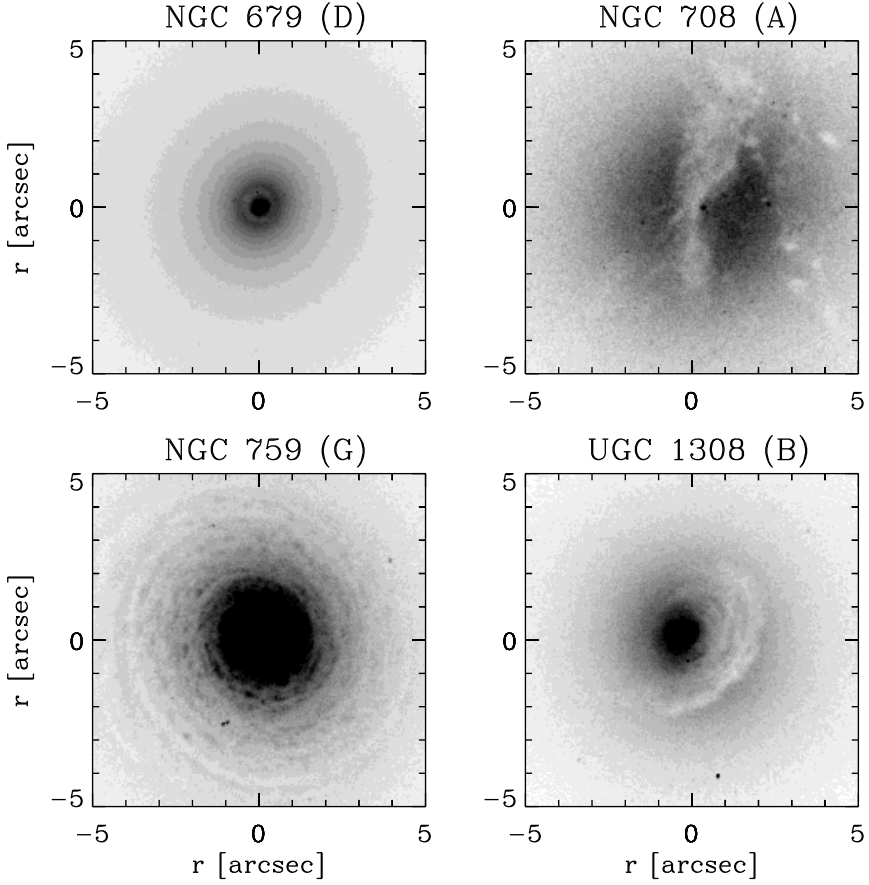


Fig. 1.— Central portions of HST WFPC2/F622W images of the galaxies showing dust features. Each frame uses a negative intensity scale and North is at the top with East to the left.

Bender & Moellenhoff (1987). For the fitted isophotes the algorithm provides the azimuthally-averaged surface brightness (μ), ellipticity (ϵ), position angle (P.A.), center coordinates (x_0, y_0) and third, fourth, and sixth cosine (a_3, a_4 , and a_6) and sine (b_3, b_4 , and b_6) Fourier coefficients describing the deviation of isophotal shape from perfect ellipse. Foreground stars, residual cosmic rays, and bad pixels were masked before fitting. Moreover, the centers of ellipses were allowed to vary. As a first step, the sky background was measured in regions free of sources at the edges of the field of view and then subtracted. Its final value in the WFPC2 images was determined through the matching of the ground-based photometry.

The surface-brightness radial profiles measured in the WFPC2 images were matched to the EFAR ones typically between $3''$ and $10''$ by determining the zero-point and sky value that minimize the surface-brightness flux differences. The galaxies were assumed to have no $R - m_{\text{F622W}}$ color gradient in the matched radial region. The resulting distribution of the differences $\Delta m = R - m_{\text{F622W}}$ after minimization gives a standard deviation about the mean $\sigma_{\Delta m} = 0.035$ mag for NGC 679, $\sigma_{\Delta m} = 0.017$ mag for NGC 687, and $\sigma_{\Delta m} = 0.050$ mag for UGC 1308. Therefore, the scatter $\sigma_{\Delta m}$ is the dominant source of error in the zero-point of the WFPC2 images, because the EFAR final data set has a common zero-point to

better than 0.01 mag (Saglia et al. 1997b).

The prominent dust lanes crossing the nucleus of NGC 708 (Fig. 1) did not allow us to measure reliable isophotal parameters within a few arcsecs from the galaxy center in both the WFPC2 and EFAR images. To minimize the impact of dust on the measurement of the isophote shape, we analyzed the H -band image obtained by Gavazzi et al. (1996), retrieved from the GOLD-Mine Archive (Gavazzi et al. 2003). The near-infrared data were taken on 1995 February 13 at Calar Alto Observatory, Spain. The 2.2-m telescope mounted the Max-Planck-Institut für Astronomie General-purpose Infrared Camera (MAGIC) with a Rockwell 256×256 NICMOS3 HgCdTe detector array. The spatial scale was $1''.61 \text{ pixel}^{-1}$ yielding a field of view of $6''.8 \times 6''.8$. The total exposure times was 192 s. A two-dimensional fit with a circular Gaussian to the field stars in the resulting image yielded a FWHM = $2''.2$. The surface-brightness radial profiles measured in the GOLDMine and EFAR images were matched between $5''$ and $26''$ with $\langle \Delta m \rangle = +0.006$ mag and $\sigma_{\Delta m} = 0.026$ mag.

For NGC 679, NGC 687, NGC 759, and UGC 1308, the position angles measured in the available HST and ground-based available images match within 2° , ellipticities within less than 0.05, cosine and sine Fourier coefficients within less than 1%, and center coordinates of the fitting ellipses within $0''.2$.

The radial profiles of the azimuthally averaged surface brightness, ellipticity, position angle, center coordinates and third, fourth, and sixth cosine and sine Fourier coefficients of the sample galaxies are presented in Fig. 2 and Table 5. For NGC 679, NGC 687, NGC 759, and UGC 1308 they are the combination of HST and EFAR data. For NGC 708 they are measured on the GOLD-Mine image. For IC 171, NGC 703, and NGC 712 they are obtained from the EFAR images.

3.3. Morphologies of the galaxies with dust

Classed as early-type galaxies on ground-based data (Wegner et al. 1996, but see also de Vaucouleurs et al. 1991), the HST images show that four of the galaxies in this investigation, NGC 679, NGC 708, UGC 1308, and NGC 759,

have absorbing material in their central regions. The images are shown in Fig. 1. These resemble the dust features described elsewhere (e.g., Martini et al. 2003; Lauer et al. 2005) and found in two of our Coma cluster galaxies (Corsini et al. 2008). Only NGC 687 shows no dust features in its nucleus.

NGC 679. The nucleus of the galaxy hosts a nearly face-on ring of dust. It has a radius of $4''.5$ (1.5 kpc).

NGC 708. The strong dark stripe of NGC 708 appears to be consistent with a dust disk seen nearly edge-on as it runs roughly North-South through the center of the galaxy image. It extends out to $3''.2$ (1.1 kpc) on its South side and $5''.8$ (2.0 kpc) on the North side. Individual dark blobs can be seen along the edge of the band, particularly to the West side.

NGC 759. The galaxy has a nuclear dusty disk which is close to being face-on. It has a radius of $5''.0$ (1.7 kpc) and it is characterized by tightly wound multiple spiral arms.

UGC 1308. The galaxy nucleus appears to have an inclined dust disk. The projected elliptical shape has a major axis of $3''.2$ (1.1 kpc) across in the North-South direction and minor axis $2''.6$ (0.9 kpc). It is asymmetric in that it is stronger on the West side and is not present on the East side.

4. Observations, data reduction, and analysis: spectroscopy

4.1. Observations and data reduction

Long-slit spectroscopic data of the sample galaxies were obtained with the 2.4-m Hiltner telescope of the MDM Observatory at Kitt Peak, Arizona on 2003 November 14-23 (run 1), 2005 October 25-31 (run 2), and 2006 November 10-16 (run 3).

In runs 1 and 2 the telescope mounted the Moderate Resolution Spectrograph with a plane reflection grating with $1200 \text{ grooves mm}^{-1}$ blazed at 5000 \AA at the first order and a $1''.9 \times 9''.6$ slit. The “Echelle” CCD was adopted as detector. It is a thinned and backside illuminated Site CCD

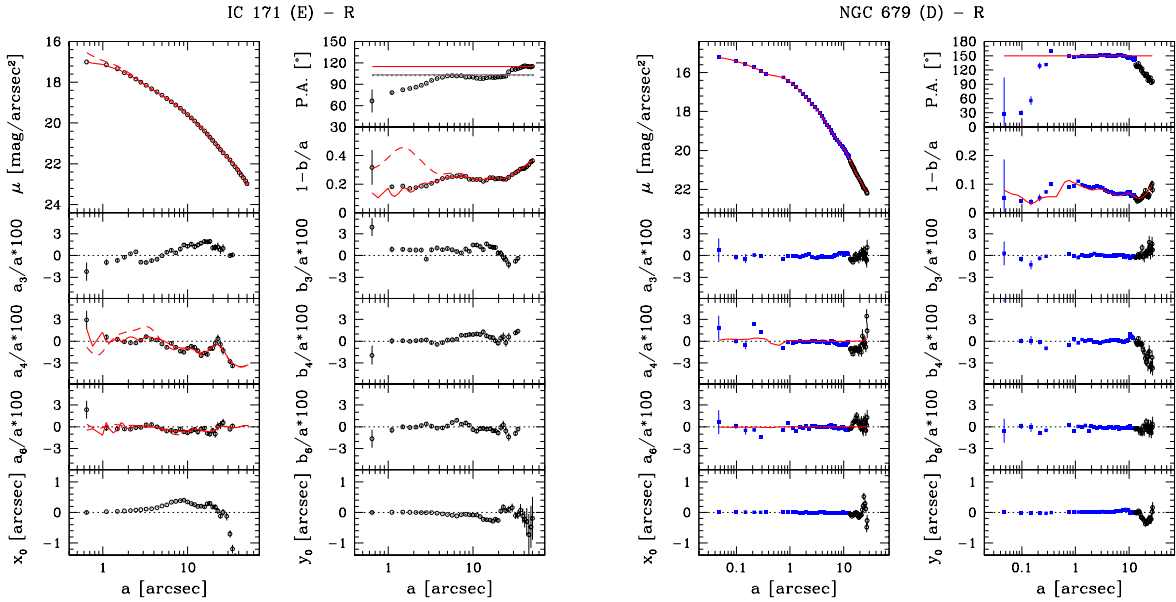


Fig. 2.— Isophotal parameters of the galaxies from ground-based (black open circles) and HST/WFPC2 images (blue filled squares) as a function of the logarithm of the semi-major axis distance in arcsec. The radial profiles of Kron-Cousins R -band surface brightness (μ), third, fourth, and sixth cosine Fourier coefficients (a_3 , a_4 , and a_6), and x -coordinate of the center (x_0) are plotted in the left panels (from top to bottom). The radial profiles of position angle (P.A.), ellipticity ($1 - b/a$), third, fourth, and sixth sine Fourier coefficients (b_3 , b_4 , and b_6), and y -coordinate of the center (y_0), are plotted in the right panels (from top to bottom). For galaxies with only ground-based photometry, the solid and dashed red lines correspond to the surface brightness, ellipticity, a_4 , and a_6 profiles obtained by projecting the deprojected stellar luminosity density with and without the correction for seeing convolution, respectively. For the remaining galaxies, the solid red lines are obtained by projecting the stellar luminosity density without the correction for seeing convolution. The solid grey line corresponds to the galaxy position angle (P.A._{gas}) derived by minimizing the difference between the rotation velocity of the ionized gas and the circular velocity from the dynamical model (see Sec. 6.2 for details). The grey dotted lines delimit the 68% confidence region for P.A._{gas}.

with 2048×2048 pixels of $24 \times 24 \mu\text{m}^2$. The gain and read-out noise are $2.7 \text{ e}^- \text{ ADU}^{-1}$ and 7.9 e^- (rms), respectively. In run 3 the Boller & Chivens CCD Spectrograph was mounted with a plane reflection grating with 600 grooves mm $^{-1}$ blazed at 5875 Å in the second order. A $1.^{\prime\prime}7 \times 5.^{\prime}2$ slit with a LG370 order blocking filter was used. The “Ohio State University Loral C” CCD was the detector. The latter is a thinned and backside illuminated Loral CCD with 1200×800 pixels of $15 \times 15 \mu\text{m}^2$. The gain and read-out noise are $2.1 \text{ e}^- \text{ ADU}^{-1}$ and 7.0 e^- (rms), respectively. No pixel binning was adopted. The wavelength range from 4670 to 6541 Å was covered with a reciprocal dispersion of $0.870 \text{ \AA pixel}^{-1}$ in run 1, from 4675 to 6530 Å

with $0.906 \text{ \AA pixel}^{-1}$ in run 2, and from 6270 to 7175 Å with $0.755 \text{ \AA pixel}^{-1}$ in run 3. The spatial scale was $0.^{\prime\prime}606 \text{ pixel}^{-1}$ in runs 1 and 2, and $0.^{\prime\prime}41 \text{ pixel}^{-1}$ in run 3.

In runs 1 and 2 the spectra were obtained along the major, minor, and a diagonal axis for all the sample galaxies, except for UGC 1308 which was observed only along the major and minor axis. The major axis of IC 171 and NGC 679 and the minor axis of UGC 1308 were observed in both runs to perform a consistency check between the measurements of stellar kinematics and line-strength indices of the two runs. In run 3 the spectra were obtained along a diagonal axis. Only NGC 708 was also observed also along the major and minor

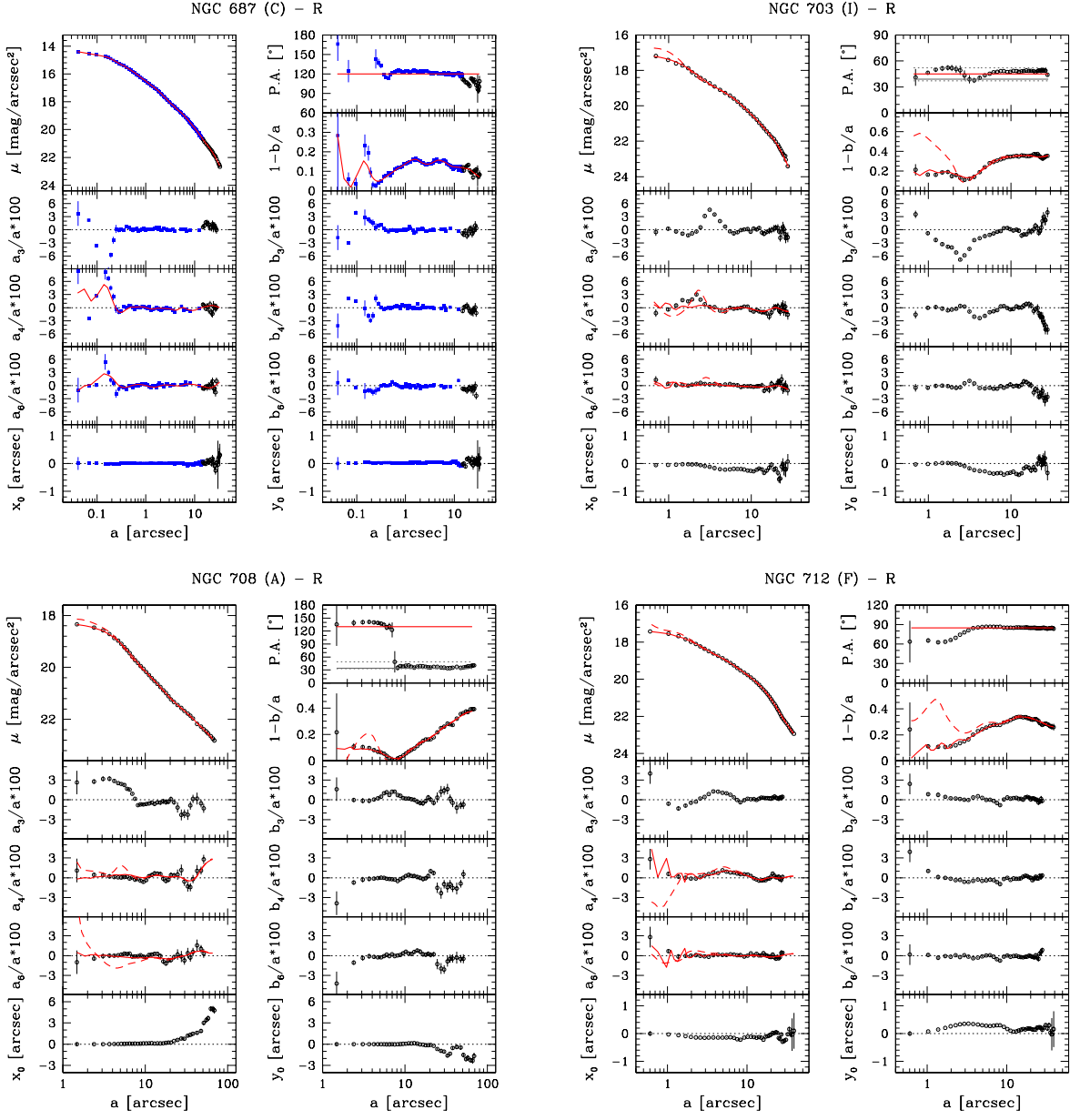


Fig. 2.— *Continued.*

axes. For NGC 759 the spectra were also taken close to the major axis and along the minor axis. The integration time of the single galaxy spectra was 3600 s in runs 1 and 2 and 1800 s in run 3. Total integration times and slit position angle of the galaxy spectra as well as the log of the spectroscopic observations are given in Table 2.

At the beginning of each exposure the galaxy was centered on the slit using the guiding camera which looks onto the slit. In runs 1 and 2 several spectra of giant stars with spectral type ranging from late-G to early-K were obtained for templates in measuring stellar kinematics and line-strength indices. The template stars were selected

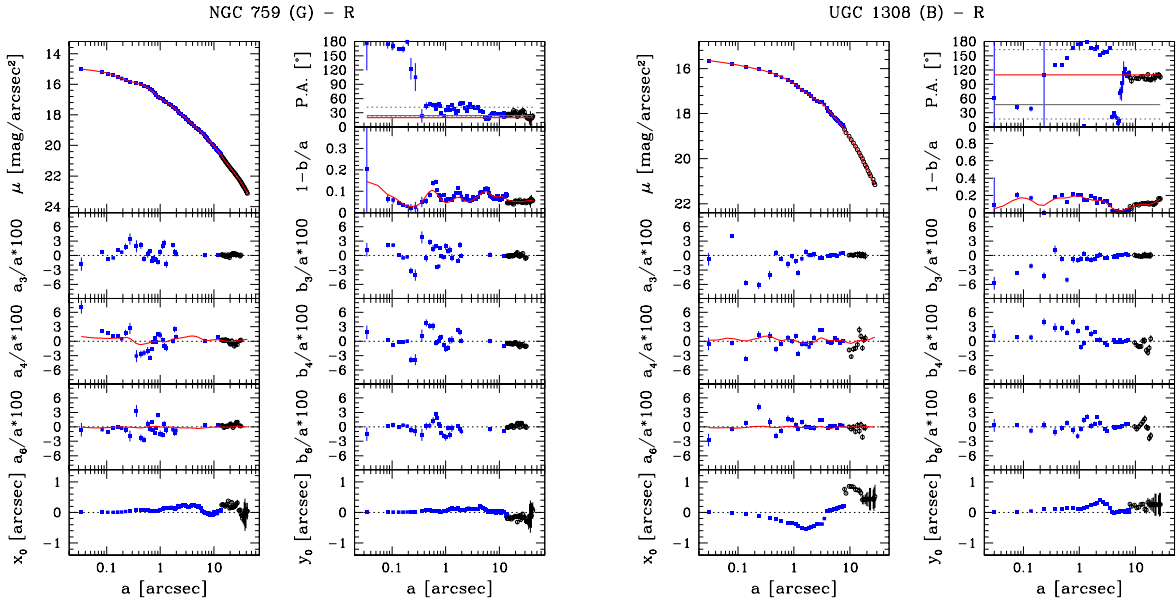


Fig. 2.— *Continued.*

from Faber et al. (1985) and González (1993). At least one flux standard star per night was observed to calibrate the flux of the spectra before line-strength indices were measured. Spectra of the comparison arc lamp were taken before and/or after object exposures.

All the spectra were bias subtracted, flat-field corrected, cleaned of cosmic rays, corrected for bad columns and wavelength and flux calibrated using standard IRAF routines. Each spectrum was rebinned using the wavelength solution obtained from the corresponding arc-lamp spectrum. The difference between the measured and predicted wavelengths in the comparison arc lamp spectra have a rms of 0.05 Å, corresponding to 3 km s⁻¹ at 5170 Å (i.e., the wavelength of the Mg I absorption triplet) in runs 1 and 2 and 2 km s⁻¹ at H α in run 3. Systematic errors of the absolute wavelength calibration (≤ 10 km s⁻¹) were estimated from the brightest night-sky emission lines in the observed spectral range (Osterbrock et al. 1996). The instrumental resolution in each run was derived as the mean of the Gaussian FWHMs measured for a number of unblended arc-lamp lines which were distributed over the whole spectral range of a wavelength-calibrated spectrum. The mean FWHM of the

arc-lamp lines was 2.3 Å in run 1 and 2.4 Å in run 2 and the corresponding instrumental resolution derived at 5170 Å is $\sigma_{\text{inst}} \simeq 60$ km s⁻¹. In run 3 the mean FWHM was 3.2 Å corresponding to $\sigma_{\text{inst}} \simeq 60$ km s⁻¹ at H α . All the galaxy and stellar spectra were corrected for CCD misalignment. The sky contribution was determined by interpolating along the outermost 10'' – 30'' at the two edges of the slit, where the galaxy or stellar light was negligible, and then subtracted. A sky subtraction better than 1% was achieved. Each spectrum was flux calibrated using the sensitivity function obtained from the flux standard star spectrum of the corresponding night. In each run the spectra obtained for the same galaxy along the same axis were coadded using the center of the stellar continuum as reference, thus improving the signal-to-noise ratio (S/N) of the final two-dimensional spectrum. The spectra of the template stars were deredshifted to laboratory wavelengths.

4.2. Stellar kinematics

The stellar kinematics of the galaxies was measured from the galaxy absorption features present in the wavelength range and centered on the Mg I line triplet ($\lambda\lambda 5164, 5173, 5184$

Table 2: Log of the spectroscopic observations

Object	Run	P.A. ($^{\circ}$)	Position	Single Exp. Time (s)	Total Exp. Time (h)	Q
(1)	(2)	(3)	(4)	(5)	(6)	(7)
IC 171 (E)	3	0	DG	3 \times 1800	1.5	4
	2	10	DG	3 \times 3600	3.0	2
	1	110	MJ	4 \times 3600	4.0	2
	2	110	MJ	1 \times 3600	1.0	2
	2	145	DG	3 \times 3600	3.0	2
NGC 679 (D)	1	0	DG	3 \times 3600	3.0	1
	2	0	DG	1 \times 3600	1.0	1
	3	0	DG	2 \times 1800	1.0	4
	2	90	DG	3 \times 3600	3.0	2
	2	135	MJ	4 \times 3600	4.0	2
NGC 687 (C)	1	0	DG	3 \times 3600	3.0	1
	3	0	DG	2 \times 1800	1.0	4
	2	20	MN	3 \times 3600	3.0	1
	2	110	MJ	3 \times 3600	3.0	1
NGC 703 (I)	2	0	DG	3 \times 3600	3.0	2
	3	0	DG	2 \times 1800	1.0	4
	1	45	MJ	3 \times 3600	3.0	1
	2	135	MN	4 \times 3600	4.0	2
NGC 708 (A)	1	0	DG	1 \times 3600	1.0	3
	3	0	DG	3 \times 1800	1.5	3
	2	40	MN	3 \times 3600	3.0	3
	3	40	MN	3 \times 1800	1.5	4
	2	130	MJ	3 \times 3600	3.0	2
NGC 712 (F)	3	0	DG	3 \times 1800	1.5	4
	1	95	MJ	3 \times 3600	3.0	2
	2	125	DG	3 \times 3600	3.0	2
	2	170	MN	4 \times 3600	4.0	2
NGC 759 (G)	3	0	DG	3 \times 1800	1.5	4
	1	11	MJ	3 \times 3600	3.0	1
	2	100	MN	3 \times 3600	3.0	2
	3	100	MN	3 \times 1800	1.5	4
	2	145	DG	3 \times 3600	3.0	2
UGC 1308 (B)	3	0	DG	3 \times 1800	1.5	4
	1	28	MN	3 \times 3600	3.0	2
	2	28	MN	2 \times 3600	2.0	3
	2	120	MJ	3 \times 3600	3.0	2

NOTE.—Col. 1: Name. Col. 2: Observing run. Col. 3: Slit position angle measured North through East. Col. 4: Slit position. MJ = major axis (or close to the major axis); MN = minor axis (or close to the minor axis); DG = diagonal axis. Col. 5: Number and exposure time of the single exposures. Col. 6: Total exposure time. Col. 7: Estimated quality of the resulting spectrum. 1: excellent; 2: very good; 3: good; 4: fair (see Fig. 3).

\AA) using the Penalized Pixel-Fitting (pPXF, Cappellari & Emsellem 2004) and Gas and Absorption Line Fitting (GANDALF, Sarzi et al. 2006) IDL³ codes adapted for dealing with MDM spectra.

The spectra of runs 1 and 2 were rebinned along the dispersion direction to a logarithmic scale, and along the spatial direction to obtain a $S/N \geq 40$ per resolution element. It decreases to $S/N \approx 20$ per resolution element at the outermost radii. The quality of the final spectrum depends on the resulting S/N . Examples of central spectra obtained in runs 1 and 2 covering the quality classes listed in Table 2 are shown in Fig. 3. The quality parameter is 1 for $S/N \geq 100$ per resolution element, 2 for $50 \leq S/N < 100$, and 3 for $30 \leq S/N < 50$.

At each radius a linear combination of template stellar spectra from the empirical library by Sánchez-Blázquez et al. (2006, i.e., the MILES library) was convolved with the line-of-sight velocity distribution (LOSVD) and fitted to the observed galaxy spectrum by χ^2 minimization in pixel space. The LOSVD was assumed to be a Gaussian plus third- and fourth-order Gauss-Hermite polynomials \mathcal{H}_3 and \mathcal{H}_4 , which describe the asymmetric and symmetric deviations of the LOSVD from a pure Gaussian profile (van der Marel & Franx 1993; Gerhard 1993). This allowed us to derive profiles of the line-of-sight velocity (v), velocity dispersion (σ), and third- (H_3) and fourth-order (H_4) Gauss-Hermite moments of the stars.

The galaxy spectra were convolved with a Gaussian function to match the MILES spectral resolution (FWHM=2.5 \AA , Beifiori et al. 2010). Bad pixels coming from imperfect subtraction of cosmic rays and sky emission lines were properly masked and excluded from the fitting procedure. Ionized-gas emission lines were simultaneously fitted and a fourth-order additive Legendre polynomial was added to correct for the different shape of the continuum in the galaxy and template spectra.

The uncertainties on the kinematic parameters were estimated by Monte Carlo simulations. The simulated spectra were obtained by convolving the template spectra with a LOSVD parametrized as a Gauss-Hermite series and adding photon, readout,

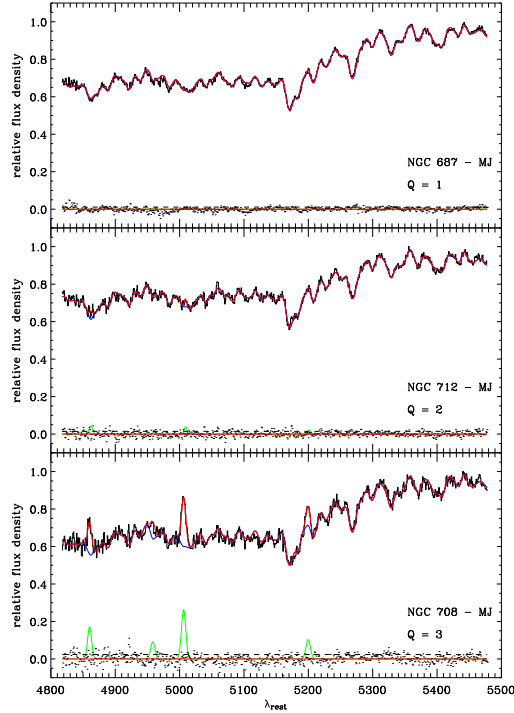


Fig. 3.— Example of central spectra covering the range of quality classes of runs 1 and 2. Relative fluxes have false zero points for viewing convenience. In each panel the best-fitting model (red line) is the sum of the spectra of the ionized-gas (green line) and stellar component (blue line). The latter is obtained convolving the synthetic templates with the best-fitting LOSVD and multiplying them by the best-fitting Legendre polynomials. The residuals (dots) are obtained by subtracting the model from the spectrum. The dashed line corresponds to the rms of the residuals.

and sky noise. The simulated spectra were measured as if they were real. Extensive testing was performed to provide an estimate of the biases of the pPXF method with the adopted instrumental setup and spectral sampling. No bias was found in the ranges of S/N and σ which characterize the spectra of the sample galaxies. The values of H_3 and H_4 measured for the simulated spectra differ from the intrinsic ones only within the measured errors.

The measured stellar kinematics is reported in Table 6 where velocities are relative to the galaxy

³The Interactive Data Language is distributed by ITT Visual Information Solutions.

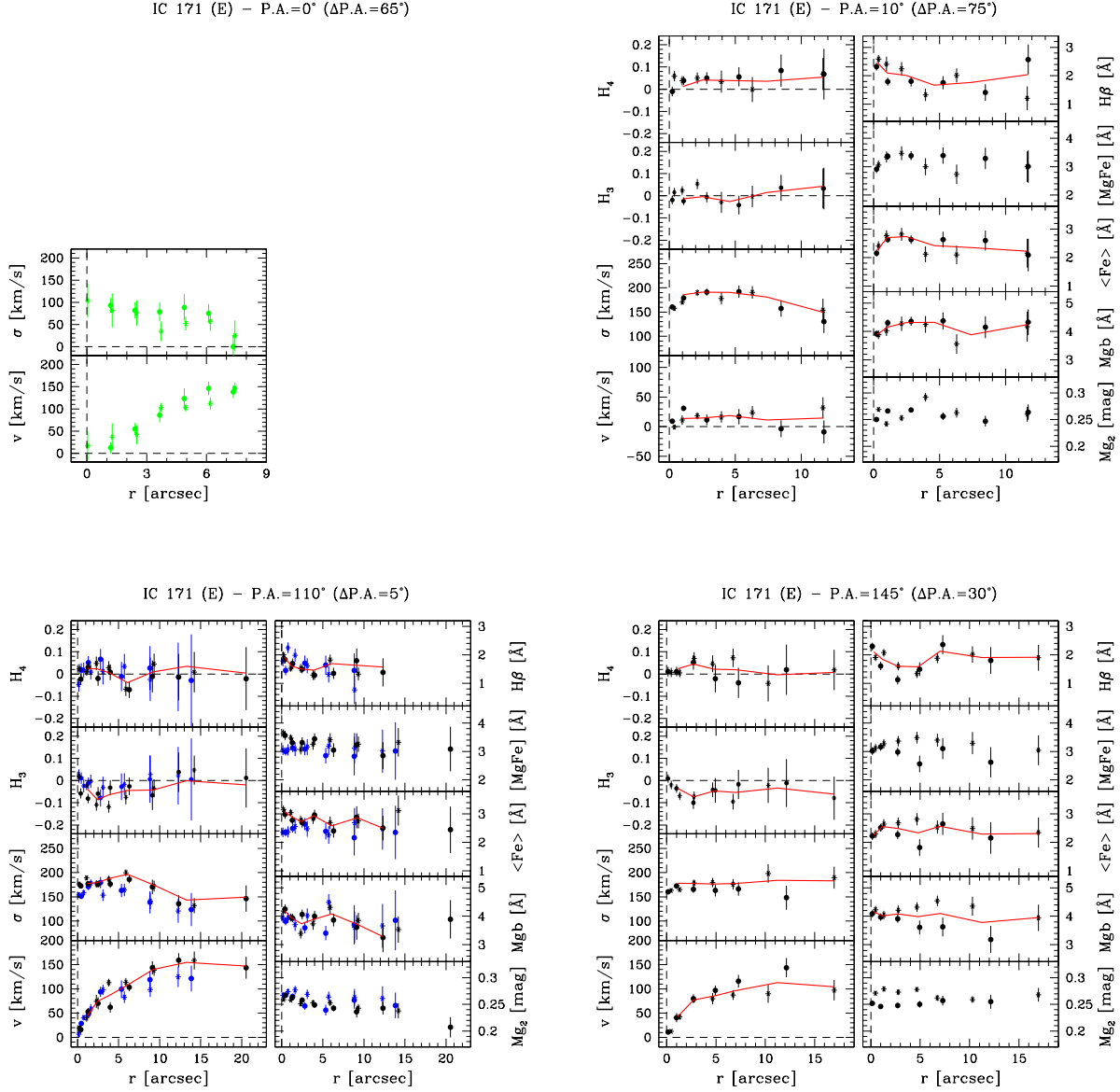


Fig. 4.— Kinematic parameters of the stars (run 1: black symbols; run 2: blue symbols) and ionized gas (run 3: green symbols) and the line-strength indices measured along the observed axes of the sample galaxies. For each axis the curves are folded around the nucleus. Circles and asterisks (or squares) refer to data measured along the receding and approaching side, respectively. The radial profiles of the line-of-sight velocity (v) after the subtraction of systemic velocity, velocity dispersion (σ), third, and fourth order coefficient of the Gauss-Hermite decomposition of the LOSVD (H_3 and H_4) are shown in the left panels (from top to bottom). The red solid lines correspond to the stellar kinematic parameters of the best fitting dynamical model. The difference between the position angle of the observed axis and that adopted in the dynamical model for the galaxy line of nodes (Table 4) is given in the top label (Δ P.A.). The radial profiles of the line-strength indices $H\beta$, $[MgFe]$, $\langle Fe \rangle$, Mgb , and Mg_2 are plotted in the right panels (from top to bottom). The red solid lines correspond to the line-strength indices derived from SSP models.

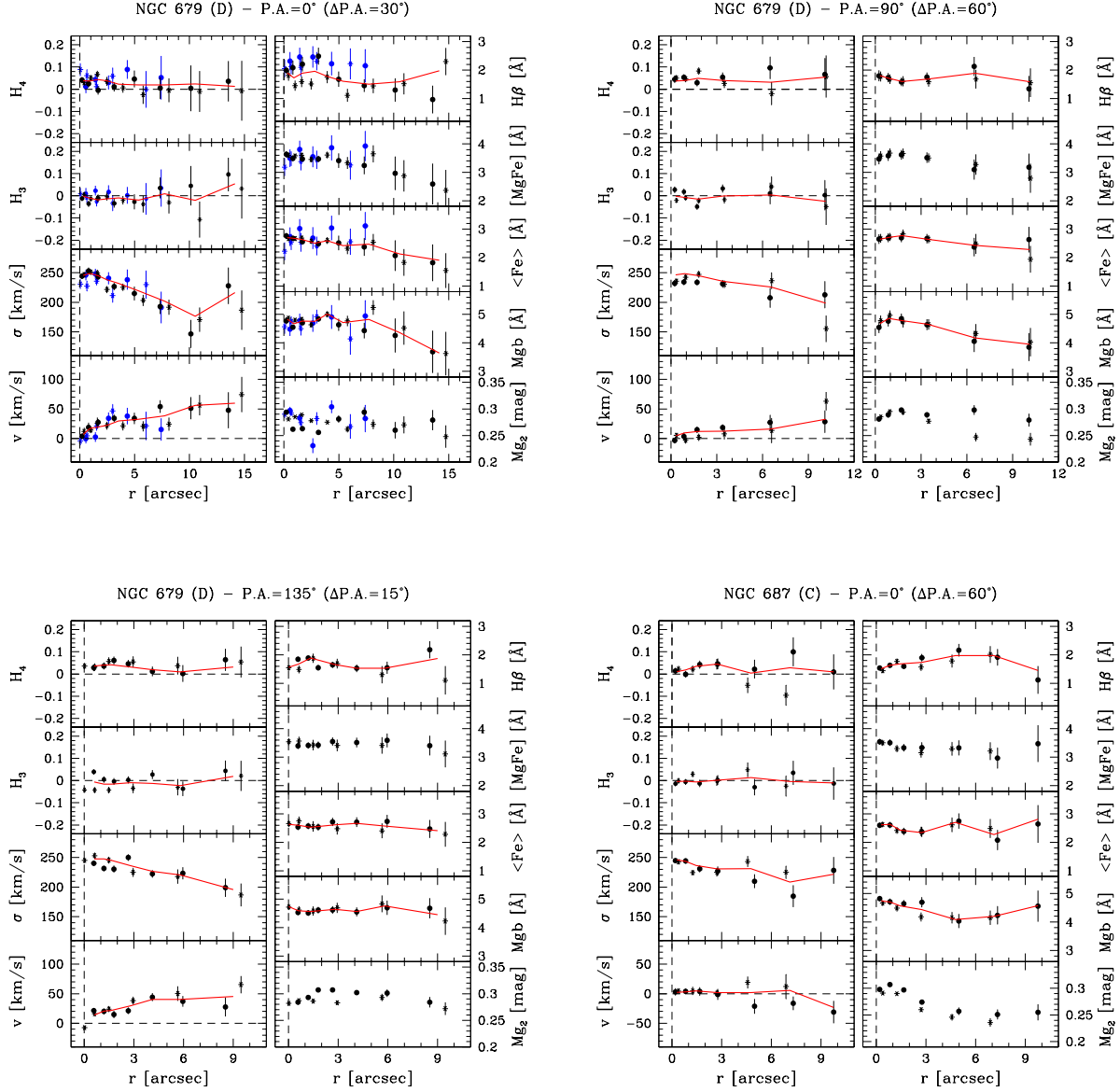


Fig. 4.— *Continued.*

centers. The folded kinematic profiles are plotted in Fig. 4. The multiple observations of IC 171, NGC 679, and UGC 1308 agree within the errors.

Fig. 5 shows the comparison between the measurements of σ obtained along the major axis of the sample galaxies and values available in literature. The mean difference in velocity dis-

persion with respect to the measurements by Wegner et al. (1999) is $\langle \Delta \log \sigma \rangle = 0.0008 \pm 0.0054$ and has a scatter $\sigma_{\Delta \log \sigma} = 0.023$. The central velocity dispersion of all the sample galaxies, except for NGC 712 and UGC 1308, were measured by Bernardi et al. (2002) and Wegner et al. (2003), too. The mean difference is $\langle \Delta \log \sigma \rangle =$

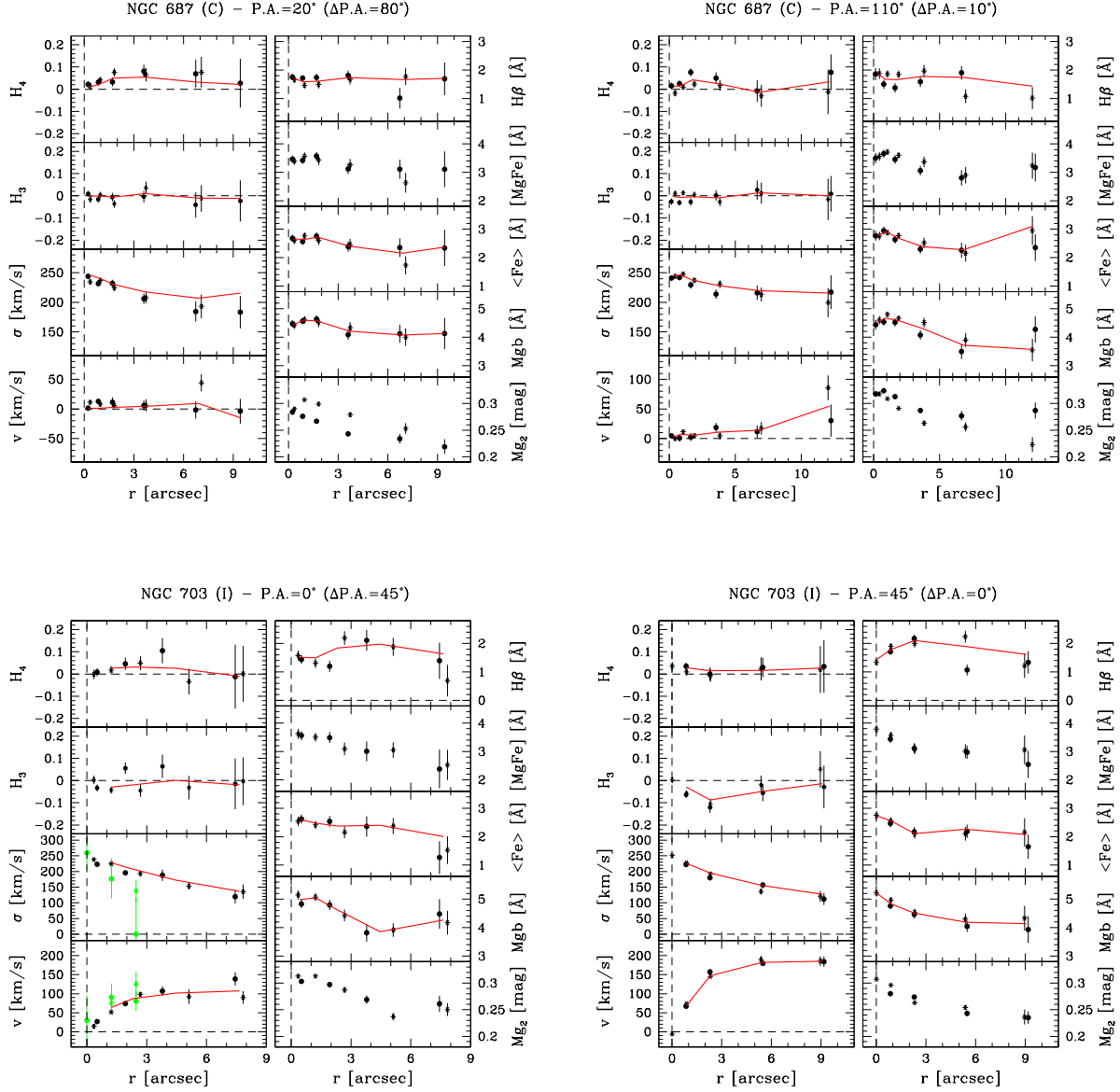


Fig. 4.— *Continued.*

-0.012 ± 0.013 with $\sigma_{\Delta \log \sigma} = 0.032$. Our values thus agree with published data sets within their measured errors.

Fig. 6 shows the central values of σ obtained along the minor and diagonal axes of the sample galaxies as a variance-weighted mean of the values available within an aperture of $3''$. They are

plotted as a function of the corresponding values obtained along the major axis. Most of the data are consistent within 3σ errors. No systematic effects are observed for the remaining ones.

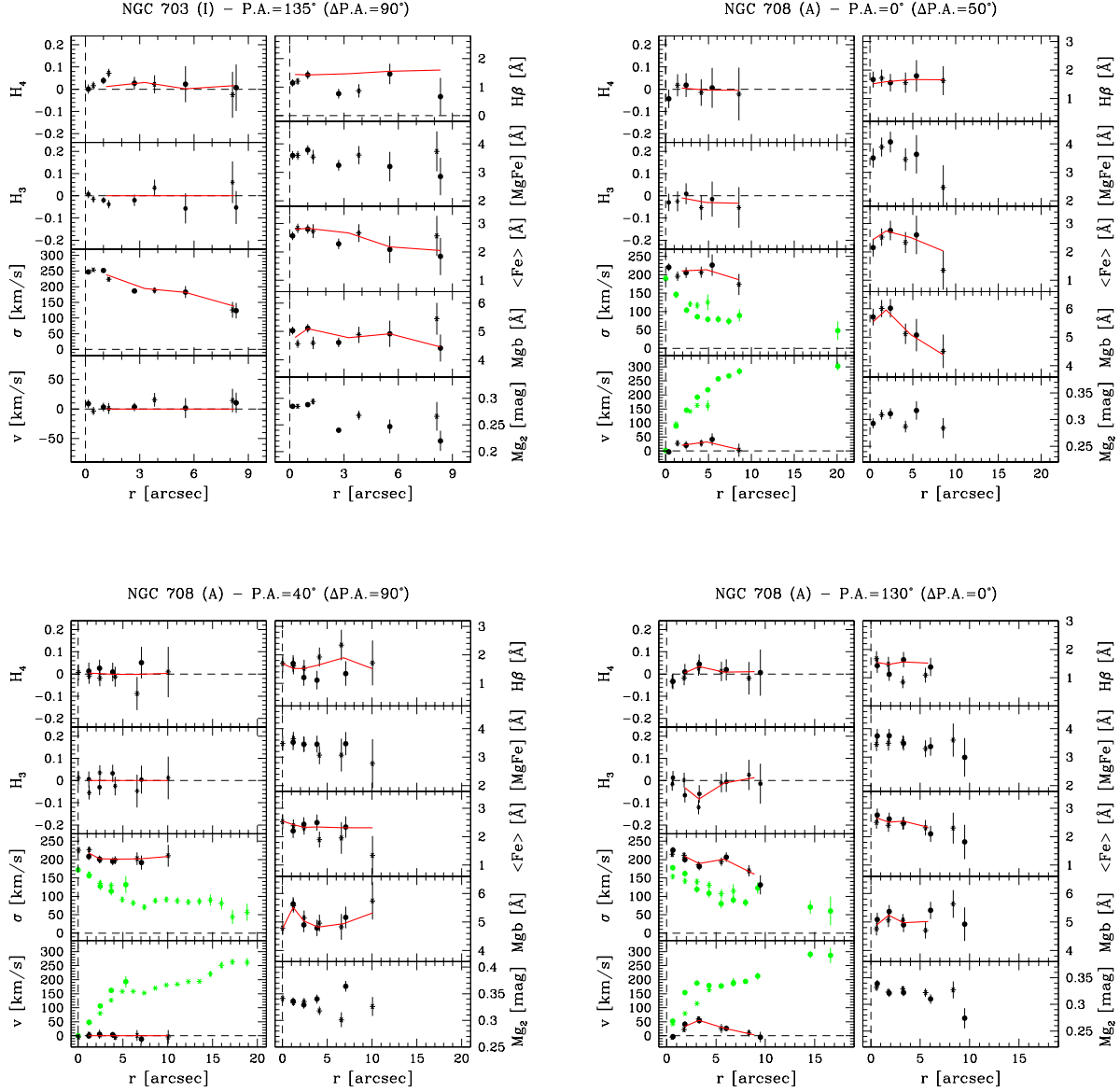


Fig. 4.— *Continued.*

4.3. Ionized-gas kinematics

The ionized-gas kinematics was measured from the emission lines present in the spectra of run 3, namely [N II] $\lambda\lambda 6548, 6583 \text{ \AA}$, H α , [S II] $\lambda\lambda 6716, 6731 \text{ \AA}$. Each observed emission line was fitted by a Gaussian, while describing the stellar continuum with a low-order polynomial. The Gaussians were

assumed to share the same line-of-sight velocity (v_{gas}) and velocity dispersion (σ_{gas}). A flux ratio of 1:2.96 was assumed for the [N II] doublet, as dictated by atomic physics (e.g., Osterbrock 1989).

The best-fitting Gaussian parameters were derived using a nonlinear least-squares minimization based on the robust Levenberg-Marquardt

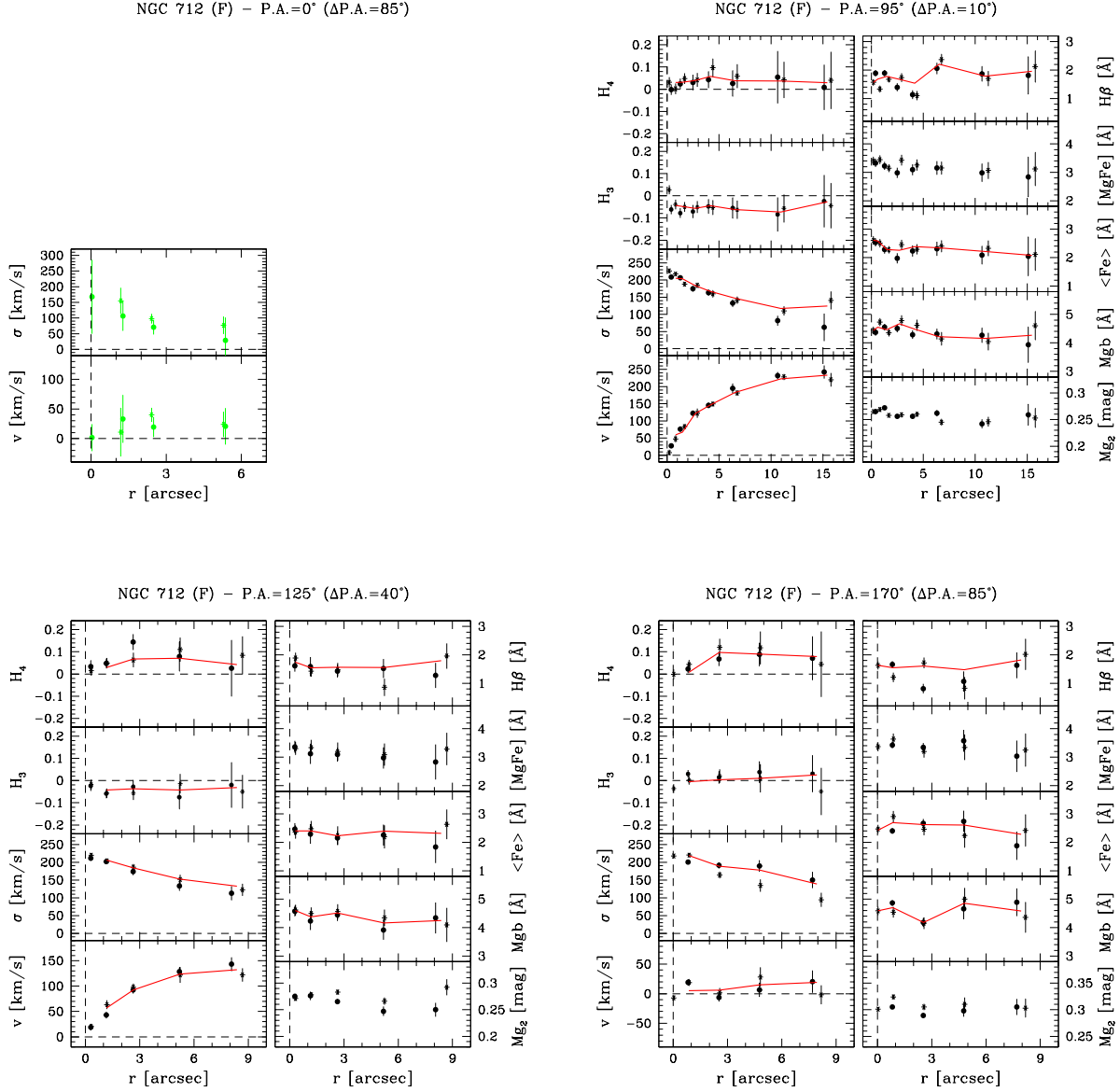


Fig. 4.— *Continued.*

method by Moré et al. (1980). The actual computation has been done using the MPFIT algorithm (Markwardt 2009) under the IDL environment. We averaged adjacent spectral rows to increase the S/N of the relevant emission lines. All the spectra of run 3 have $S/N < 30$ per resolution element in the continuum and were assigned to

quality class 4 (Table 2). We checked that the error in the kinematic parameter determination derived by Monte Carlo simulations did not differ significantly from the formal errors given as output by the least-squares fitting routine. We therefore decided to assume the latter as error bars on the gas kinematics.

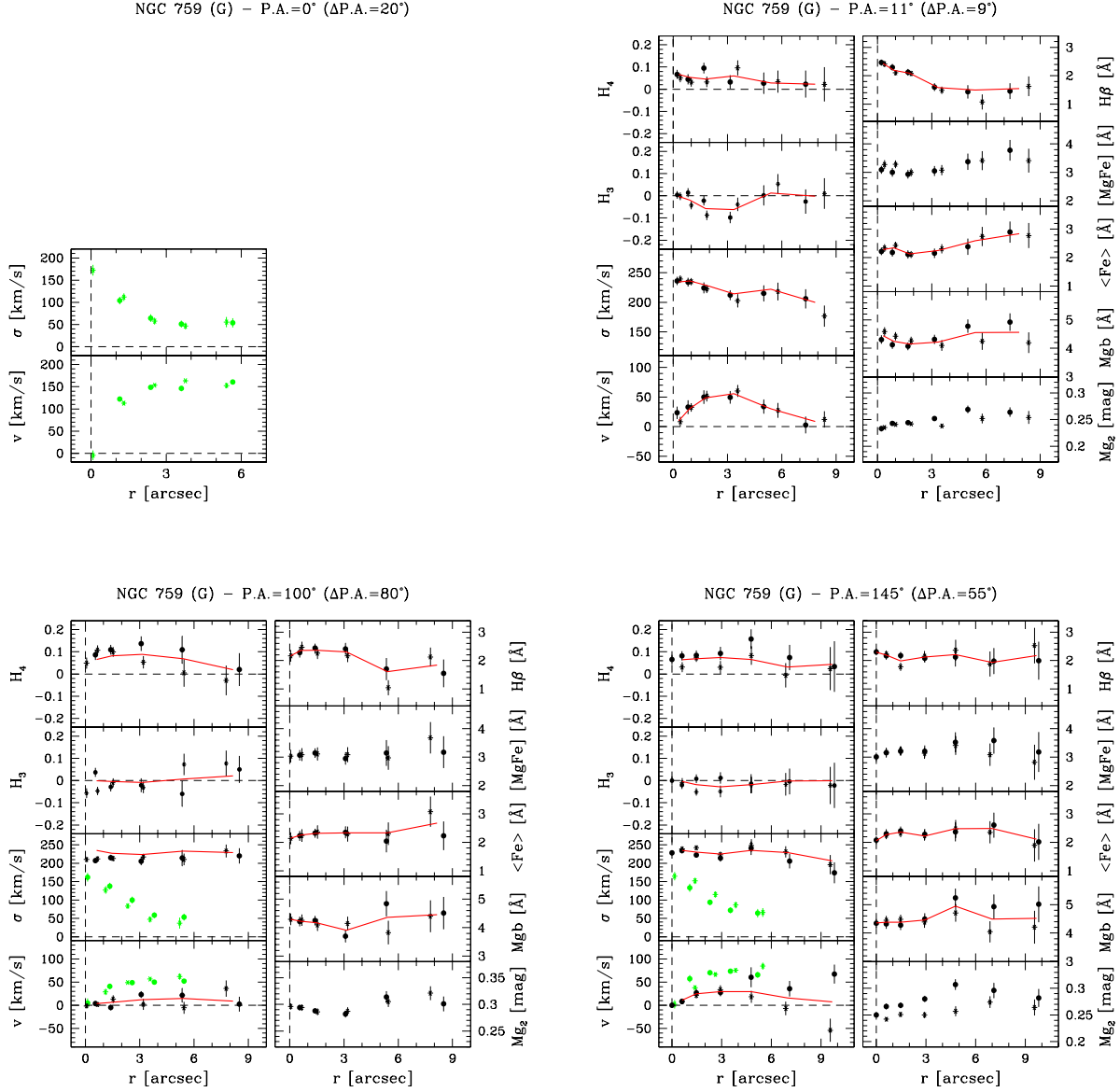


Fig. 4.— *Continued.*

The measured ionized-gas kinematics is reported in Table 7 where velocities are given relative to galaxy centers and velocity dispersions are corrected for instrumental FWHM. The folded kinematic profiles are plotted in Fig. 4.

4.4. Line-strength indices

The Mg, Fe, and H β line-strength indices were measured following Faber et al. (1985) and Worthey et al. (1994) from flux calibrated spectra obtained in runs 1 and 2. The average Iron index $\langle \text{Fe} \rangle = (\text{Fe}_{5270} + \text{Fe}_{5335})/2$ (Gorgas et al. 1990) and the combined Magnesium-Iron index

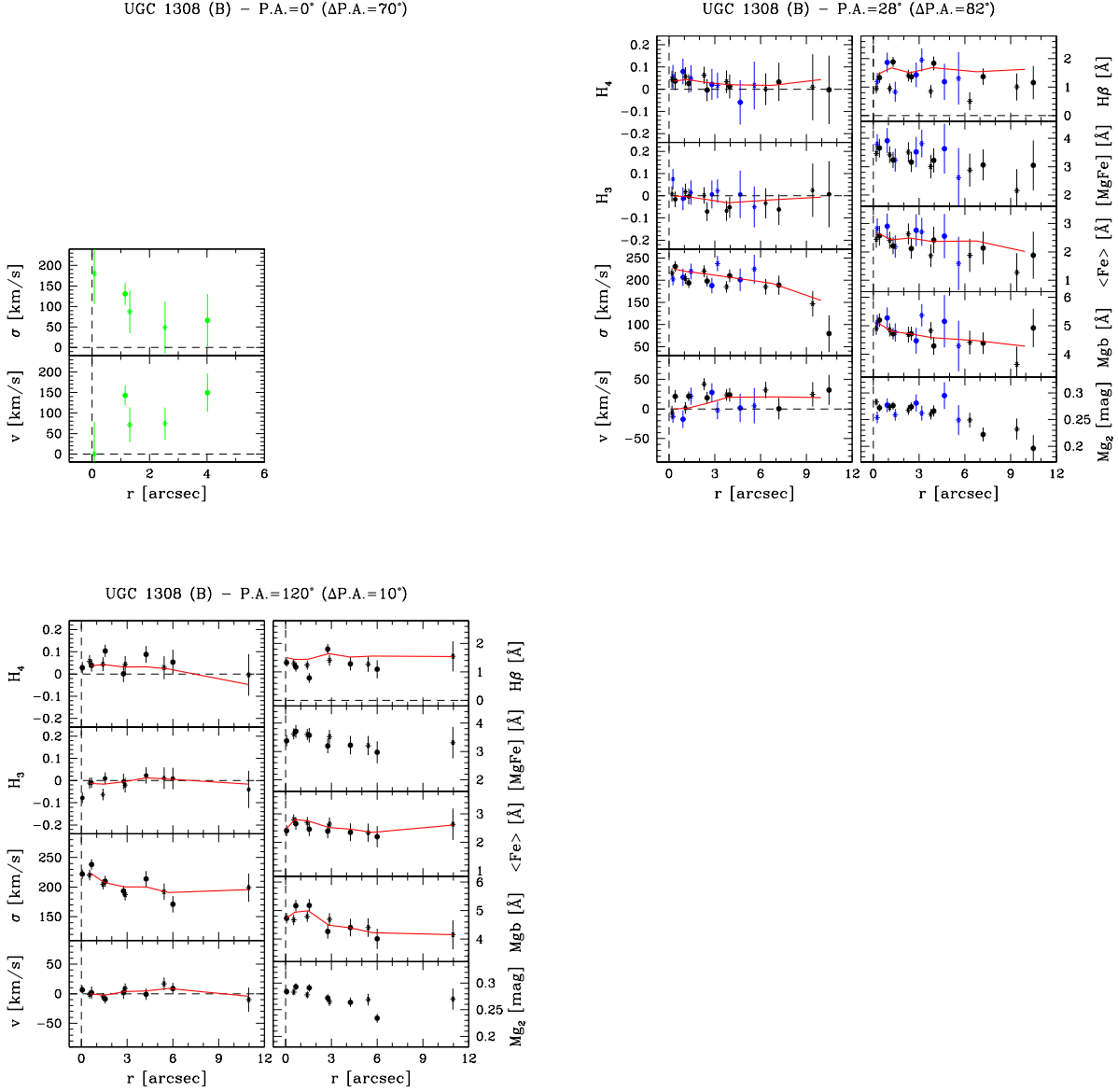


Fig. 4.— *Continued.*

with $[\text{MgFe}] = \sqrt{\text{Mgb}\langle\text{Fe}\rangle}$ (González 1993) were computed too. Spectra were rebinned in the dispersion direction as well as in the radial direction as before. The difference between our spectral resolution and the Lick/IDS system one ($\text{FWHM} = 8.6 \text{ Å}$; Worthey & Ottaviani 1997) was taken into account by degrading our spectra to

match the Lick/IDS resolution before measuring the line-strength indices. The original Lick/IDS spectra are not flux calibrated contrary to ours. Such a difference in the continuum shape is expected to introduce small systematic offsets of the measured values of the indices. To establish these offsets and to calibrate our measurements to the

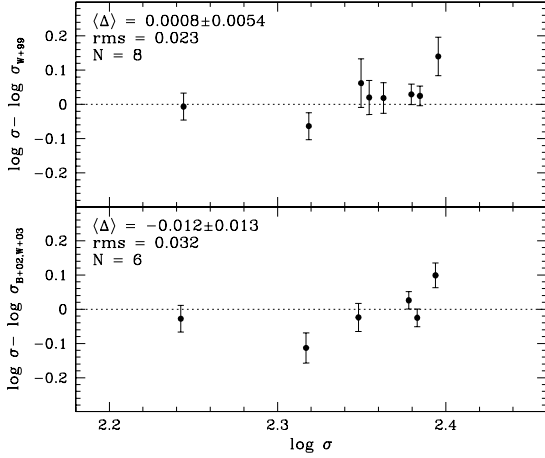


Fig. 5.— Central values of the stellar velocity dispersion σ measured along the major axis of the sample galaxies are compared to those available in Wegner et al. (1999, W+99), Bernardi et al. (2002, B+02), and Wegner et al. (2003, W+03).

Lick/IDS system, the values of the line-strength indices measured for the templates were compared to those obtained by Worthey et al. (1994). Fig. 7 shows the differences between our and Lick/IDS line-strength indices for the stars observed in runs 1 and 2. The offsets were evaluated as the mean of the differences between our and Lick/IDS line-strength values, and neglected if they were smaller than the mean error of the differences. The latter was the case of $H\beta$, Mg_2 , and Mgb for which no offset was adopted. On the contrary, it was applied an offset to the measured values of Fe_{5270} ($\Delta Fe_{5270} = -0.29 \text{ \AA}$ for run 1, -0.28 \AA for run 2) and Fe_{5335} ($\Delta Fe_{5335} = -0.48 \text{ \AA}$ for run 1, -0.44 \AA for run 2) to bring our data to the Lick/IDS system. No focus correction was applied because atmospheric seeing was the dominant effect during observations (see Mehlert et al. 1998 for details). Errors on indices were derived from photon statistics and CCD read-out noise, and calibrated by means of Monte Carlo simulations.

The measured values of $H\beta$, $[Mg/Fe]$, $\langle Fe \rangle$, Mgb , and Mg_2 are listed in Table 8 and plotted in Fig. 4. Fig. 6 shows the central values of $H\beta$, $[Mg/Fe]$, $\langle Fe \rangle$, Mgb , and Mg_2 obtained along the minor and diagonal axes of the sample galaxies as a variance-weighted mean of the values available within an aperture of $3''$ and those obtained along the cor-

responding major axes. Most of the data are consistent within 3σ errors. No systematic effects are observed for the remaining ones.

4.5. Properties of the stellar populations

The traditional and effective method of studying stellar population properties uses diagrams of different pairs of line-strength indices. Here, the modeling of the line-strength indices measured in the previous section followed the method described in Saglia et al. (2010) and Pu et al. (2010). Among the measured line-strength indices, $H\beta$, $\langle Fe \rangle$, and Mgb were considered since $H\beta$ is sensitive to early-type stars and thus useful as an age indicator, $\langle Fe \rangle$ gives the metal abundance, and Mgb covers the α -element abundance. The SSP models of Maraston (1998, 2005) and the models of Lick/IDS line-strength indices with α -element overabundance of Thomas et al. (2003) were spline-interpolated on a fine grid in age t (up to 15 Gyr on steps of 0.1 Gyr), metallicity $[Z/H]$ (from -2.25 to 0.67 dex on steps of 0.02 dex) and overabundances $[\alpha/Fe]$ (from -0.3 to 0.5 dex on steps of 0.05 dex). At each radius r of the galaxies the best-fit values of τ , $[Z/H]$, and $[\alpha/Fe]$ were determined by minimizing the χ^2 function

$$\chi^2(r) = \Delta^2 H\beta(r) + \Delta^2 Mgb(r) + \Delta^2 \langle Fe \rangle(r), \quad (1)$$

where

$$\Delta^2 I(r) = \left(\frac{I(r) - I_{SSP}(\tau, [Z/H], [\alpha/Fe])}{\sigma_I(r)} \right)^2. \quad (2)$$

Here $\sigma_I(r)$ is the error on the index $I(r)$ measured at a distance r and $I_{SSP}(\tau, [Z/H], [\alpha/Fe])$ is the value predicted by the SSP models for the given set of age, metallicity, and overabundance. As in Saglia et al. (2010) and Pu et al. (2010), the best-fit values of τ , $[Z/H]$, and $[\alpha/Fe]$ are derived to the same accuracy through the χ^2 minimization by giving the same weight to $H\beta$, $\langle Fe \rangle$, and Mgb . We did not extrapolate to values outside the model grid. Therefore, the minimum χ^2 solutions are sometimes found at the edges of the parameter space. Once the set of best-fit values, i.e. the set $(\tau_{min}, [Z/H]_{min}, [\alpha/Fe]_{min})$ that minimizes $\chi^2(r)$ was determined, we computed the values of the mass-to-light ratios of the corresponding SSP

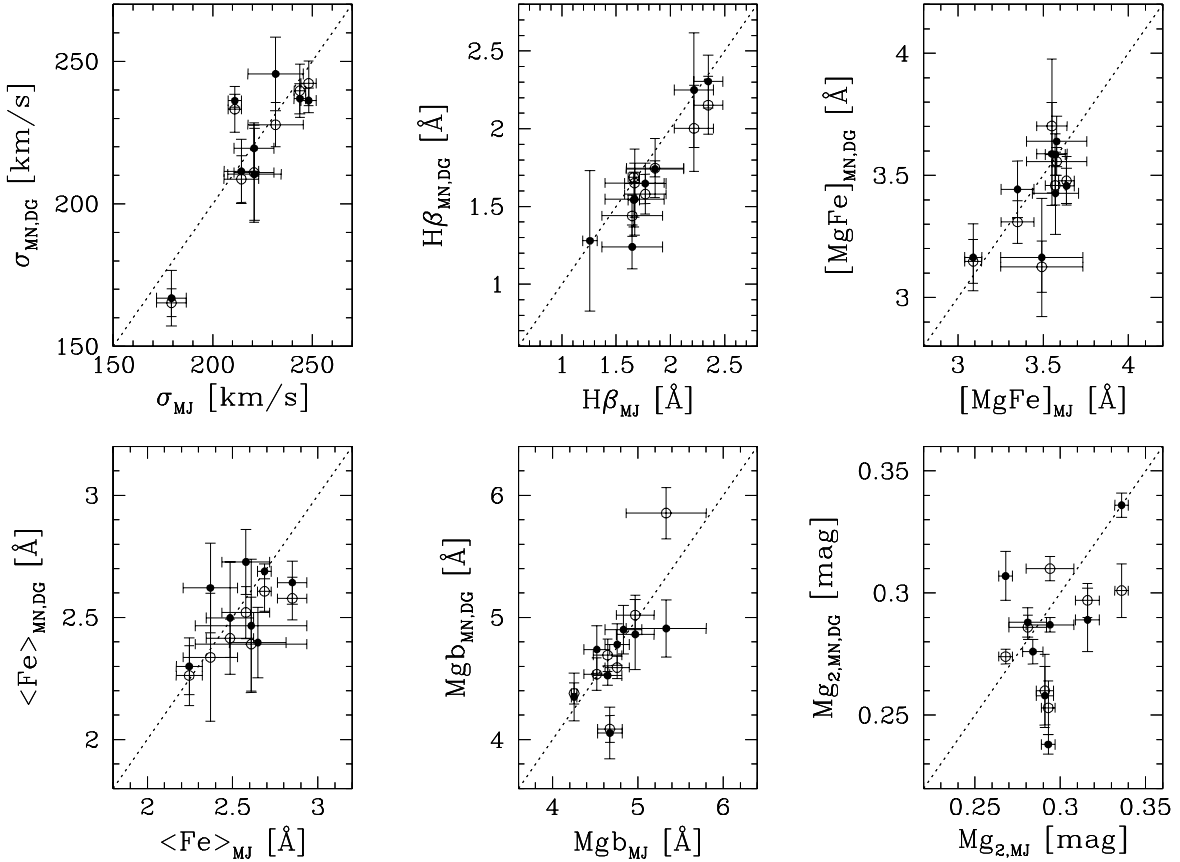


Fig. 6.— Central values of the stellar velocity dispersion σ and line-strength indices $H\beta$, $[\text{MgFe}]$, $\langle \text{Fe} \rangle$, Mgb , and Mg_2 measured within an aperture of $3''$ along the minor (filled circles) and diagonal axis (open circles) are compared to those measured along the major axis.

models for the Kroupa IMF (Υ_{Krou}). The resulting values of Υ_{Krou} , stellar-population ages, metallicities and overabundances (inside r_{eff}) are given in Table 3. Errors on all quantities were derived by considering the minimal and maximal parameter variations compatible with $\Delta\chi^2 = \chi^2 - \chi^2_{\min} = 1$. Note, however, that errors on age and metallicity are correlated to some extent (Worthey 1994).

5. Dynamical modeling

As discussed in Sec. 1, the dynamical modeling follows our previous work as in Thomas et al. (2007b,a, 2009a) and is based on the orbit superposition technique (Schwarzschild 1979) as implemented in Thomas et al. (2004, 2005b). We first

determined the stellar luminosity density from the surface brightness profile by deprojection into a three-dimensional, axisymmetric distribution with specified inclination, using the simulated annealing scheme implemented by Magorrian (1999). This algorithm reconstructs the luminosity density non-parametrically on a set of ≈ 250 sampling points in a plane perpendicular to the equatorial one and crossing the galactic center.

The adopted inclinations of the galaxies are given in Table 4. The nearly round dust features in NGC 679, NGC 759 and UGC 1308 suggest that these galaxies are almost face-on and we deprojected them at the lowest inclination compatible with a system that is intrinsically not flatter

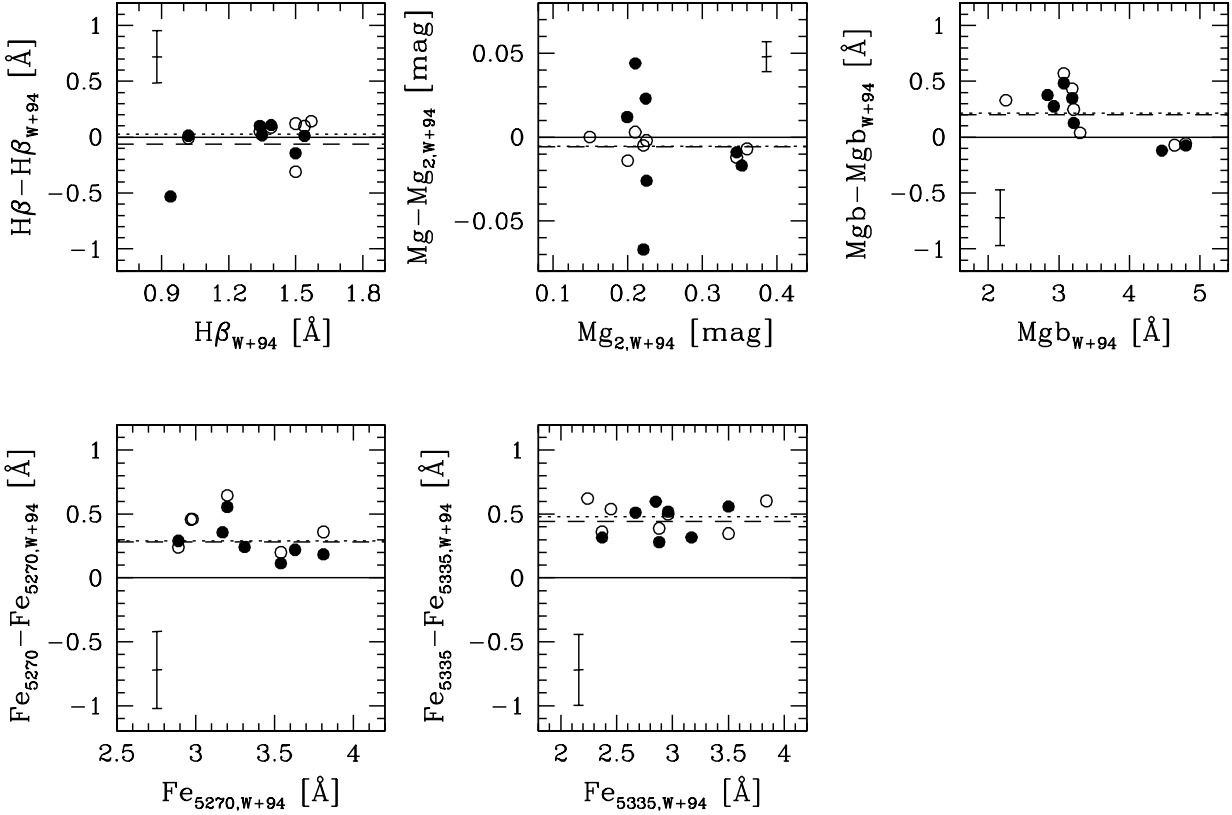


Fig. 7.— Comparison of the line-strength indices $H\beta$, Mg_2 , Mgb , Fe_{5270} , and Fe_{5335} measured for the stars in common with Worley et al. (1994, W+94). In each panel the error bar in the upper left corner indicates the mean error of the difference between our values and those by Worley et al. (1994), the continuous line shows the line of correspondence, the dotted and dashed lines correspond to the average difference of data in run 1 (open circles) and in run 2 (filled circles), respectively.

than an E7 galaxy. In all other galaxies, except NGC 687, the projected ellipticity reaches $\epsilon \approx 0.4$ at some radius and we assumed that these galaxies are edge-on ($i = 90^\circ$). The inclination of NGC 687 is unclear, but the galaxy is slightly flattened without showing any significant rotation at almost all radii and we assumed that this galaxy is edge-on, too. For the galaxies where no HST images were available, we deprojected the ground-based surface brightness taking into account seeing convolution as in Rusli et al. (2010). The solid lines in the Fig. 2 show the photometric profiles obtained by projecting the deprojected stellar luminosity density.

As a second step, we modeled the total mass

distribution of the galaxies as the sum of two components

$$\rho = \rho_* + \rho_{\text{halo}} \quad (3)$$

where ρ_* is the density of matter (either luminous or dark) that is distributed like the stars and ρ_{halo} is the density of dark matter distributed in a halo. The mass-to-light ratio of the matter distributed like the stars is

$$\Upsilon_* = \rho_*/\nu \quad (4)$$

where ν is the deprojected stellar luminosity density. Note that ρ_* measures all the matter following the light (it may include dark matter as well as stars). In contrast, ρ_{halo} is the halo density (some of the dark matter may not follow this profile) and

its distribution is assumed to be either a cored logarithmic profile (Binney & Tremaine 1987)

$$\rho_{\text{LOG}}(r) = \frac{V_c^2}{4\pi G} \frac{3r_c^2 + r^2}{(r_c^2 + r^2)^2} \quad (5)$$

or a NFW profile (Navarro et al. 1996)

$$\rho_{\text{NFW}}(r) \propto \frac{1}{r(r + r_s)^2}, \quad (6)$$

implemented as in Thomas et al. (2007b). In either case the halo is assumed spherical. Cored logarithmic halos have an asymptotically constant circular velocity V_c and a flat density core inside $r < r_c$.

Then, the gravitational potential Φ was computed by integrating Poisson's equation. Thousands of orbits were calculated in this fixed potential. The orbits were superposed to fit the observed LOSVDs, following the luminosity density constraint. The maximum entropy technique of Richstone & Tremaine (1988) was used to fit the kinematic data. The maximum entropy technique is a method for modeling galaxies from limited observations. While many distribution functions are consistent with the collisionless Boltzmann equation and the observational data, statistical mechanics and information theory suggest that the most natural ones have the largest entropy. The function

$$\hat{S} = S - \alpha\chi^2, \quad (7)$$

is maximized, where S is an approximation to the Boltzmann entropy and χ^2 is the sum of the squared residuals to the kinematic data. The smoothing parameter α controls the influence of the entropy S on the orbital weights. Thomas et al. (2005b) used Monte-Carlo simulations to derive the optimal α for a typical long-slit setup.

The best-fit dark halo densities, dark-halo mass fractions, and mass-to-light ratios Υ_* of the mass that is tied to the light are given in Table 4. The corresponding best fitting lines to the kinematic data are shown in Fig. 4.

6. Comparison with strong gravitational lenses and kinematics of the ionized gas

The statistical significance and accuracy of the methods employed here have been previously

tested. Thomas et al. (2005b) checked the axisymmetric orbit superposition code with mock observations of Coma galaxies and used Monte Carlo simulations to show that internal velocity moments could be reconstructed to $\approx 15\%$. In Thomas et al. (2007b), the mass-to-light ratio, halo-mass fraction, and shape of the circular velocity curve from the dynamical modeling of 17 Coma early-type galaxies are shown to be robust against the choice of the regularization parameter α .

A more severe modeling uncertainty is the unknown flattening of the galaxies along the line-of-sight. Even if all galaxies were perfectly axisymmetric their flattening along the line-of-sight is not directly observable and can only be inferred from the apparent flattening if the inclination is given. For early-type galaxies this is in general not the case and, moreover, even with the help of stellar kinematics the inclination remains only weakly constrained (e.g., Krajnović et al. 2005; van den Bosch & van de Ven 2009). However, dynamical mass-to-light ratios turn out to be robust against the inclination mismatch (e.g., Krajnović et al. 2005; Thomas et al. 2005b; van den Bosch & van de Ven 2009). Only if the flattening along the line-of-sight is significantly underestimated (as in the case of an almost face-on disk modeled as a spheroid), the dynamical masses can be biased by up to a factor of two (Thomas et al. 2007a). In addition, the mass recovery in the axisymmetric approximation becomes dependent on viewing angle and shape for significantly triaxial galaxies. End-on views of prolate/triaxial models give 20 – 30% overestimated masses, while for highly flattened face-on systems masses are underestimated by up to 50% (Thomas et al. 2007a).

Both, published masses of gravitational strong lenses that are structurally similar to our galaxies as well as our limited emission-line data for the galaxies in Abell 262 provide valuable checks on our foregoing analysis.

6.1. Comparison with strong gravitational lensing

Fig. 8 compares the projected dynamical masses of the Abell 262 galaxies with strong gravitational lenses from the SLACS survey (Auger et al. 2009). The comparison is done ex-

Table 3: Stellar-population parameters averaged inside r_{eff}

Object	Υ_{Krou} ($M_{\odot} L_{\odot}^{-1}$)	τ (Gyr)	[Z/H]	[α/Fe]	z_*
(1)	(2)	(3)	(4)	(5)	(6)
IC 171 (E)	3.22 ± 0.70	9.0 ± 2.4	0.12 ± 0.10	0.08 ± 0.05	$1.3^{+1.3}_{-0.6}$
NGC 679 (D)	3.65 ± 0.29	9.7 ± 1.0	0.21 ± 0.05	0.31 ± 0.02	$1.5^{+0.5}_{-0.3}$
NGC 687 (C)	3.72 ± 0.44	9.9 ± 1.6	0.17 ± 0.07	0.22 ± 0.03	$1.6^{+1.1}_{-0.5}$
NGC 703 (I)	2.15 ± 0.32	5.2 ± 1.2	0.23 ± 0.05	0.45 ± 0.02	$0.5^{+0.2}_{-0.1}$
NGC 708 (A)	4.17 ± 1.05	11.0 ± 3.1	0.19 ± 0.14	0.39 ± 0.05	$2.2^{+\infty}_{-1.2}$
NGC 712 (F)	2.42 ± 0.37	6.2 ± 1.4	0.20 ± 0.08	0.39 ± 0.03	$0.7^{+0.2}_{-0.2}$
NGC 759 (G)	2.75 ± 0.31	7.1 ± 0.9	0.16 ± 0.07	0.35 ± 0.04	$0.8^{+0.2}_{-0.1}$
UGC 1308 (B)	3.07 ± 1.06	8.8 ± 4.4	0.07 ± 0.16	0.30 ± 0.10	$1.2^{+5.0}_{-0.8}$

NOTE.—Col. 1: Name. Col. 2: SSP mass-to-light ratio Υ_{Krou} in the Kron-Cousins R band. Col. 3: SSP age τ . Col. 4: SSP metallicity [Z/H]. Col. 5: SSP α -elements overabundance [α/Fe]. Col. 6: Star-formation redshift z_* .

Table 4: Mass-to-light ratio, parameters of the dark matter halo, stellar velocity dispersion, and geometric parameters adopted for the dynamical model.

Object	Model	Υ_* ($M_{\odot} L_{\odot}^{-1}$)	f_{halo}	$\log_{10}\langle\rho_{\text{halo}}\rangle$ ($M_{\odot} \text{ pc}^{-3}$)	z_{DM}	σ_{eff} (km s $^{-1}$)	i_{stars} ($^{\circ}$)	P.A. $_{\text{stars}}$ ($^{\circ}$)
(1)	(2)	(3)	(4)	(5)	(6)	(7)	(8)	(9)
IC 171 (E)	NFW	$3.5^{+0.5}_{-0.5}$	$0.41^{+0.18}_{-0.12}$	$-2.17^{+0.33}_{-0.14}$	0.7	211.4 ± 1.5	90	115
NGC 679 (D)	NFW	$4.0^{+0.5}_{-0.5}$	$0.27^{+0.13}_{-0.11}$	$-1.00^{+0.25}_{-0.04}$	1.3	252.7 ± 0.9	30	150
NGC 687 (C)	LOG	$3.5^{+0.5}_{-1.0}$	$0.36^{+0.21}_{-0.07}$	$-1.03^{+0.08}_{-0.21}$...	237.4 ± 1.3	90	120
NGC 703 (I)	LOG	$9.5^{+0.5}_{-0.5}$	$0.001^{+0.062}_{-0.001}$	$-3.12^{+1.56}_{-\infty}$	3.7	233.3 ± 1.2	90	45
NGC 708 (A)	SC	$7.5^{+1.0}_{-2.5}$	< 0.41	< -2.11	0.8	189.2 ± 1.6	90	130
NGC 712 (F)	SC	$8.5^{+0.5}_{-0.5}$	< 0.06	< -1.84	4.0	225.2 ± 0.9	90	85
NGC 759 (G)	LOG	$4.5^{+0.5}_{-0.5}$	$0.48^{+0.04}_{-0.18}$	$-1.22^{+0.17}_{-0.25}$	2.8	231.0 ± 1.1	40	20
UGC 1308 (B)	SC	$2.6^{+0.1}_{-0.1}$	< 0.20	< -1.95	...	202.6 ± 1.8	50	110

NOTE.—Col. 1: Name. Col. 2: Type of best-fit mass model (LOG: logarithmic halo, NFW: NFW halo, SC: self-consistent, i.e. no dark matter halo). Col. 3: Dynamical mass-to-light ratio Υ_* (including all the mass that follows the light) in the Kron-Cousins R band. Col. 4: Spherically averaged halo-mass fraction within r_{eff} . Col. 5: Average halo density within $2 r_{\text{eff}}$. Col. 6: Dark halo assembly redshift z_{DM} . Col. 7: Velocity dispersion σ_{eff} inside r_{eff} . Col. 8: Assumed galaxy inclination i_{stars} . Col. 9: Position angle P.A. $_{\text{stars}}$ of the line of nodes measured North through East adopted for the dynamical model.

actly as in Thomas et al. (2011) and we refer the reader to this paper for further details. We find no significant differences between the Abell 262 galaxies, Coma galaxies, and SLACS lenses, respectively. Note that the scatter in the dynamical masses is not larger than in the lensing masses. This implies that possible biases in the dynamical modeling related to spatially limited kinematic observations and/or symmetry assumptions are unlikely (as they would increase the scatter in dynamical masses of galaxies observed at random

viewing angles). That the Coma and Abell 262 galaxies must have nearly axisymmetric shapes is consistent with the lack of isophotal twists or minor-axis rotation in the photometric and kinematic observations, respectively (except for IC 171 and NGC 708; cf. Sec. 6.2).

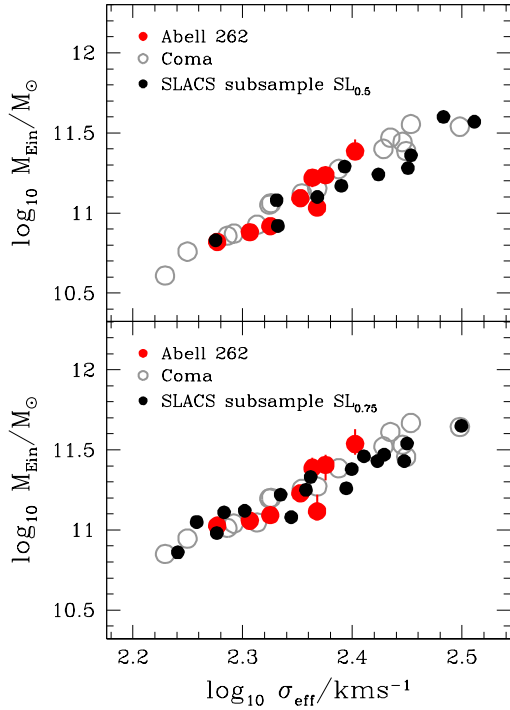


Fig. 8.— Projected total mass, M_{Ein} , within a fiducial Einstein radius, r_{Ein} , as a function of the effective velocity dispersion, σ_{eff} , for the galaxies in Abell 262 (red filled circles; the error bars are smaller than the symbols in most cases), Coma Cluster (open circles, Thomas et al. 2011), and SLACS survey (Auger et al. 2009; black filled circles). The dynamical masses from two-component models with dark halos ($\rho = \Upsilon_* \times \nu + \rho_{\text{halo}}$) are shown. The lensing galaxies are divided into the SL0.5 (with $\langle r_{\text{Ein}}/\sigma_{\text{eff}} \rangle \approx 0.5$, top panel) and SL0.75 (with $\langle r_{\text{Ein}}/\sigma_{\text{eff}} \rangle \approx 0.75$, bottom panel) subsamples, respectively.

6.2. Comparison between circular velocity and ionized-gas rotation velocity

Fig. 10 compares the circular velocity v_{circ} obtained from stellar dynamics and rotation velocity v_{rot} of the ionized gas. The comparison is restricted to radii r_{gas} where the pressure support in the gas component is small ($\sigma_{\text{gas}} \leq 60 \text{ km s}^{-1}$) and therefore the gas velocity is supposed to trace v_{circ} (Bertola et al. 1995; Pignatelli et al. 2001; Dalcanton & Stilp 2010). The line-of-sight gas velocity v_{gas} is derived from the observed one af-

ter subtracting the systemic velocity and folding around the galaxy center. It was deprojected into v_{rot} by assuming that the gaseous component rotates in circular orbits in an infinitesimally thin disk. The orientation of the gaseous disk with respect to the line of sight is given by its inclination (i_{gas}) and the position angle of its line of nodes (P.A._{gas}). Therefore, it is

$$v_{\text{rot}} = \frac{v_{\text{gas}}}{\sin i_{\text{gas}} \cos \vartheta}, \quad (8)$$

where

$$\vartheta = \arctan \frac{\tan \Delta \text{P.A.}_{\text{gas}}}{\cos i_{\text{gas}}} \quad (9)$$

and

$$\Delta \text{P.A.}_{\text{gas}} = \text{P.A.}_{\text{gas}} - \text{P.A.}_{\text{slit}}. \quad (10)$$

P.A._{slit} is the position angle of the slit where v_{gas} is measured. Likewise, the deprojected radius is

$$r = r_{\text{gas}} \cos \vartheta \cos \Delta \text{P.A.}_{\text{gas}}. \quad (11)$$

In an axisymmetric spheroidal system, the position angle P.A._{stars} of the stellar isophotes is constant with radius and a rotating gaseous disk is confined to the equatorial plane. Hence, the unique stellar P.A._{stars} coincides with the P.A._{gas} of the gaseous disk. The same holds for the inclinations. For the ionized-gas component of the Abell 262 galaxies we only have observations along a few slits and can neither verify the assumption of an infinitesimally thin disk nor, given the case, derive its orientation (i.e., P.A._{gas} and i_{gas}) directly. Therefore, we performed two different deprojections of the gas kinematics for each galaxy.

Firstly, we assumed that the galaxy is an axisymmetric spheroid and deprojected the gas kinematics with $i_{\text{gas}} = i_{\text{stars}}$ and $\text{P.A.}_{\text{gas}} = \text{P.A.}_{\text{stars}}$ from the dynamical model (Tab. 4). The corresponding values v_{rot} are open dots in Fig. 10 (when missing, they fall outside the plot range). We used $i_{\text{gas}} = 85^\circ$ when the dynamical model has $i_{\text{stars}} = 90^\circ$ since an infinitesimally thin and exactly edge-on gas disk would not be observable at any P.A. different from the galaxy's major axis.

Secondly, since the isophotal P.A. of the Abell 262 galaxies show some scatter, we varied i_{gas} and P.A._{gas} and minimized the χ^2 difference between v_{rot} and v_{circ} . The P.A._{gas} was changed between the minimum and maximum values measured for the P.A. of the galaxy isophotes. The

best-fitting values of v_{rot} are shown by the filled circles in Fig. 10. For each galaxy, the figure also quotes i_{gas} and P.A._{gas} for both sets of deprojection. IC 171 was treated separately, as discussed below.

As Fig. 10 shows, using the same P.A. and i for both the gaseous disks and dynamical models did not yield good agreement between v_{rot} and v_{circ} . However, varying i_{gas} and P.A._{gas} allowed matching the gas kinematics with predictions of the dynamical models quite well. The corresponding inclinations i_{gas} differ from the i_{stars} values of the dynamical models by less than 10°. The inclination of an elliptical galaxy can, at best, be derived dynamically with an uncertainty of ±20° (e.g., Krajnović et al. 2005; Thomas et al. 2005b; van den Bosch & van de Ven 2009). Thus, a $\Delta i \leq 10^\circ$ is well within the uncertainties of the dynamical models.

The case for the position angles is more complicated. To ease the comparison with the orientation of the stars in the galaxies, the P.A. panels in Fig. 2 show the position angles adopted in the two deprojection sets. The red solid line corresponds to P.A._{gas} = P.A._{stars} and gives the open circles for v_{rot} plotted in Fig. 10. The grey solid line marks the gas orientation that minimizes the χ^2 between gas rotation and dynamical v_{circ} and leads to the filled circles for v_{rot} given in Fig. 10. The dotted lines in Fig. 2 delimit the 68% confidence region of P.A._{gas}.

The ionized-gas kinematics for our Abell 262 galaxies has limited spatial coverage and radial extension because only a few slits were observed. Nevertheless, this gives a valuable consistency check. Within the above limitations and when $\sigma_{\text{gas}} \leq 60 \text{ km s}^{-1}$, the gas rotation velocity is consistent with the circular velocity obtained from our axisymmetric dynamical models and supports to the total mass distributions we derived. This holds also for IC 171 and NGC 708, which are not exactly axisymmetric systems.

6.3. Notes on individual galaxies

In the following we discuss the Abell 262 galaxies individually, except for NGC 679 and NGC 687 which show no detectable emission line.

IC 171. The observed isophotal twist (Fig. 2) suggests that IC 171 is not exactly axisymmetric, similarly to NGC 708. Moreover, v_{rot} do not match the dynamical v_{circ} for any P.A. within the observed range. If IC 171 is triaxial, the gas might also be rotating around the long axis of the galaxy. To test this geometric configuration, we tried a variety of different P.A._{gas} tilted by about 90° with respect to the photometric major axis, fixing the inclination at $i_{\text{gas}} = 85^\circ$. A P.A._{gas} = 13° brings v_{rot} in agreement with v_{circ} . If the gas rotates around the long axis of the galaxy, then the line of nodes of the gaseous disk is at P.A. = 103°. This value is consistent with the orientation of the galaxy isophotes at the corresponding deprojected radii ($r \gtrsim 3 \text{ kpc}$, Fig. 2).

NGC 703. The isophotes show little variation in position angle over all the observed radii ($30^\circ \lesssim \text{P.A.} \lesssim 50^\circ$, Fig. 2). We found P.A._{stars} ≈ P.A._{gas} and $i_{\text{stars}} \approx i_{\text{gas}}$ within the scatter of the data after minimizing the χ^2 -difference between dynamical circular velocity and gas rotation velocity (Fig. 10). The photometric and kinematic data are consistent with our assumptions about both the stellar and gaseous components.

NGC 708. The inner and outer isophotes ($r \lesssim 2.5 \text{ kpc}$) have different orientations (Fig. 2). The dynamical model was adjusted towards the galaxy center, where the stellar kinematics was measured (Fig. 4) and the largest stellar rotation is at P.A. = 130°. It vanishes at P.A. = 40°, indicating that the position angle of the galaxy's line of nodes is close to P.A._{stars} = 130° adopted for the dynamical model. The gas rotation differs as it is large along all the observed slits (Fig. 4) and the derived P.A._{gas} is close to the position angle measured for the outer isophotes and v_{rot} best matches v_{circ} for a nearly edge-on gas disk with P.A._{gas} = 34°. For $i_{\text{gas}} = 80^\circ$ the deprojected radii ($r \approx 7 \text{ kpc}$; Fig. 10) fall into the region where the stellar system has a photometric P.A. ≈ 40° (Fig. 2). The twist of the isophotes indicates that the system cannot be exactly axisymmetric. However, as P.A._{gas} is consistent with the stellar orientation at the corresponding radii we infer that NGC 708 is probably only mildly triaxial and that its dynamical mass is reliable.

NGC 712. The emission-line spectrum was taken close to the galaxy minor-axis, making deprojection of v_{gas} highly uncertain. The measured rotation velocities are low (Fig. 4) and, therefore, consistent with a gaseous disk with the same $i_{\text{gas}} = i_{\text{stars}}$ and $\text{P.A.}_{\text{gas}} = \text{P.A.}_{\text{stars}}$ as adopted in the dynamical model of the galaxy.

NGC 759. The position angle of the isophotes of NGC 759 ranges between about 10° and 50° beyond radii of 0.1 kpc (Fig. 2). The gas kinematics was measured along three different axes and has a regular and symmetric rotation curve and velocity dispersion profile (Fig. 4). We found $\text{P.A.}_{\text{stars}} \approx \text{P.A.}_{\text{gas}}$ and $i_{\text{stars}} \approx i_{\text{gas}}$ (Fig. 10) confirming the orientation and intrinsic shape obtained from the stellar dynamics.

UGC 1308. The orientation of the isophotes scatters significantly within 2 kpc, but it is constant at larger radii. For the dynamical model we adopted $\text{P.A.}_{\text{stars}} = 110^\circ$, which is representative of the orientation of the major axis of the isophotes at $r \gtrsim 2$ kpc (Fig. 2). A much smaller $\text{P.A.}_{\text{gas}} = 47^\circ$ is needed to match v_{rot} measured along a diagonal axis with v_{circ} from stellar dynamics. However, the uncertainties in P.A._{gas} are large and the predictions of the dynamical model are formally consistent with the gas rotation. Also the measured photometric P.A. has large uncertainties because the galaxy is pretty round ($\epsilon \lesssim 0.2$; Fig. 2).

7. Results

In this Section we discuss the results from the dynamical and stellar-population models.

7.1. Evidence for halo mass not associated to the light

Fig. 9 shows the χ^2 of Eq. 7 against the dynamical mass-to-light ratios Υ_* for the Abell 262 galaxies. Three parameter fits including a logarithmic dark halo component $\rho_{\text{halo}} = \rho_{\text{LOG}}$ (Eq. 5; the three parameters are Υ_* , r_c , and V_c) are displayed by solid lines and we marginalized over the halo parameters. Similarly, NFW halos are shown by the dashed lines and the dotted curves are for models in which all the mass follows the light ($\rho_{\text{halo}} \equiv 0$).

The kinematics of NGC 679, NGC 687, and NGC 759 cannot be fit without $\rho_{\text{halo}} > 0$. The statistical significance is at least 3σ and the dark halos dominate beyond $r \approx 1.7 r_{\text{eff}}$, $1.4 r_{\text{eff}}$, and $1.0 r_{\text{eff}}$, respectively (Fig. 10). These radii are only slightly larger than the radius r_{max} of the farthest kinematic data point. For IC 171 the evidence for $\rho_{\text{halo}} > 0$ is about 2σ and the dark halo outweighs the mass following the light beyond $r \approx 2.9 r_{\text{eff}}$, which is significantly on the far side of r_{max} . For the remaining objects (NGC 703, NGC 708, NGC 712, and UGC 1308) a second mass-component ρ_{halo} does not improve the fit significantly. In fact, the best-fitting models of NGC 708, NGC 712, and UGC 1308 are obtained without any dark matter in a halo with a different mass distribution than the stars, while the best-fit halo-mass fraction inside r_{eff} in NGC 703 is $f_{\text{halo}} = 0.001$, its upper limit $f_{\text{halo}} \leq 0.06$.

In the Coma galaxy sample of Thomas et al. (2007b) the statistical significance for dark halos is over 95% for 8 (out of 17) galaxies and the halo-mass takes over the mass that follows the light roughly between r_{eff} and $2 r_{\text{eff}}$. IC 171, NGC 679, NGC 687, and NGC 759 have comparable dark halos. In Coma, however, we found only one galaxy with $f_{\text{halo}} \approx 0$ (GMP 1990, Thomas et al. 2007b), whereas the Abell 262 sample reveals 4 (out of 8) galaxies of this kind.

The evidence for a dark component aside mass that follows light is not directly connected to the spatial extent of the kinematic data (indicated by the dashed horizontal lines in Fig. 10). For example, the presence of halo mass in NGC 759 is highly significant, even though $r_{\text{max}} < r_{\text{eff}}$. By contrast, our measurements reach $r_{\text{max}} \approx 1.5 r_{\text{eff}}$ in NGC 712 yet the mass distribution follows the light almost exactly. Likewise, in the Coma galaxy GMP 1990 mass follows light out to $r_{\text{max}} \approx 3 r_{\text{eff}}$. The kinematic evidence for extra mass beyond the light is also not coupled to the degree of rotation or flattening. For example, UGC 1308 is round and shows almost no rotation, whereas NGC 712 is a moderately flattened, strong rotator and the Coma galaxy GMP 1990 is a highly-flattened ($\epsilon_{\text{max}} \approx 0.6$) fast rotating system as well.

As already noted for the Coma galaxies, we can not discriminate between NFW halos and logarithmic halos based on the quality of the kinematic

fits. There is only one Abell 262 galaxy where NFW halos fit worse by $\Delta\chi^2 \approx 2$ (NGC 703), in all other galaxies the difference is $\Delta\chi^2 \leq 1$.

7.2. Mass that follows the light

The two upper panels of Fig. 11 plot Υ_* and the corresponding SSP Υ_{Krou} values as a function of σ_{eff} , i.e., the velocity dispersion averaged within r_{eff} . The galaxies of Abell 262 follow trends very similar to the galaxies in the Coma cluster. While the dynamically determined Υ_* increase strongly with σ_{eff} , the SSP models result in almost constant Υ_{Krou} . This implies that the ratio $\Upsilon_*/\Upsilon_{\text{Krou}}$ increases with σ_{eff} , as shown explicitly in the bottom panel of Fig. 11.

Around $\sigma_{\text{eff}} \approx 200 \text{ km s}^{-1}$ the distribution of $\Upsilon_*/\Upsilon_{\text{Krou}}$ has a sharp cutoff with almost no galaxy below $\Upsilon_*/\Upsilon_{\text{Krou}} = 1$ (Fig. 11, bottom panel). For $\sigma_{\text{eff}} \gtrsim 250 \text{ km s}^{-1}$ the lower bound of $\Upsilon_*/\Upsilon_{\text{Krou}}$ increases to $\Upsilon_*/\Upsilon_{\text{Krou}} \gtrsim 2$ at $\sigma_{\text{eff}} \approx 300 \text{ km s}^{-1}$. Similar trends are also observed in the SAURON sample (Cappellari et al. 2006; cf. the triangles in the bottom panel of Fig. 11), in SLACS galaxies (Treu et al. 2010; squares in Fig. 11) and, recently, in the ATLAS3d survey (Cappellari et al. 2012).

7.3. Dark halo densities

Fig. 12 displays the average dark halo densities $\langle \rho_{\text{halo}} \rangle$ inside $2r_{\text{eff}}$ of Coma and Abell 262 galaxies against the dynamical mass that follows the light $M_* = \Upsilon_* \times L$. In contrast to the Coma galaxies not all the Abell 262 galaxies have denser dark halos than spirals. For the three Abell 262 galaxies closest to the spiral galaxy scaling relations (NGC 703, NGC 708, and UGC 1308) we can only determine upper limits for the amount of mass that is distributed unlike the light. In these cases, models without a halo fit the data equally well within the uncertainties, or even better than models with halo.

Still, the majority of cluster early-types has 2–10 times denser halos than local spirals, implying a 1.3–2.2 times higher $(1+z_{\text{DM}})$ (assuming $\langle \rho_{\text{DM}} \rangle \sim (1+z_{\text{DM}})^3$). Thus, if spirals typically formed at $z \approx 1$, then cluster ellipticals assembled at $z_{\text{DM}} \approx 1.6 - 3.4$.

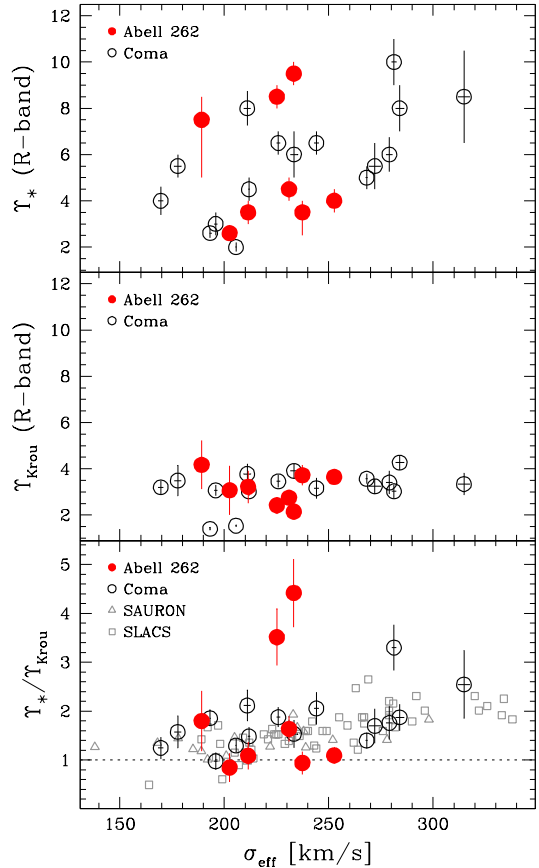


Fig. 11.— Dynamical Υ_* (upper panel), stellar-population Υ_{Krou} (middle panel), and the ratio $\Upsilon_*/\Upsilon_{\text{Krou}}$ (bottom panel) as a function of the effective velocity dispersion, σ_{eff} , for galaxies in Abell 262 (filled circles) and Coma Cluster (open circles, Thomas et al. 2011). In the bottom panel, the results for the Abell 262 and Coma galaxies are also compared to SLACS galaxies with combined dynamical and lensing analysis (open squares, Treu et al. 2010) and SAURON galaxies with dynamical models lacking a separate dark halo (open triangles, Cappellari et al. 2006).

7.4. Dark matter fractions

Averaging over all Abell 262 galaxies we find that a fraction of $\langle f_{\text{halo}} \rangle = 0.19$ of the total mass inside r_{eff} is in a dark halo distinct from the light. The mean over the Coma galaxies is $\langle f_{\text{halo}} \rangle = 0.23$ and similar fractions come from other dynamical studies employing spherical

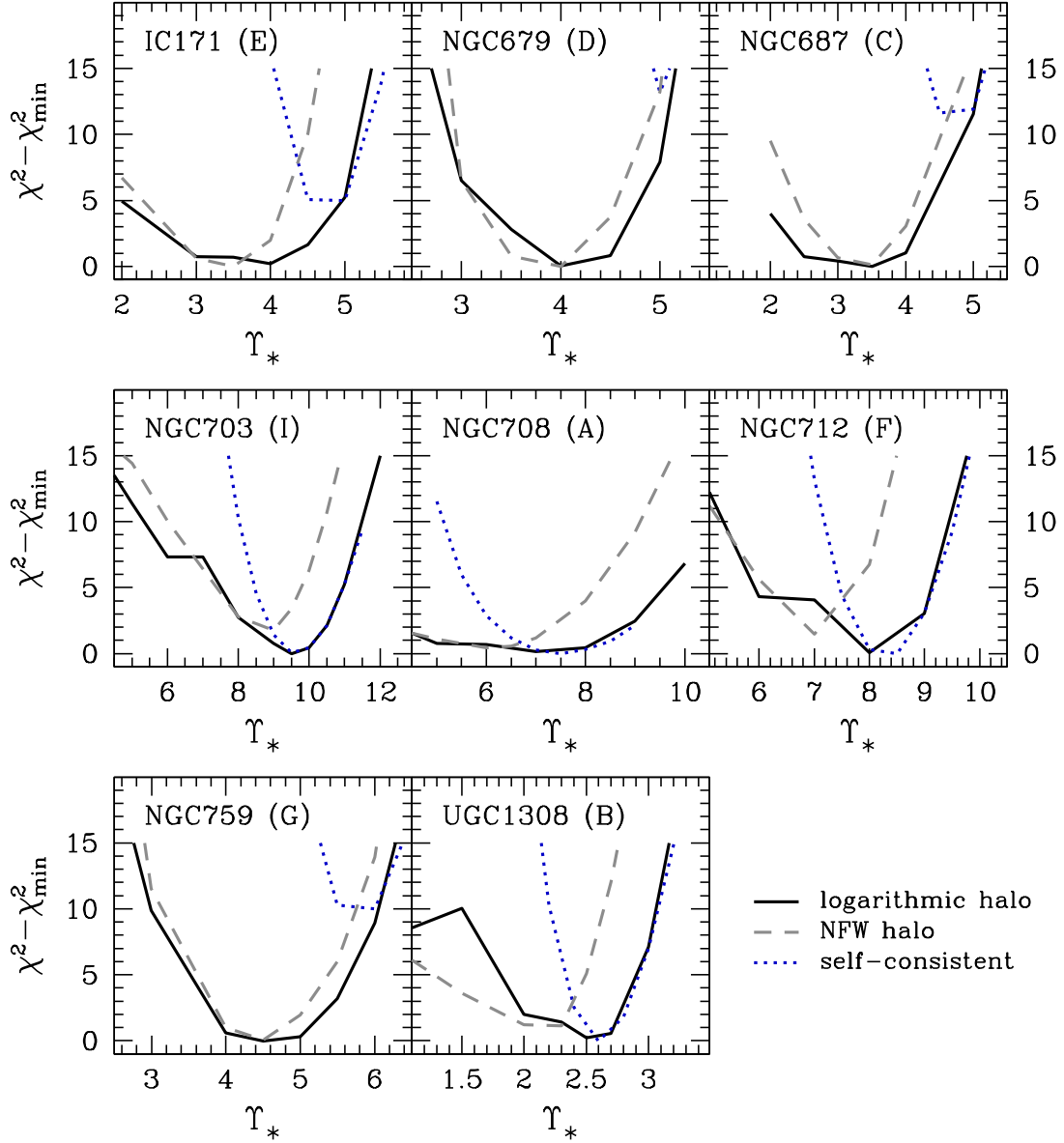


Fig. 9.— Goodness of the kinematic fit χ^2 (cf. Eq. 7) versus mass-to-light ratio Υ_* . Black solid lines are for fits including a logarithmic dark matter halo; grey and dashed lines are for NFW fits; the blue and dotted lines show models where all the mass follows the light ($\rho_{\text{halo}} \equiv 0$ in Eq. 3). For each galaxy the value χ^2_{\min} of the corresponding best-fit model is subtracted.

models (e.g., Gerhard et al. 2001; Tortora et al. 2009). The Abell 262 and Coma samples indicate an anti-correlation between $\Upsilon_*/\Upsilon_{\text{Krou}}$ and

$\langle f_{\text{halo}} \rangle$. Galaxies where the dynamical mass following the light exceeds the Kroupa value by far ($\Upsilon_*/\Upsilon_{\text{Krou}} > 3$) seem to lack matter following the

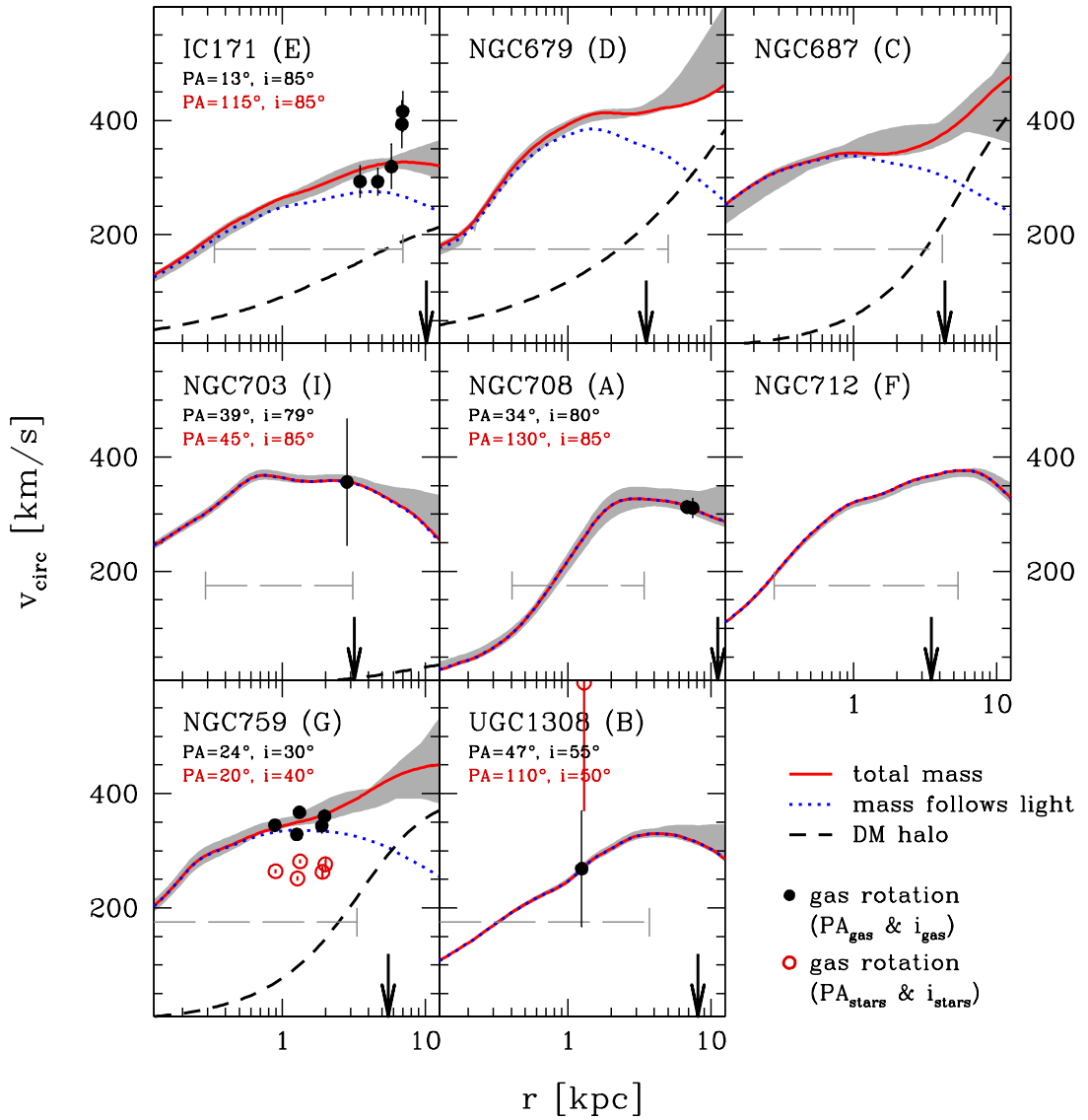


Fig. 10.— Rotation curves of the Abell 262 galaxies derived from dynamical modeling. Blue dotted lines show the contribution of the mass following the light; black dashed lines are for dark halos; red solid lines give the total mass (with the 68% confidence region in grey). Long-dashed lines delimit the region with kinematic observations and the effective radius r_{eff} of each galaxy is marked by an arrow. Where detectable, we also show gas rotation measurements: red open circles correspond to the deprojected gas velocities assuming for the gaseous disk orientation the values of P.A._{stars} and i_{stars} adopted for dynamical models (Table 4); black filled circles are obtained by varying P.A._{gas} and i_{gas} of the gaseous disk to match the gas velocity to the circular velocity predicted by dynamical models. The best-fit P.A._{gas} and i_{gas} are given. The central regions with significant pressure support ($\sigma_{\text{gas}} > 60 \text{ km s}^{-1}$) are omitted.

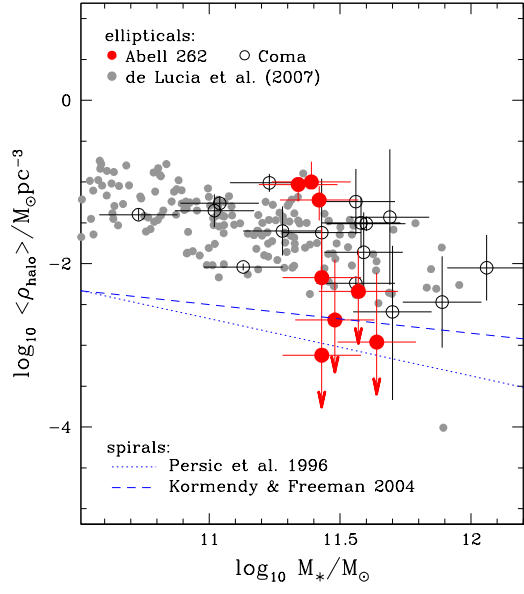


Fig. 12.— Average dark halo density from dynamical modeling, $\langle \rho_{\text{halo}} \rangle$, inside two effective radii as a function of the mass that follows light, M_* , for the galaxies in Abell 262 (red filled circles) and Coma Cluster (open circles, Thomas et al. 2009a). The best-fitting halo densities among all models with a dark halo are plotted. Note that in some galaxies a better fit to the data was achieved without a separate halo component. Predictions from semi-analytic galaxy formation models (De Lucia & Blaizot 2007) are indicated by the grey filled circles. The lines show spiral galaxy scaling relations from two different studies (blue dotted line: Persic et al. 1996b,a; blue dashed line: Kormendy & Freeman 2004).

halo distribution inside r_{eff} ($\langle f_{\text{halo}} \rangle = 0.004$). Not so in galaxies near the Kroupa limit ($\Upsilon_* / \Upsilon_{\text{Krou}} < 1.4$), where the dark-halo mass fraction is at its maximum ($\langle f_{\text{halo}} \rangle = 0.30$). The remaining galaxies are intermediate in both their $\Upsilon_* / \Upsilon_{\text{Krou}}$ and their halo-mass fractions ($\langle f_{\text{halo}} \rangle = 0.22$). We will return to this anti-correlation in Sec. 8.1.

8. Discussion

Fig. 11 provides strong evidence for large central mass-to-light ratios Υ_* in many early-type galaxies – preferably in those with large velocity dispersions σ_{eff} . However, in all gravity-based

methods there is a fundamental degeneracy concerning the interpretation of mass-to-light ratios. Such methods can not uniquely discriminate between luminous and dark matter once they follow similar radial distributions. The distinction is always based on the assumption that the mass density profile of the dark matter differs from that of the luminous matter. Thus, if dark matter in massive ellipticals follows the light closer than that can be resolved by kinematic and/or lensing observations, then the dynamical mass associated to the light might not be stars only.

In fact, if the actual stellar mass-to-light ratio of a galaxy is Υ_{stars} then the stellar mass-density is

$$\rho_{\text{stars}} \equiv \Upsilon_{\text{stars}} \times \nu, \quad (12)$$

while the remaining mass that follows the light,

$$\rho_{\text{DM},*} = (\Upsilon_* - \Upsilon_{\text{stars}}) \times \nu, \quad (13)$$

is a component of dark matter that follows the light – at least so closely that it is captured by Υ_* rather than the nominal ρ_{halo} . Rigorously speaking, any $0 \leq \Upsilon_{\text{stars}} \leq \Upsilon_*$ is equally consistent with the observational data and the dynamically derived dark-matter distributions are correspondingly uncertain. In the following we will discuss the issue in detail.

8.1. Maximum stellar mass and variable initial mass function

One extreme point of view is the assumption that the stellar masses in early-type galaxies are maximal, i.e. $\Upsilon_{\text{stars}} = \Upsilon_*$ (in analogy to the maximum-disk interpretation of spiral galaxy rotation curves; e.g., van Albada & Sancisi 1986). The immediate consequence is that the stellar IMF in early-type galaxies is not universal. While around $\sigma_{\text{eff}} \approx 200 \text{ km s}^{-1}$ there are some galaxies with $\Upsilon_* \approx \Upsilon_{\text{Krou}}$ such galaxies are lacking at higher dispersions σ_{eff} (Fig. 11). Recent attempts to try and measure the stellar IMF directly from near-infrared observations point in the same direction (van Dokkum & Conroy 2010, 2011; Conroy & van Dokkum 2012). These spectroscopically derived IMFs (Salpeter or steeper around $\sigma_{\text{eff}} \approx 300 \text{ km s}^{-1}$) correspond to $\Upsilon_* / \Upsilon_{\text{Krou}} \approx 1.6$ or larger (consistent with Fig. 11) favoring the maximum stellar mass interpretation and an IMF

varying from Kroupa-like at low velocity dispersions to Salpeter (or steeper) in the most massive early-types.

As already noticed for the Coma galaxies (Thomas et al. 2011), we do not see any correlation of $\Upsilon_*/\Upsilon_{\text{Krou}}$ and the SSP ages, metallicities, and α -elements overabundances of the Abell 262 galaxies. Such correlations could be expected if the IMF is variable, since a change in the relative number of low and high-mass stars has some influence on the chemical evolution of the galaxies (e.g., Graves & Faber 2010). However, the stellar IMF acts on the metallicities and element abundances simultaneously with other variable conditions, like the depth of the potential well and star-formation timescale. Hence, the lack of significant stellar-population differences between galaxies with high $\Upsilon_*/\Upsilon_{\text{Krou}}$ on the one hand and galaxies with low $\Upsilon_*/\Upsilon_{\text{Krou}}$ on the other is inconclusive with respect to the IMF.

An intriguing observation is the fact that the galaxies with the highest $\Upsilon_*/\Upsilon_{\text{Krou}}$ in the Abell 262 and Coma clusters ($\Upsilon_*/\Upsilon_{\text{Krou}} > 3$) have the lowest dark matter fractions ($\langle f_{\text{halo}} \rangle \approx 0$). In contrast, galaxies with $\Upsilon_*/\Upsilon_{\text{Krou}} < 1.4$ have the highest dark matter fractions ($\langle f_{\text{halo}} \rangle = 0.30$). Such an anti-correlation between $\Upsilon_*/\Upsilon_{\text{Krou}}$ and f_{halo} can easily be understood if the occasionally large Υ_* in some galaxies results from their dark matter density following the light so closely that it becomes indistinguishable from the stellar mass (at least in the inner parts at $r \lesssim r_{\text{eff}}$ considered here). The more that the actual dark matter of a galaxy leaks into the mass component of our models that follows the light, the less is expected to reside in its nominal halo component ρ_{halo} , resulting in the observed anti-correlation between f_{halo} (measuring only the dark matter in the halo) and $\Upsilon_*/\Upsilon_{\text{Krou}}$ (including also the dark matter following the light). We are not aware of an immediate physical explanation why a more ‘massive’ IMF should occur in galaxies with less dark matter.

8.2. Cold dark matter and halo contraction

One option to further constrain the mass-decomposition of gravity-based models is to incorporate predictions from cosmological simulations that confine the maximum amount of dark matter that can be plausibly attached to a galaxy of a

given stellar mass. Napolitano et al. (2010) found that the velocity dispersions of a large sample of low-redshift early-type galaxies require high central mass-to-light ratios for the stars (consistent with a Salpeter IMF on average) when using such cosmological halos without baryon contraction. Adiabatic contraction (Blumenthal et al. 1986), instead, is able to increase the amount of dark matter in the centers of ellipticals and to lower the required stellar masses towards a Kroupa IMF (see also Napolitano et al. 2011). The recent study of Cappellari et al. (2012), with a not further specified halo-contraction scenario, points against halo contraction to be sufficient to lower the central stellar masses. Lensing studies go in the same direction (Auger et al. 2010) and numerical simulations generally indicate that the classic adiabatic scenario overpredicts the actual contraction of dark matter halos (e.g., Gnedin et al. 2004).

Therefore, while halo contraction could in principle reconcile the observed central dynamical masses with a ‘light’ stellar IMF, the required amount of dark-matter contraction seems to be rather strong. However, this constraint against a ‘light’ IMF is not purely empirical and we here briefly discuss the halo-assembly redshifts of the Abell 262 and Coma galaxies that result in the context of a Kroupa IMF and adiabatic contraction.

An immediate consequence of a universal Kroupa IMF is that some of the mass that follows the light is actually dark matter and needs to be combined with ρ_{halo} , i.e.

$$\rho_{\text{DM},\text{Krou}} = \rho_{\text{halo}} + (\Upsilon_* - \Upsilon_{\text{Krou}}) \times \nu. \quad (14)$$

The effect is to increase the dark matter fractions by about a factor 2, for example it is $\langle f_{\text{DM},\text{Krou}} \rangle = 0.47$ in the Abell 262 sample and similarly in the Coma cluster (Thomas et al. 2011). Dark-matter fractions of $\approx 50\%$ or more are generally found and required in the context of the assumption of a ‘light’ IMF (e.g., Napolitano et al. 2010; Barnabè et al. 2011).

Based on $\rho_{\text{DM},\text{Krou}}$ we derived the dark-halo assembly redshift z_{DM} for the Abell 262 galaxies following Thomas et al. (2011). The basic assumption is that the (decontracted) halo density scales with the mean density of the universe at the assembly epoch, i.e. $\langle \rho_{\text{DM}} \rangle \sim (1 + z_{\text{DM}})^3$. Fig. 13 compares the values of z_{DM} to the star-formation

redshifts z_* calculated from the stellar-population ages.

The derivation of z_{DM} involves the adiabatic decontraction of the dark matter density $\rho_{\text{DM}, \text{Krou}}$. In NGC 687 and UGC 1308 the dynamical Υ_* turns out to be lower than Υ_{Krou} , such that the dark halo to be decontracted for NGC 687 would be exactly cored logarithmic. However, the adiabatic decontraction of cored logarithmic halos is not possible (cf. Thomas et al. 2011) and NGC 687 has been omitted from the analysis. The dynamical model of UGC 1308 formally leaves no space for dark matter at all and the galaxy is not considered furthermore as well.

For the Abell 262 galaxies in Fig. 13 we estimated the uncertainty in z_{DM} that comes from the scatter in the correlation between $\langle \rho_{\text{DM}} \rangle$ and $(1 + z_{\text{DM}})^3$ derived from cosmological simulations (see Fig. 9 in Thomas et al. 2009a). Note that this does not include the uncertainties in ρ_{halo} or any uncertainties related to the contraction scenario. In the majority of Coma galaxies $z_{\text{DM}} \approx z_*$ and the assembly of these galaxies seems to have stopped before $z_{\text{DM}} \approx 1$. In four Coma and three Abell 262 galaxies the stars appear younger than the halo, which indicates a secondary star-formation episode after the main halo assembly.

In one Coma galaxy (GMP 5568) z_{DM} is significantly smaller than z_* . The r_{eff} of GMP 5568 is, however, about 3 times larger than expected for its B -band luminosity, when compared to the rest of the Coma sample. The average of its dark halo density is low because of this change in the physical scale (Thomas et al. 2011). In the Abell 262 cluster we found two galaxies with $z_{\text{DM}} < z_*$ as well (IC 171 and NGC 708). Both galaxies have significant isophote twist (Sec. 6.2) and, in addition, IC 171 has boxy outskirts (Fig. 2) while NGC 708 is a very slow rotator (Fig. 4). The two galaxies may therefore be the remnants of gas-poor binary mergers. The virial theorem predicts the average density to drop by a factor of 4 during such a merger (assuming homology and equal-mass progenitors), whereas the stellar z_* remains constant (assuming similar stellar-population ages for the progenitors) due to the lack of gas to form new stars. Thus, gas-less major mergers move galaxies downward in Fig. 13. In fact, the approximate decrease of the mean density to a quarter of its original value implies assembly redshifts of

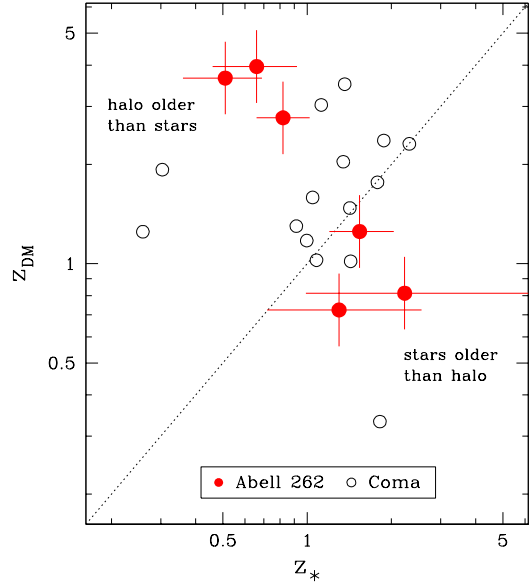


Fig. 13.— Kroupa-IMF based halo-assembly redshifts z_{DM} and star-formation redshifts z_* from stellar-population ages against each other for the galaxies in Abell 262 (filled circles) and Coma Cluster (open circles, Thomas et al. 2011). The dotted line indicates where $z_{\text{DM}} = z_*$. The Coma galaxy GMP 5568 is in the lower right of the diagram.

the hypothetical progenitors to be $z_{\text{DM}} \approx 1.7$ and $z_{\text{DM}} \approx 1.9$ for IC 171 and NGC 708, respectively. Hence, if actually the two galaxies have been recently undergone a major merger, then their progenitors may well have originated from the vicinity of the one-to-one relation in Fig. 13 where we find the majority of early-type galaxies with homogeneously old stellar populations.

Without trying to overinterpret the result given the assumptions going into Fig. 13 (i.e., SSP models, cosmological relations between halo density and formation redshift, and halo contraction), it seems that an universal Kroupa IMF gives a consistent picture for the formation redshifts of our galaxies.

8.3. Violent relaxation

Apart from baryonic contraction, the central dark-matter and stellar mass profiles could also become similar as a result of violent relaxation.

This is usually invoked to explain the orbital structure of elliptical galaxies formed via collapse or merging (Lynden-Bell 1967; Nakamura 2000). Although many of its details are not fully understood (e.g., Arad & Lynden-Bell 2005), some general predictions can be made in the simplest cases of gas-rich (wet) and gas-poor (dry) major mergers, but it is apparent that their general evolution can be more complex.

In this paper, we have added data for some Abell 262 early-type galaxies to those of our previously studied Coma galaxies. We derived the redshifts when the stars and the dark matter halos formed and compared the profiles of the luminous and dark matter components. Some of this information could be interpreted as being consistent with signatures of violent relaxation. In particular, there are two pieces of evidence which are consistent with violent relaxation. The first is the division of the ellipticals into the two merger types as shown in Fig. 13 and explained by models. Indeed recent analyses of the light distributions and dynamics of ellipticals support a picture requiring violent relaxation (Cox et al. 2006; Hopkins et al. 2009a,b; Hoffman et al. 2010) with the conclusion that cuspy ellipticals grew from the mergers of gas-rich spirals while core ellipticals resulted from mergers of earlier gas-poor ellipticals, the orbital and mass distributions of the merger remnants providing a record of their progenitors (cf. Benson 2010 for a review). The second comes from Figs. 10 and 11. If one makes the assumption that the stellar IMF is fixed, then the stellar and luminous matter distributions are close to being the same in several of the galaxies, which is what it would be expected from violent relaxation in the merging which formed them.

Nevertheless, there are problems from some of the other galaxies. The dark matter follows the light closely in both the Abell 262 galaxy NGC 712 and Coma galaxy GMP 1990. They are fast flattened rotators and show the least randomized orbital motions. Moreover, GMP 1990 is a highly flattened system and, taking the model results at face value, the assumption of a Kroupa IMF for this galaxy requires a highly flattened dark matter component $\rho_{\text{DM},*}$. However, as we have not tried to fit a continuous sequence of ever more flattened halos to the kinematic data, it is not clear if a model where all the mass exactly follows the

light is the only way to explain the observational data. In fact, the preference for a high Υ_* in the models could just reflect that the actual dark halo is flatter than the (spherical) ρ_{halo} , though still being rounder than the light distribution – on a level that the data are just better approximated by increasing the mass that follows the light rather than to make the spherical component ρ_{halo} more massive. The actual flattening of the galaxy’s potential might be somewhere in between that of the light and ρ_{halo} (spherical). Lensing galaxies do not show a significant difference between the flattening of their total mass distributions and that of their light, at least not the massive ones (Koopmans et al. 2006; Barnabè et al. 2011). If this also holds for the galaxies studied here, then either the mass that follows the light is indeed stars, or, if not, then there has to be a dark matter component that is as flattened as the stellar distribution ($\epsilon_{\max} \approx 0.6$).

Admittedly, we are dealing with a small sample of imperfect observations, but at present it appears that the best one can conclude is that these data do not offer strong proof for violent relaxation being a major mechanism to make sufficiently similar the distributions of stars and dark matter.

Further numerical investigations are required to test if a predominantly collisionless-accretion growth of the outer parts of massive early-types can lead to a similarisation of the mass-density profiles of stellar and dark matter. Simulations show that accreted stars have shallower radial mass profiles than in-situ formed stars (Naab et al. 2009). Since the dark-matter accretion is collisionless as well, the stellar and dark-matter profiles around r_{eff} (where accreted stars are expected to dominate) might be similar.

Finally, we note that it seems unlikely that uncertainties in the modeling process (due to limited kinematic observations and/or symmetry assumptions) can explain the particular large mass-to-light ratios of some early-type galaxies. Mainly, because our total (i.e., luminous and dark) dynamical masses are consistent with completely independent results from strong gravitational lensing and from our gas rotation velocities being consistent with the circular velocities derived from dynamical modeling.

9. Summary

We presented new radially resolved spectroscopy of 8 early-type galaxies in the Abell 262 cluster. We measured the stellar rotation, velocity dispersion, and the H_3 and H_4 coefficients of the line-of-sight velocity distribution along the major axis, minor axis and an intermediate axis. In addition, we derived line index profiles of Mg, Fe and H β . The ionized-gas velocity and velocity dispersion were measured along different axes of 6 sample galaxies. Axisymmetric orbit-based dynamical models were used to derive (1) the mass-to-light ratio of all the mass that follows the light and (2) the dark halo parameters. The analysis of the ionized-gas kinematics gave a valuable consistency check for the circular velocity (and total mass distribution) predicted by dynamical modeling. Line-strength indices were analyzed by SSP models to derive the galaxies' ages, metallicities, and α -elements abundances.

This study of Abell 262 galaxies complements our earlier work on a similar, though larger, sample of early-type galaxies in Coma. While the Coma galaxies were selected to be mostly flattened, the Abell 262 galaxies regarded here appear predominantly round on the sky.

Three of the new Abell 262 galaxies show clear evidence for a mass component that is unrelated to the light with a statistical significance of at least 3σ . In one further galaxy the statistical evidence for dark matter is slightly lower (about 2σ). In four Abell 262 galaxies the addition of mass that is distinct from the luminosity distribution does not improve the fit to the observed kinematics significantly.

We find that the dynamical mass-to-light ratios $\Upsilon_* = \rho_*/\nu$, where ρ_* is the density of all the mass that follows the light, increase with the stellar velocity dispersion σ_{eff} (averaged inside r_{eff}), while the corresponding stellar-population values are almost constant. Many galaxies around $\sigma_{\text{eff}} \approx 200 \text{ km s}^{-1}$ have Υ_* consistent with a Kroupa IMF. Around $\sigma_{\text{eff}} \approx 300 \text{ km s}^{-1}$ the Υ_* are typically 2 times larger than for a Kroupa IMF.

This could reflect a change in the stellar IMF with σ_{eff} . However, we also find an anti-correlation between the average fraction of mass in the halo, f_{halo} , and the ratio $\Upsilon_*/\Upsilon_{\text{Krou}}$. The galaxies with the largest $\Upsilon_*/\Upsilon_{\text{Krou}}$ have the lowest

halo-mass fractions inside r_{eff} and vice versa. A possible explanation for this finding is a dark matter distribution that follows the light very closely in massive galaxies and contaminates the measured Υ_* , while it is more distinct from the light in lower-mass systems.

If there is indeed some ambiguity between stellar and dark mass, then the finding of $\Upsilon_* > \Upsilon_{\text{Krou}}$ does not necessarily indicate a 'massive' IMF. In fact, galaxies where the dynamical mass that follows the light is in excess of a Kroupa stellar population do not differ in terms of their stellar population ages, metallicities and α -elements abundances from galaxies where this is not the case. Taken at face value, our dynamical mass models are therefore as consistent with a universal IMF, as they are with a variable IMF.

However, Conroy & van Dokkum (2012) have presented stellar-population models with a variable IMF that do show a correlation with α -overabundance which can partly explain the large amount of mass that follows the light in massive early-type galaxies. Nevertheless, even these models produce stellar mass-to-light ratios that are smaller than the dynamical ones for the mass that follows the light. Therefore, a combination of both, IMF variation and some degeneracy between the mass profiles of stellar and dark matter could give a consistent explanation for our observations. If the IMF indeed varies from galaxy to galaxy according to the average star-formation rate, as implicated by the correlation with α -overabundance, then the assumption of a constant stellar mass-to-light ratio *inside* a galaxy should be relaxed in future dynamical and lensing models.

Finally, we have derived halo-assembly redshifts for the Abell 262 galaxies by calibrating the average dark matter density inside $2r_{\text{eff}}$ using cosmological N -body simulations. As in Coma early-types, the typical assembly redshift of the halos is around $z_{\text{DM}} \approx 1 - 3$.

E.M.C. acknowledges the Max-Planck-Institut für extraterrestrische Physik for hospitality while this paper was in progress. E.M.C. receives support by Padua University through grants CPDA089220/08 and CPDR095001/09 and by Italian Space Agency through grant ASI-INAF I/009/10/0. J.T. acknowledges the Padua University for hospitality while this paper was in

progress. Support for Program number HST-GO-10884.0-A was provided by NASA through a grant from the Space Telescope Science Institute which is operated by the Association of Universities for Research in Astronomy, Incorporated, under NASA contract NAS5-26555. This work was in part supported by the Chinese National Science Foundation (Grant No. 10821061) and the National Basic Research Program of China (Grant No. 2007CB815406). We also gratefully acknowledge the Chinese Academy of Sciences and Max-Planck-Institut für Extraterrestrische Physik that partially supported this work. The authors wish to acknowledge the anonymous referee who's comments substantially improved this paper.

REFERENCES

- Abell, G. O., Corwin, Jr., H. G., & Olowin, R. P. 1989, ApJS, 70, 1
- Arad, I., & Lynden-Bell, D. 2005, MNRAS, 361, 385
- Auger, M. W., Treu, T., Bolton, A. S., Gavazzi, R., Koopmans, L. V. E., Marshall, P. J., Bundy, K., & Moustakas, L. A. 2009, ApJ, 705, 1099
- Auger, M. W., Treu, T., Gavazzi, R., Bolton, A. S., Koopmans, L. V. E., & Marshall, P. J. 2010, ApJ, 721, L163
- Baggett, S., & McMaster, M. 2002, WFPC2 Data Handbook, Version 4.0 (Baltimore: STScI)
- Barnabè, M., Czoske, O., Koopmans, L. V. E., Treu, T., & Bolton, A. S. 2011, MNRAS, 415, 2215
- Beifiori, A., Maraston, C., Thomas, D., & Johansson, J. 2010, ArXiv e-prints
- Bender, R., & Moellenhoff, C. 1987, A&A, 177, 71
- Benson, A. J. 2010, Phys. Rep., 495, 33
- Bernardi, M., Alonso, M. V., da Costa, L. N., Willmer, C. N. A., Wegner, G., Pellegrini, P. S., Ritè, C., & Maia, M. A. G. 2002, AJ, 123, 2990
- Bertola, F., Cinzano, P., Corsini, E. M., Rix, H.-W., & Zeilinger, W. W. 1995, ApJ, 448, L13
- Binney, J., & Tremaine, S. 1987, Galactic Dynamics (Princeton: Princeton Univ. Press)
- Blanton, E. L., Sarazin, C. L., McNamara, B. R., & Clarke, T. E. 2004, ApJ, 612, 817
- Blumenthal, G. R., Faber, S. M., Flores, R., & Primack, J. R. 1986, ApJ, 301, 27
- Cappellari, M., & Emsellem, E. 2004, PASP, 116, 138
- Cappellari, M., et al. 2006, MNRAS, 366, 1126
- . 2012, Nature, 484, 485
- Clarke, T. E., Blanton, E. L., Sarazin, C. L., Anderson, L. D., Gopal-Krishna, Douglass, E. M., & Kassim, N. E. 2009, ApJ, 697, 1481
- Colless, M., Burstein, D., Davies, R. L., McMahan, R. K., Saglia, R. P., & Wegner, G. 1999, MNRAS, 303, 813
- Colless, M., Burstein, D., Wegner, G., Saglia, R. P., McMahan, R., Davies, R. L., Bertschinger, E., & Bagley, G. 1993, MNRAS, 262, 475
- Colless, M., Saglia, R. P., Burstein, D., Davies, R. L., McMahan, R. K., & Wegner, G. 2001, MNRAS, 321, 277
- Collobert, M., Sarzi, M., Davies, R. L., Kuntschner, H., & Colless, M. 2006, MNRAS, 370, 1213
- Conroy, C., & van Dokkum, P. 2012, ArXiv e-prints
- Corsini, E. M., Wegner, G., Saglia, R. P., Thomas, J., Bender, R., & Thomas, D. 2008, ApJS, 175, 462
- Cox, T. J., Dutta, S. N., Di Matteo, T., Hernquist, L., Hopkins, P. F., Robertson, B., & Springel, V. 2006, ApJ, 650, 791
- Dalcanton, J. J., & Stilp, A. M. 2010, ApJ, 721, 547
- David, L. P., Slyz, A., Jones, C., Forman, W., Vrtilek, S. D., & Arnaud, K. A. 1993, ApJ, 412, 479
- De Lucia, G., & Blaizot, J. 2007, MNRAS, 375, 2
- De Lucia, G., Springel, V., White, S. D. M., Croton, D., & Kauffmann, G. 2006, MNRAS, 366, 499
- de Vaucouleurs, G., de Vaucouleurs, A., Corwin, Jr., H. G., Buta, R. J., Paturel, G., & Fouque, P. 1991, Third Reference Catalogue of Bright Galaxies (Volume 1-3, XII, 2069 pp. 7 figs.. Springer-Verlag Berlin Heidelberg New York)
- Faber, S. M., Friel, E. D., Burstein, D., & Gaskell, C. M. 1985, ApJS, 57, 711
- Gavazzi, G., Boselli, A., Donati, A., Franzetti, P., & Scodéglio, M. 2003, A&A, 400, 451
- Gavazzi, G., Pierini, D., Boselli, A., & Tuffs, R. 1996, A&AS, 120, 489

- Gerhard, O., Kronawitter, A., Saglia, R. P., & Bender, R. 2001, AJ, 121, 1936
- Gerhard, O. E. 1993, MNRAS, 265, 213
- Gnedin, O. Y., Kravtsov, A. V., Klypin, A. A., & Nagai, D. 2004, ApJ, 616, 16
- González, J. J. 1993, PhD thesis, Univ. California
- Gorgas, J., Efstathiou, G., & Aragon Salamanca, A. 1990, MNRAS, 245, 217
- Graves, G. J., & Faber, S. M. 2010, ApJ, 717, 803
- Hoffman, L., Cox, T. J., Dutta, S., & Hernquist, L. 2010, ApJ, 723, 818
- Hopkins, P. F., Cox, T. J., Dutta, S. N., Hernquist, L., Kormendy, J., & Lauer, T. R. 2009a, ApJS, 181, 135
- Hopkins, P. F., Lauer, T. R., Cox, T. J., Hernquist, L., & Kormendy, J. 2009b, ApJS, 181, 486
- Koopmans, L. V. E., Treu, T., Bolton, A. S., Burles, S., & Moustakas, L. A. 2006, ApJ, 649, 599
- Kormendy, J., & Freeman, K. C. 2004, in IAU Symposium, Vol. 220, Dark Matter in Galaxies, ed. S. Ryder, D. Pisano, M. Walker, & K. Freeman, 377
- Krajnović, D., Cappellari, M., Emsellem, E., McDermid, R. M., & de Zeeuw, P. T. 2005, MNRAS, 357, 1113
- Kroupa, P. 2001, MNRAS, 322, 231
- Lauer, T. R., et al. 2005, AJ, 129, 2138
- Lynden-Bell, D. 1967, MNRAS, 136, 101
- Magorrian, J. 1999, MNRAS, 302, 530
- Maraston, C. 1998, MNRAS, 300, 872
- . 2005, MNRAS, 362, 799
- Markwardt, C. B. 2009, in Astronomical Society of the Pacific Conference Series, Vol. 411, Astronomical Data Analysis Software and Systems XVIII, ed. D. A. Bohlender, D. Durand, & P. Dowler, 251
- Martini, P., Regan, M. W., Mulchaey, J. S., & Pogge, R. W. 2003, ApJS, 146, 353
- McMaster, M., & Biretta, J. 2008, WFPC2 Instrument Handbook, Version 10.0 (Baltimore: STScI)
- Mehlert, D., Saglia, R. P., Bender, R., & Wegner, G. 1998, A&A, 332, 33
- . 2000, A&AS, 141, 449
- Mehlert, D., Thomas, D., Saglia, R. P., Bender, R., & Wegner, G. 2003, A&A, 407, 423
- Moré, J. J., Garbow, B. S., & Hillstrom, K. E. 1980, User guide for MINPACK-1 (Technical Report ANL-80-74, Argonne National Laboratory, Argonne, IL)
- Naab, T., Johansson, P. H., & Ostriker, J. P. 2009, ApJ, 699, L178
- Nakamura, T. K. 2000, ApJ, 531, 739
- Napolitano, N. R., Romanowsky, A. J., & Tortora, C. 2010, MNRAS, 405, 2351
- Napolitano, N. R., et al. 2011, MNRAS, 411, 2035
- Navarro, J. F., Frenk, C. S., & White, S. D. M. 1996, ApJ, 462, 563
- Neill, J. D., Brodie, J. P., Craig, W. W., Hailey, C. J., & Misch, A. A. 2001, ApJ, 548, 550
- Nelan, J. E., Smith, R. J., Hudson, M. J., Wegner, G. A., Lucey, J. R., Moore, S. A. W., Quinney, S. J., & Suntzeff, N. B. 2005, ApJ, 632, 137
- Osterbrock, D. E. 1989, Astrophysics of Gaseous Nebulae and Active Galactic Nuclei (Sausalito, California, University Science Books)
- Osterbrock, D. E., Fulbright, J. P., Martel, A. R., Keane, M. J., Trager, S. C., & Basri, G. 1996, PASP, 108, 277
- Paturel, G., Petit, C., Prugniel, P., Theureau, G., Rousseau, J., Brouty, M., Dubois, P., & Cambrésy, L. 2003, A&A, 412, 45
- Persic, M., Salucci, P., & Stel, F. 1996a, MNRAS, 283, 1102
- . 1996b, MNRAS, 281, 27

- Pignatelli, E., et al. 2001, MNRAS, 323, 188
- Pu, S. B., Saglia, R. P., Fabricius, M. H., Thomas, J., Bender, R., & Han, Z. 2010, A&A, 516, A4
- Richstone, D. O., & Tremaine, S. 1988, ApJ, 327, 82
- Rusli, S. P., Thomas, J., Erwin, P., Saglia, R. P., Nowak, N., & Bender, R. 2010, MNRAS, 1625
- Saglia, R. P., Bertschinger, E., Baggley, G., Burstein, D., Colless, M., Davies, R. L., McManan, Jr., R. K., & Wegner, G. 1997a, ApJS, 109, 79
- Saglia, R. P., Burstein, D., Baggley, G., Davies, R. L., Bertschinger, E., Colless, M. M., McManan, Jr., R. K., & Wegner, G. 1997b, MNRAS, 292, 499
- Saglia, R. P., Colless, M., Burstein, D., Davies, R. L., McMahan, R. K., & Wegner, G. 2001, MNRAS, 324, 389
- Saglia, R. P., et al. 2010, A&A, 509, A61
- Salpeter, E. E. 1955, ApJ, 121, 161
- Sánchez-Blázquez, P., et al. 2006, MNRAS, 371, 703
- Sarzi, M., et al. 2006, MNRAS, 366, 1151
- Sato, K., Matsushita, K., & Gastaldello, F. 2009, PASJ, 61, 365
- Schwarzschild, M. 1979, ApJ, 232, 236
- Struble, M. F., & Rood, H. J. 1999, ApJS, 125, 35
- Thomas, D., Maraston, C., & Bender, R. 2003, MNRAS, 339, 897
- Thomas, D., Maraston, C., Bender, R., & Mendes de Oliveira, C. 2005a, ApJ, 621, 673
- Thomas, J., Jesseit, R., Naab, T., Saglia, R. P., Burkert, A., & Bender, R. 2007a, MNRAS, 381, 1672
- Thomas, J., Saglia, R. P., Bender, R., Thomas, D., Corsini, E. M., & Wegner, G. 2011, MNRAS, in prep.
- Thomas, J., Saglia, R. P., Bender, R., Thomas, D., Gebhardt, K., Magorrian, J., Corsini, E. M., & Wegner, G. 2005b, MNRAS, 360, 1355
- . 2007b, MNRAS, 382, 657
- . 2009a, ApJ, 691, 770
- Thomas, J., Saglia, R. P., Bender, R., Thomas, D., Gebhardt, K., Magorrian, J., & Richstone, D. 2004, MNRAS, 353, 391
- Thomas, J., et al. 2009b, MNRAS, 393, 641
- Tortora, C., Napolitano, N. R., Romanowsky, A. J., Capaccioli, M., & Covone, G. 2009, MNRAS, 396, 1132
- Treu, T., Auger, M. W., Koopmans, L. V. E., Gavazzi, R., Marshall, P. J., & Bolton, A. S. 2010, ApJ, 709, 1195
- van Albada, T. S., & Sancisi, R. 1986, R. Soc. London Phil. Trans. Series A, 320, 447
- van den Bosch, R. C. E., & van de Ven, G. 2009, MNRAS, 398, 1117
- van der Marel, R. P., & Franx, M. 1993, ApJ, 407, 525
- van Dokkum, P. G., & Conroy, C. 2010, Nature, 468, 940
- . 2011, ApJ, 735, L13
- Wechsler, R. H., Bullock, J. S., Primack, J. R., Kravtsov, A. V., & Dekel, A. 2002, ApJ, 568, 52
- Wegner, G., Colless, M., Baggley, G., Davies, R. L., Bertschinger, E., Burstein, D., McManan, Jr., R. K., & Saglia, R. P. 1996, ApJS, 106, 1
- Wegner, G., Colless, M., Saglia, R. P., McMahan, R. K., Davies, R. L., Burstein, D., & Baggley, G. 1999, MNRAS, 305, 259
- Wegner, G., Corsini, E. M., Saglia, R. P., Bender, R., Merkl, D., Thomas, D., Thomas, J., & Mehlert, D. 2002, A&A, 395, 753
- Wegner, G., & Grogin, N. A. 2008, AJ, 136, 1
- Wegner, G., et al. 2003, AJ, 126, 2268
- Worthey, G. 1994, ApJS, 95, 107
- Worthey, G., Faber, S. M., Gonzalez, J. J., & Burstein, D. 1994, ApJS, 94, 687

Worthey, G., & Ottaviani, D. L. 1997, ApJS, 111,
377

TABLE 5
PHOTOMETRIC PARAMETERS OF THE SAMPLE GALAXIES.

a [arcsec]	μ_R [mag arcsec $^{-2}$]	e	PA [°]	Δx_c [arcsec]	Δy_c [arcsec]	Err. ^a [arcsec]	a_3/a $\times 100$	b_3/a $\times 100$	a_4/a $\times 100$	b_4/a $\times 100$	a_6/a $\times 100$	b_6/a $\times 100$	Err. ^b
IC 171													
0.202 ± 0.000	16.927 ± 0.010	0.000 ± 0.000	90.0 ± 0.0	0.127	0.594	0.000	0.00	0.00	0.00	0.00	0.00	0.00	0.00
0.644 ± 0.081	17.005 ± 0.014	0.317 ± 0.121	66.7 ± 16.1	0.000	0.000	0.057	-2.21	3.91	2.94	-1.95	2.36	-1.64	1.25
1.104 ± 0.010	17.146 ± 0.015	0.182 ± 0.010	78.4 ± 1.9	0.024	0.006	0.007	-0.94	0.85	0.55	0.03	-0.18	-0.45	0.41
1.482 ± 0.007	17.338 ± 0.014	0.186 ± 0.006	82.3 ± 1.1	0.036	0.012	0.005	-0.67	0.85	0.27	0.06	-0.28	-0.01	0.29
1.797 ± 0.006	17.530 ± 0.012	0.170 ± 0.004	84.1 ± 0.7	0.048	0.006	0.004	-0.23	0.77	-0.07	-0.02	-0.30	-0.09	0.17
2.118 ± 0.006	17.690 ± 0.011	0.176 ± 0.003	85.9 ± 0.7	0.061	0.000	0.004	0.24	0.75	-0.21	0.07	-0.34	-0.05	0.12
2.455 ± 0.007	17.845 ± 0.012	0.186 ± 0.003	88.5 ± 0.6	0.079	-0.006	0.005	0.51	0.75	-0.23	0.13	-0.12	0.16	0.15
2.805 ± 0.009	17.993 ± 0.010	0.187 ± 0.004	91.4 ± 0.7	0.091	-0.006	0.006	-0.91	-0.49	0.14	0.18	-0.07	0.40	0.19
3.240 ± 0.012	18.149 ± 0.009	0.205 ± 0.004	95.4 ± 0.7	0.109	-0.006	0.009	-0.96	0.79	0.62	-0.19	0.28	0.09	0.22
3.760 ± 0.013	18.322 ± 0.008	0.222 ± 0.004	98.1 ± 0.6	0.121	-0.024	0.009	-0.69	1.04	0.28	-0.44	0.32	-0.17	0.19
4.356 ± 0.011	18.476 ± 0.007	0.239 ± 0.003	99.8 ± 0.4	0.158	-0.048	0.008	-0.51	0.81	0.16	-0.20	-0.00	-0.14	0.20
4.978 ± 0.013	18.632 ± 0.005	0.247 ± 0.003	101.6 ± 0.4	0.212	-0.067	0.009	-0.03	0.97	-0.38	0.15	-0.28	0.12	0.15
5.678 ± 0.018	18.796 ± 0.005	0.252 ± 0.003	102.2 ± 0.5	0.248	-0.091	0.013	0.45	0.79	-0.84	0.19	-0.57	0.59	0.18
6.422 ± 0.021	18.958 ± 0.005	0.257 ± 0.003	101.6 ± 0.5	0.339	-0.115	0.015	0.72	0.57	-0.29	0.28	-0.49	0.90	0.20
7.260 ± 0.024	19.118 ± 0.004	0.253 ± 0.004	102.0 ± 0.5	0.364	-0.073	0.017	0.37	0.36	-0.85	0.82	-0.61	0.35	0.25
8.208 ± 0.030	19.273 ± 0.005	0.255 ± 0.004	99.9 ± 0.6	0.388	-0.061	0.021	0.90	0.90	-1.37	0.81	-0.30	0.53	0.27
9.037 ± 0.034	19.431 ± 0.005	0.234 ± 0.004	100.4 ± 0.6	0.400	-0.073	0.024	1.47	0.59	-1.52	0.91	-0.70	0.22	0.22
9.978 ± 0.037	19.593 ± 0.005	0.232 ± 0.004	100.0 ± 0.7	0.345	-0.085	0.026	1.29	1.46	-0.99	0.91	-0.83	-0.38	0.24
11.055 ± 0.038	19.750 ± 0.004	0.233 ± 0.004	98.5 ± 0.6	0.291	-0.085	0.027	1.57	1.45	-0.70	0.99	-0.56	-0.60	0.30
12.124 ± 0.044	19.903 ± 0.004	0.233 ± 0.004	98.0 ± 0.6	0.255	-0.133	0.031	1.22	1.24	-0.85	0.93	-0.37	-0.26	0.33
13.184 ± 0.044	20.072 ± 0.005	0.220 ± 0.004	98.2 ± 0.6	0.200	-0.224	0.031	1.46	0.82	-1.32	1.28	-0.69	-0.22	0.32
14.406 ± 0.056	20.232 ± 0.005	0.229 ± 0.004	99.1 ± 0.7	0.206	-0.236	0.040	1.72	1.61	-2.00	0.73	-0.30	-0.32	0.29
15.821 ± 0.057	20.390 ± 0.005	0.245 ± 0.004	99.9 ± 0.6	0.182	-0.248	0.040	1.96	1.25	-1.64	0.55	-0.18	-0.26	0.25
17.105 ± 0.071	20.548 ± 0.005	0.245 ± 0.004	99.6 ± 0.7	0.285	-0.285	0.050	1.88	1.15	-1.82	0.49	-0.90	-0.55	0.28
18.323 ± 0.076	20.697 ± 0.005	0.233 ± 0.005	99.6 ± 0.7	0.297	-0.218	0.054	1.96	1.10	-1.02	0.07	-1.01	-0.55	0.31
19.761 ± 0.078	20.854 ± 0.005	0.244 ± 0.004	100.3 ± 0.7	0.182	-0.261	0.055	1.06	0.36	-0.96	-0.27	-0.51	-0.84	0.35
21.221 ± 0.116	21.005 ± 0.005	0.240 ± 0.006	100.4 ± 0.9	0.176	0.042	0.082	1.13	0.29	-0.28	0.41	-0.99	-0.08	0.48
22.722 ± 0.122	21.152 ± 0.006	0.235 ± 0.006	100.9 ± 0.9	0.048	0.176	0.086	1.18	-0.26	0.36	0.62	0.07	0.25	0.58
24.346 ± 0.116	21.303 ± 0.006	0.234 ± 0.005	101.5 ± 0.8	-0.121	0.055	0.082	0.78	-0.57	-0.44	-0.21	0.25	-0.57	0.54
26.243 ± 0.151	21.465 ± 0.006	0.248 ± 0.006	107.5 ± 0.9	0.006	0.097	0.107	1.00	-1.23	-1.30	0.58	0.56	-1.39	0.55
28.901 ± 0.193	21.634 ± 0.006	0.267 ± 0.007	110.7 ± 1.0	-0.127	0.158	0.137	0.55
31.554 ± 0.159	21.809 ± 0.008	0.280 ± 0.005	111.0 ± 0.7	-0.703	-0.103	0.113	-0.02	-0.78	-2.78	1.14	-0.34	-0.92	0.27
33.807 ± 0.199	21.985 ± 0.009	0.299 ± 0.006	112.1 ± 0.8	-1.194	-0.073	0.141	0.09	-0.38	-3.40	1.38	0.12	-0.32	0.30
36.215 ± 0.273	22.142 ± 0.010	0.303 ± 0.007	113.2 ± 1.0	-1.521	0.079	0.193	0.30
38.634 ± 0.335	22.284 ± 0.011	0.310 ± 0.008	114.7 ± 1.1	-1.721	-0.115	0.237	0.30
40.684 ± 0.377	22.426 ± 0.013	0.312 ± 0.009	115.8 ± 1.2	-1.927	-0.230	0.267	0.30
42.867 ± 0.632	22.557 ± 0.014	0.322 ± 0.014	115.3 ± 1.9	-2.273	-0.297	0.447	0.30
45.373 ± 0.961	22.683 ± 0.015	0.336 ± 0.020	114.7 ± 2.5	-2.479	-0.727	0.680	0.30
48.122 ± 0.969	22.830 ± 0.017	0.356 ± 0.018	114.3 ± 2.3	-2.254	-0.473	0.685	0.30
50.153 ± 0.995	22.979 ± 0.017	0.363 ± 0.018	115.2 ± 2.2	-2.085	-0.194	0.704	0.30
NGC 679													
0.017 ± 0.000	15.105 ± 0.010	0.000 ± 0.000	90.0 ± 0.0	-0.021	0.025	0.000	0.00	0.00	0.00	0.00	0.00	0.00	0.00
0.047 ± 0.005	15.221 ± 0.004	0.053 ± 0.133	28.0 ± 76.2	0.000	0.000	0.003	0.73	0.30	1.86	6.99	0.64	-0.54	1.64
0.098 ± 0.000	15.398 ± 0.007	0.041 ± 0.007	30.2 ± 4.8	0.003	-0.004	0.000	-0.23	-0.53	0.03	0.04	0.06	0.07	0.35
0.148 ± 0.001	15.573 ± 0.008	0.037 ± 0.011	55.6 ± 9.0	0.009	-0.012	0.001	-0.42	-1.27	-0.54	0.09	-0.50	-0.07	0.60
0.215 ± 0.002	15.736 ± 0.008	0.052 ± 0.012	128.5 ± 6.9	0.004	-0.028	0.001	0.06	-0.39	2.37	-0.16	-0.43	-0.81	0.28
0.284 ± 0.002	15.899 ± 0.007	0.073 ± 0.007	131.3 ± 3.0	0.003	-0.027	0.001	-0.12	-0.12	1.22	-0.98	-1.38	-0.48	0.19
0.354 ± 0.002	16.077 ± 0.005	0.100 ± 0.008	159.8 ± 2.5	-0.000	-0.006	0.002	0.19
0.754 ± 0.002	16.247 ± 0.002	0.091 ± 0.004	150.1 ± 1.4	0.000	0.012	0.002	-0.49	0.21	-0.99	-0.48	-0.48	0.28	0.24
0.922 ± 0.002	16.416 ± 0.002	0.092 ± 0.003	146.5 ± 0.9	0.001	0.020	0.001	-0.10	-0.06	-0.18	0.28	0.53	-0.53	0.21
1.126 ± 0.002	16.588 ± 0.002	0.110 ± 0.002	148.5 ± 0.6	0.001	0.014	0.001	-0.02	-0.27	-0.23	-0.23	-0.19	0.05	0.18
1.320 ± 0.002	16.754 ± 0.002	0.098 ± 0.002	149.6 ± 0.7	0.000	0.017	0.002	-0.08	0.13	-0.07	0.22	-0.57	-0.04	0.19
1.529 ± 0.002	16.925 ± 0.001	0.093 ± 0.002	148.8 ± 0.6	-0.002	0.019	0.002	-0.25	-0.04	0.08	0.03	-0.02	0.18	0.17
1.750 ± 0.003	17.095 ± 0.001	0.091 ± 0.002	149.6 ± 0.8	-0.001	0.023	0.002	-0.06	-0.07	-0.16	0.13	-0.10	-0.56	0.19
1.983 ± 0.003	17.263 ± 0.001	0.086 ± 0.002	149.2 ± 0.8	0.004	0.020	0.002	0.09	0.13	-0.08	0.10	0.04	0.11	0.23
2.253 ± 0.004	17.428 ± 0.001	0.091 ± 0.002	148.7 ± 0.8	-0.005	0.015	0.003	0.22	0.28	-0.05	-0.09	-0.27	0.00	0.22
2.565 ± 0.003	17.592 ± 0.001	0.095 ± 0.001	150.2 ± 0.5	-0.001	0.024	0.002	-0.16	0.11	0.02	-0.18	0.08	-0.18	0.11
2.883 ± 0.003	17.753 ± 0.001	0.099 ± 0.001	150.8 ± 0.4	-0.008	0.025	0.002	-0.30	0.09	-0.03	-0.19	0.04	-0.08	0.09
3.218 ± 0.002	17.911 ± 0.001	0.087 ± 0.001	150.9 ± 0.4	-0.002	0.025	0.002	-0.29	0.07	-0.12	-0.11	-0.01	-0.15	0.07

TABLE 5—Continued

a [arcsec]	μ_R [mag arcsec $^{-2}$]	e	PA [$^{\circ}$]	Δx_c [arcsec]	Δy_c [arcsec]	Err. ^a [arcsec]	a_3/a $\times 100$	b_3/a $\times 100$	a_4/a $\times 100$	b_4/a $\times 100$	a_6/a $\times 100$	b_6/a $\times 100$	Err. ^b
3.549 ± 0.003	18.068 ± 0.001	0.080 ± 0.001	150.7 ± 0.4	-0.000	0.026	0.002	-0.16	-0.04	-0.05	-0.04	-0.03	-0.10	0.08
3.877 ± 0.003	18.226 ± 0.001	0.076 ± 0.001	150.4 ± 0.4	0.000	0.027	0.002	-0.12	-0.13	-0.04	-0.02	-0.00	-0.12	0.06
4.218 ± 0.004	18.380 ± 0.001	0.074 ± 0.001	150.9 ± 0.5	0.000	0.021	0.003	-0.23	-0.09	-0.04	0.09	0.03	-0.08	0.09
4.564 ± 0.004	18.530 ± 0.001	0.073 ± 0.001	150.2 ± 0.5	-0.002	0.023	0.003	-0.26	-0.02	-0.09	0.12	-0.03	-0.05	0.08
4.918 ± 0.004	18.677 ± 0.001	0.073 ± 0.001	149.9 ± 0.5	-0.003	0.022	0.003	-0.17	-0.04	-0.24	0.20	-0.06	-0.15	0.08
5.277 ± 0.004	18.819 ± 0.001	0.068 ± 0.001	149.2 ± 0.5	-0.005	0.025	0.003	-0.22	0.02	-0.24	0.13	0.05	-0.11	0.10
5.664 ± 0.005	18.958 ± 0.001	0.065 ± 0.001	149.8 ± 0.6	-0.007	0.040	0.004	-0.18	0.01	0.01	0.19	0.23	-0.01	0.09
6.091 ± 0.007	19.090 ± 0.001	0.064 ± 0.002	151.6 ± 0.7	-0.020	0.059	0.005	-0.25	0.07	0.02	0.16	-0.01	-0.04	0.15
6.552 ± 0.008	19.217 ± 0.001	0.067 ± 0.002	151.8 ± 0.8	-0.024	0.044	0.006	-0.13	0.10	-0.16	0.01	-0.22	-0.34	0.17
7.042 ± 0.009	19.338 ± 0.001	0.067 ± 0.002	150.7 ± 0.8	-0.029	0.055	0.006	0.02	0.09	-0.23	-0.00	0.07	-0.15	0.12
7.553 ± 0.008	19.452 ± 0.001	0.067 ± 0.002	149.6 ± 0.7	-0.017	0.074	0.006	0.06	0.12	-0.36	-0.17	-0.12	-0.12	0.13
8.064 ± 0.010	19.561 ± 0.001	0.064 ± 0.002	148.6 ± 0.8	-0.022	0.085	0.007	0.28	-0.24	-0.51	-0.07	-0.29	-0.11	0.13
8.595 ± 0.010	19.661 ± 0.001	0.065 ± 0.002	148.9 ± 0.7	-0.015	0.096	0.007	0.32	-0.24	-0.47	0.08	-0.12	-0.15	0.14
9.148 ± 0.013	19.755 ± 0.002	0.069 ± 0.002	147.2 ± 0.8	-0.010	0.094	0.009	0.37	-0.04	-0.50	0.09	0.02	-0.17	0.14
9.664 ± 0.013	19.843 ± 0.002	0.072 ± 0.002	146.1 ± 0.7	0.005	0.070	0.009	0.31	-0.02	-0.41	0.20	0.01	-0.06	0.17
10.171 ± 0.015	19.922 ± 0.002	0.073 ± 0.002	147.4 ± 0.8	-0.013	0.028	0.011	0.12	-0.27	-0.35	0.76	-0.13	0.06	0.12
10.574 ± 0.017	19.992 ± 0.003	0.065 ± 0.002	147.5 ± 1.0	-0.028	-0.011	0.012	0.21	-0.33	-0.22	0.94	-0.25	0.10	0.13
10.919 ± 0.017	20.060 ± 0.003	0.059 ± 0.002	144.7 ± 1.1	-0.014	0.001	0.012	0.33	-0.19	-0.59	0.76	-0.33	-0.22	0.11
11.256 ± 0.017	20.124 ± 0.004	0.057 ± 0.002	144.3 ± 1.1	-0.012	-0.002	0.012	0.41	-0.26	-0.22	0.53	-0.44	-0.15	0.13
11.574 ± 0.016	20.177 ± 0.005	0.061 ± 0.002	143.4 ± 0.9	-0.005	0.013	0.011	0.35	-0.18	-0.21	0.43	-0.38	-0.18	0.16
11.842 ± 0.018	20.223 ± 0.006	0.058 ± 0.002	143.6 ± 1.1	-0.027	0.020	0.013	0.26	-0.07	-0.17	0.40	-0.46	-0.11	0.17
12.069 ± 0.022	20.260 ± 0.007	0.059 ± 0.003	143.2 ± 1.3	-0.026	0.015	0.016	0.17
12.268 ± 0.027	20.291 ± 0.008	0.061 ± 0.003	140.8 ± 1.4	-0.033	0.012	0.019	0.17
12.467 ± 0.028	20.324 ± 0.010	0.062 ± 0.003	142.2 ± 1.5	-0.034	0.016	0.020	0.17
12.578 ± 0.032	20.351 ± 0.013	0.057 ± 0.003	143.7 ± 1.8	-0.023	-0.000	0.023	0.17
12.658 ± 0.042	20.363 ± 0.023	0.054 ± 0.004	143.6 ± 2.4	-0.013	0.010	0.029	0.17
12.680 ± 0.049	20.382 ± 0.023	0.053 ± 0.005	145.3 ± 2.9	-0.013	0.004	0.035	0.17
13.220 ± 0.040	20.544 ± 0.007	0.053 ± 0.004	130.7 ± 2.3	-0.051	0.004	0.028	-0.45	-0.29	-1.09	0.04	-0.25	-0.33	0.27
13.699 ± 0.043	20.648 ± 0.008	0.045 ± 0.004	127.5 ± 2.8	-0.064	-0.021	0.030	-0.61	-0.17	-0.98	-0.25	-0.22	-0.23	0.29
14.210 ± 0.047	20.739 ± 0.008	0.040 ± 0.005	127.0 ± 3.4	-0.127	-0.002	0.034	-0.52	-0.09	-1.45	-0.47	0.04	-0.26	0.36
14.874 ± 0.054	20.839 ± 0.008	0.047 ± 0.005	133.6 ± 3.2	-0.076	0.055	0.038	-0.91	0.20	-1.78	0.39	0.55	-0.29	0.28
15.553 ± 0.063	20.934 ± 0.009	0.043 ± 0.005	127.7 ± 3.8	-0.083	0.011	0.044	-0.57	-0.24	-1.20	-0.25	0.74	-0.45	0.35
16.148 ± 0.061	21.038 ± 0.010	0.048 ± 0.005	125.1 ± 3.2	-0.019	-0.053	0.043	-0.01	-0.01	-0.92	-0.28	0.77	-0.85	0.35
16.763 ± 0.078	21.146 ± 0.011	0.049 ± 0.006	119.2 ± 3.9	-0.019	-0.155	0.055	0.15	0.28	-1.80	-0.50	1.19	-0.53	0.45
17.413 ± 0.090	21.222 ± 0.011	0.053 ± 0.007	122.5 ± 3.9	-0.006	-0.167	0.063	-0.38	1.08	-1.03	-0.37	1.58	-0.86	0.47
18.086 ± 0.098	21.303 ± 0.010	0.059 ± 0.007	113.6 ± 3.7	-0.095	-0.218	0.069	-0.36	-0.17	-1.25	-1.19	0.59	0.05	0.50
19.124 ± 0.118	21.413 ± 0.010	0.065 ± 0.008	112.5 ± 3.8	-0.165	-0.269	0.083	-0.26	-0.11	-1.24	-1.56	0.68	-0.43	0.84
20.093 ± 0.125	21.519 ± 0.011	0.078 ± 0.008	107.8 ± 3.2	-0.127	-0.377	0.088	0.07	0.34	-1.16	-2.35	0.19	-0.00	0.58
20.719 ± 0.130	21.586 ± 0.013	0.063 ± 0.008	108.4 ± 4.0	-0.089	-0.333	0.092	-0.28	0.13	-0.61	-2.87	-0.20	0.70	0.52
21.347 ± 0.140	21.666 ± 0.014	0.057 ± 0.009	111.5 ± 4.7	-0.083	-0.326	0.099	0.57	0.32	-1.52	-2.06	0.87	-0.32	0.61
22.317 ± 0.168	21.778 ± 0.013	0.062 ± 0.010	98.5 ± 4.9	0.089	-0.320	0.119	0.12	0.52	0.69	-3.20	-0.07	-0.03	0.95
23.038 ± 0.172	21.873 ± 0.015	0.055 ± 0.010	104.3 ± 5.5	0.216	-0.225	0.121	0.15	0.88	-0.31	-2.10	-0.39	0.14	0.89
23.737 ± 0.170	21.940 ± 0.015	0.062 ± 0.010	101.5 ± 4.7	0.522	-0.193	0.120	0.45	1.82	-0.11	-1.42	0.64	-0.60	0.88
24.939 ± 0.206	21.975 ± 0.016	0.087 ± 0.011	103.8 ± 3.9	0.293	-0.231	0.146	0.27	0.37	-0.26	-3.58	0.96	0.01	0.91
25.748 ± 0.209	22.045 ± 0.016	0.094 ± 0.010	93.6 ± 3.5	0.121	-0.218	0.147	-0.47	0.85	-0.78	-3.52	-0.51	-0.84	0.74
26.870 ± 0.231	22.142 ± 0.017	0.101 ± 0.011	269.7 ± 3.5	-0.483	0.023	0.163	-0.65	1.59	3.44	-2.24	0.25	-0.11	0.98
27.214 ± 0.257	22.207 ± 0.017	0.080 ± 0.012	96.2 ± 4.8	-0.267	0.163	0.182	1.13	0.78	1.44	-3.70	1.29	0.35	1.03

NGC 687

0.015 ± 0.000	14.226 ± 0.010	0.000 ± 0.000	198.4 ± 0.0	-0.141	0.132	0.000	0.00	0.00	0.00	0.00	0.00	0.00	0.00
0.041 ± 0.326	14.419 ± 0.017	0.283 ± 7.970	166.1 ± 26.1	0.000	0.000	0.230	3.72	-1.79	8.24	-4.13	-1.04	0.65	2.83
0.068 ± 0.002	14.513 ± 0.015	0.060 ± 0.034	124.4 ± 17.3	0.002	0.022	0.001	2.20	-2.97	-2.39	2.19	-0.03	1.13	0.29
0.097 ± 0.002	14.634 ± 0.010	0.035 ± 0.031	244.0 ± 26.7	0.002	0.027	0.002	-3.69	3.96	2.64	1.49	0.08	-0.41	0.43
0.147 ± 0.008	14.731 ± 0.014	0.232 ± 0.057	239.0 ± 9.1	-0.008	0.035	0.005	-10.80	2.83	8.22	-0.12	5.41	-1.24	1.81
0.173 ± 0.006	14.797 ± 0.033	0.193 ± 0.038	241.5 ± 7.0	-0.009	0.034	0.004	-9.11	2.33	6.68	-1.84	2.99	-1.10	0.59
0.192 ± 0.004	14.899 ± 0.032	0.094 ± 0.027	244.6 ± 9.0	-0.008	0.032	0.003	-5.81	1.90	4.51	-2.92	1.27	-1.15	0.58
0.216 ± 0.003	15.028 ± 0.009	0.031 ± 0.017	250.2 ± 16.0	-0.005	0.030	0.002	-2.39	1.57	2.49	-1.77	0.67	-1.52	0.77
0.246 ± 0.003	15.129 ± 0.009	0.028 ± 0.014	143.4 ± 14.8	-0.002	0.031	0.002	0.20	0.59	-0.29	2.13	-1.84	-1.19	0.91
0.280 ± 0.002	15.236 ± 0.008	0.043 ± 0.008	137.7 ± 5.6	-0.001	0.028	0.001	-0.04	0.97	-0.96	0.94	-0.78	-0.90	0.52
0.315 ± 0.001	15.331 ± 0.005	0.051 ± 0.006	132.5 ± 3.7	0.001	0.027	0.001	0.10	1.06	-0.76	0.13	-0.19	-0.09	0.41
0.357 ± 0.001	15.422 ± 0.005	0.072 ± 0.004	119.5 ± 1.8	0.000	0.028	0.001	-0.14	0.39	0.22	-0.32	-0.41	0.07	0.34
0.401 ± 0.001	15.523 ± 0.004	0.080 ± 0.004	115.2 ± 1.5	0.000	0.028	0.001	0.66	-0.18	0.01	-0.24	-0.82	-0.08	0.27
0.447 ± 0.001	15.626 ± 0.004	0.091 ± 0.004	114.0 ± 1.2	0.002	0.028	0.001	0.61	-0.46	0.55	0.07	-0.11	-0.05	0.33

TABLE 5—Continued

a [arcsec]	μ_R [mag arcsec $^{-2}$]	e	PA [°]	Δx_c [arcsec]	Δy_c [arcsec]	Err. ^a [arcsec]	a_3/a × 100	b_3/a × 100	a_4/a × 100	b_4/a × 100	a_6/a × 100	b_6/a × 100	Err. ^b
0.489 ± 0.001	15.729 ± 0.004	0.080 ± 0.004	119.2 ± 1.4	0.004	0.028	0.001	0.03	-0.20	0.48	-0.09	0.03	0.21	0.33
0.542 ± 0.002	15.825 ± 0.004	0.091 ± 0.004	122.3 ± 1.4	0.001	0.026	0.001	-0.16	-0.04	0.06	0.03	-0.41	0.86	0.42
0.600 ± 0.002	15.922 ± 0.004	0.110 ± 0.004	123.5 ± 1.0	0.003	0.027	0.001	0.05	-0.10	-0.33	0.31	0.02	0.35	0.30
0.654 ± 0.002	16.025 ± 0.003	0.114 ± 0.003	124.6 ± 0.9	0.006	0.029	0.001	0.36	-0.22	0.18	0.51	0.24	0.13	0.31
0.712 ± 0.002	16.120 ± 0.003	0.119 ± 0.003	125.5 ± 0.9	0.004	0.031	0.001	-0.21	-0.19	0.02	0.22	-0.08	-0.05	0.34
0.777 ± 0.002	16.220 ± 0.003	0.122 ± 0.002	124.9 ± 0.7	0.010	0.033	0.001	-0.05	0.01	-0.06	-0.22	0.12	-0.25	0.26
0.841 ± 0.003	16.320 ± 0.003	0.125 ± 0.004	123.4 ± 1.0	0.007	0.031	0.002	0.02	-0.19	0.35	0.57	0.48	-0.46	0.29
0.924 ± 0.002	16.417 ± 0.003	0.140 ± 0.003	122.9 ± 0.7	0.006	0.032	0.001	0.28	0.08	0.26	0.39	0.26	-0.27	0.26
1.001 ± 0.002	16.519 ± 0.003	0.140 ± 0.003	124.5 ± 0.7	0.008	0.030	0.002	-0.02	-0.18	-0.05	0.56	0.48	0.29	0.24
1.090 ± 0.003	16.612 ± 0.004	0.145 ± 0.003	124.0 ± 0.8	0.007	0.017	0.002	0.10	0.10	-0.11	-0.14	0.20	-0.24	0.25
1.185 ± 0.003	16.709 ± 0.003	0.149 ± 0.003	122.4 ± 0.8	0.010	0.027	0.002	0.18	0.64	0.20	0.54	-0.34	0.18	0.34
1.283 ± 0.004	16.811 ± 0.002	0.148 ± 0.004	123.6 ± 0.9	0.013	0.034	0.003	0.03	0.33	-0.59	-0.03	-0.40	-0.49	0.28
1.398 ± 0.004	16.907 ± 0.002	0.162 ± 0.003	124.8 ± 0.7	0.010	0.029	0.003	0.07	-0.01	-0.44	-0.25	-0.09	0.05	0.34
1.517 ± 0.005	17.004 ± 0.002	0.155 ± 0.004	126.1 ± 0.8	0.003	0.041	0.003	0.26	-0.83	-0.28	-0.03	0.05	0.04	0.32
1.647 ± 0.006	17.099 ± 0.002	0.166 ± 0.004	124.0 ± 0.8	0.005	0.035	0.004	0.63	-0.49	-0.01	-0.16	-0.46	-0.44	0.30
1.772 ± 0.005	17.198 ± 0.002	0.158 ± 0.003	123.4 ± 0.8	0.003	0.024	0.004	0.18	0.08	-0.14	0.76	0.21	0.24	0.29
1.897 ± 0.006	17.296 ± 0.002	0.155 ± 0.004	122.7 ± 0.8	0.013	0.035	0.004	0.58	0.04	-0.36	-0.25	0.66	-0.01	0.38
2.034 ± 0.006	17.392 ± 0.003	0.151 ± 0.004	124.3 ± 0.8	0.013	0.031	0.004	-0.08	0.02	-0.56	-0.20	0.13	-0.70	0.27
2.182 ± 0.003	17.492 ± 0.003	0.143 ± 0.002	124.1 ± 0.4	0.005	0.032	0.002	-0.19	0.30	-0.31	0.00	0.12	-0.19	0.13
2.320 ± 0.004	17.593 ± 0.002	0.142 ± 0.002	123.1 ± 0.5	0.007	0.024	0.003	0.41	0.03	-0.25	0.50	-0.19	-0.14	0.16
2.462 ± 0.003	17.693 ± 0.002	0.138 ± 0.002	124.4 ± 0.4	0.003	0.026	0.002	0.16
2.609 ± 0.004	17.791 ± 0.002	0.133 ± 0.002	124.3 ± 0.5	0.003	0.033	0.003	0.12	-0.24	0.00	0.08	0.30	-0.10	0.14
2.782 ± 0.005	17.887 ± 0.002	0.136 ± 0.002	124.7 ± 0.5	0.007	0.038	0.004	-0.00	-0.26	-0.26	0.10	0.38	-0.26	0.17
2.973 ± 0.006	17.980 ± 0.002	0.140 ± 0.003	123.0 ± 0.6	0.015	0.041	0.005	0.17
3.177 ± 0.006	18.077 ± 0.002	0.141 ± 0.002	122.1 ± 0.6	0.007	0.041	0.004	-0.03	-0.04	-0.25	-0.05	0.02	-0.09	0.20
3.380 ± 0.006	18.176 ± 0.002	0.139 ± 0.002	120.5 ± 0.5	0.001	0.044	0.004	0.20
3.616 ± 0.007	18.263 ± 0.003	0.145 ± 0.002	121.0 ± 0.6	0.007	0.053	0.005	0.07	0.04	-0.56	0.10	0.06	-0.04	0.17
3.877 ± 0.014	18.359 ± 0.003	0.157 ± 0.004	122.4 ± 0.9	-0.002	0.038	0.010	-0.21	-0.08	-1.06	-0.14	0.25	0.15	0.38
4.143 ± 0.011	18.456 ± 0.002	0.154 ± 0.003	121.2 ± 0.7	0.005	0.039	0.008	0.38
4.435 ± 0.015	18.549 ± 0.002	0.161 ± 0.004	121.5 ± 0.8	0.026	0.045	0.010	0.38
4.725 ± 0.017	18.640 ± 0.002	0.152 ± 0.004	120.9 ± 0.9	0.032	0.057	0.012	0.38
5.033 ± 0.010	18.733 ± 0.002	0.149 ± 0.002	121.1 ± 0.5	0.013	0.038	0.007	0.38
5.388 ± 0.013	18.823 ± 0.002	0.152 ± 0.003	120.4 ± 0.7	0.017	0.044	0.009	0.13	0.18	0.34	-0.14	0.06	-0.08	0.21
5.752 ± 0.017	18.910 ± 0.002	0.155 ± 0.004	120.3 ± 0.8	0.012	0.048	0.012	0.21
6.112 ± 0.016	18.999 ± 0.003	0.157 ± 0.003	122.2 ± 0.7	-0.012	0.031	0.012	0.14	0.04	-0.56	0.42	0.07	-0.52	0.30
6.444 ± 0.020	19.088 ± 0.003	0.153 ± 0.004	120.4 ± 0.8	-0.029	0.012	0.014	0.18	0.20	-0.40	0.02	0.88	-0.21	0.30
6.805 ± 0.017	19.170 ± 0.003	0.152 ± 0.003	119.2 ± 0.7	-0.032	0.029	0.012	-0.30	-0.24	-0.35	-0.57	0.23	-0.17	0.27
7.099 ± 0.031	19.248 ± 0.003	0.137 ± 0.005	119.8 ± 1.3	-0.073	0.013	0.022	0.27
7.481 ± 0.031	19.332 ± 0.003	0.136 ± 0.005	121.4 ± 1.2	-0.055	0.031	0.022	0.27
7.863 ± 0.024	19.422 ± 0.003	0.131 ± 0.004	119.0 ± 1.0	-0.032	0.016	0.017	0.27
8.187 ± 0.030	19.512 ± 0.002	0.128 ± 0.004	119.0 ± 1.1	-0.013	0.019	0.021	-0.05	0.25	-0.72	0.10	0.51	-0.24	0.34
8.521 ± 0.021	19.593 ± 0.003	0.121 ± 0.003	119.2 ± 0.8	-0.018	0.045	0.015	0.34
8.872 ± 0.026	19.667 ± 0.004	0.120 ± 0.004	119.8 ± 1.0	-0.018	0.051	0.018	0.34
9.253 ± 0.027	19.742 ± 0.005	0.124 ± 0.004	117.7 ± 1.0	-0.054	0.055	0.019	0.34
9.517 ± 0.036	19.807 ± 0.009	0.110 ± 0.005	118.5 ± 1.4	-0.043	0.069	0.025	0.34
9.896 ± 0.036	19.876 ± 0.013	0.117 ± 0.005	118.9 ± 1.3	-0.024	0.093	0.026	0.34
10.303 ± 0.031	19.946 ± 0.013	0.121 ± 0.004	120.0 ± 1.0	0.001	0.055	0.022	0.34
10.701 ± 0.041	20.016 ± 0.011	0.123 ± 0.005	121.0 ± 1.3	0.011	0.079	0.029	0.34
11.041 ± 0.040	20.084 ± 0.009	0.119 ± 0.004	121.0 ± 1.2	0.026	0.031	0.028	0.34
11.408 ± 0.036	20.152 ± 0.009	0.123 ± 0.004	119.8 ± 1.0	-0.026	0.017	0.025	0.34
11.803 ± 0.046	20.224 ± 0.009	0.125 ± 0.005	119.9 ± 1.3	0.003	0.005	0.033	0.34
12.124 ± 0.053	20.256 ± 0.041	0.124 ± 0.005	121.9 ± 1.4	0.036	-0.031	0.037	-0.14	-0.28	-0.14	-0.29	0.03	1.17	0.39
12.354 ± 0.045	20.323 ± 0.040	0.107 ± 0.005	121.4 ± 1.4	0.031	-0.045	0.032	0.39
12.604 ± 0.050	20.402 ± 0.007	0.107 ± 0.005	118.2 ± 1.5	0.018	-0.038	0.035	0.39
12.951 ± 0.139	20.426 ± 0.015	0.121 ± 0.013	116.6 ± 3.6	-0.001	-0.065	0.099	0.39
13.379 ± 0.098	20.458 ± 0.020	0.124 ± 0.009	118.7 ± 2.4	0.016	-0.074	0.069	0.39
13.720 ± 0.074	20.530 ± 0.019	0.107 ± 0.007	120.1 ± 2.0	-0.037	-0.044	0.052	0.39
14.021 ± 0.058	20.611 ± 0.019	0.105 ± 0.005	119.6 ± 1.6	-0.013	-0.036	0.041	0.39
14.258 ± 0.067	20.603 ± 0.036	0.105 ± 0.006	119.5 ± 1.8	0.018	-0.068	0.048	0.39
14.417 ± 0.067	20.604 ± 0.043	0.103 ± 0.006	117.0 ± 1.8	0.086	-0.050	0.047	0.39
14.594 ± 0.097	20.672 ± 0.043	0.106 ± 0.008	118.1 ± 2.5	0.073	-0.043	0.069	0.39
14.827 ± 0.067	20.700 ± 0.007	0.121 ± 0.006	111.9 ± 1.5	0.051	-0.028	0.047	0.61	-0.78	0.71	-0.74	-0.63	-0.69	0.48
15.674 ± 0.076	20.851 ± 0.008	0.104 ± 0.006	110.3 ± 1.9	0.000	-0.003	0.054	0.91	-1.13	0.44	0.07	-0.65	-0.82	0.53
16.903 ± 0.083	20.994 ± 0.008	0.121 ± 0.006	107.4 ± 1.6	-0.013	-0.105	0.059	1.71	-0.20	-0.21	0.31	-0.24	-0.89	0.54

TABLE 5—Continued

<i>a</i> [arcsec]	μ_R [mag arcsec $^{-2}$]	<i>e</i>	PA [°]	Δx_c [arcsec]	Δy_c [arcsec]	Err. ^a [arcsec]	a_3/a × 100	b_3/a × 100	a_4/a × 100	b_4/a × 100	a_6/a × 100	b_6/a × 100	Err. ^b
18.147 ± 0.113	21.121 ± 0.009	0.128 ± 0.008	106.7 ± 2.0	0.108	0.156	0.080	1.52	-1.37	0.29	0.45	-0.38	-1.12	0.80
19.382 ± 0.137	21.250 ± 0.009	0.133 ± 0.009	104.4 ± 2.1	0.045	0.182	0.097	1.21	-0.88	-0.44	-0.08	0.05	-0.70	0.86
20.585 ± 0.136	21.378 ± 0.009	0.105 ± 0.008	101.6 ± 2.5	0.127	0.099	0.096	0.54	0.18	0.75	-0.80	-0.23	-0.51	0.79
22.010 ± 0.163	21.497 ± 0.010	0.094 ± 0.010	113.0 ± 3.2	0.006	0.023	0.116	0.54	0.19	-1.18	-0.92	0.39	-0.88	0.89
23.227 ± 0.179	21.610 ± 0.012	0.093 ± 0.010	112.0 ± 3.3	0.178	0.169	0.127	1.29	-0.88	-1.38	-0.86	0.98	-0.50	0.87
24.260 ± 0.217	21.760 ± 0.017	0.063 ± 0.012	109.5 ± 5.2	0.051	-0.066	0.154	0.63	-0.15	0.30	-0.83	-0.60	-1.16	1.19
25.663 ± 0.213	21.865 ± 0.017	0.102 ± 0.011	111.0 ± 3.3	-0.089	0.086	0.151	0.93	-0.13	0.17	-0.56	-0.66	-0.68	0.82
26.780 ± 0.211	21.947 ± 0.015	0.099 ± 0.010	107.3 ± 3.2	-0.254	0.061	0.149	0.42	0.99	-0.10	0.09	-1.54	-0.04	0.97
28.028 ± 0.247	22.114 ± 0.015	0.110 ± 0.011	102.8 ± 3.2	0.025	0.099	0.175	-0.04	0.38	0.07	-1.21	1.02	-2.32	0.84
29.804 ± 1.227	22.314 ± 0.017	0.077 ± 0.054	97.3 ± 21.6	-0.045	-0.035	0.868	0.84
31.128 ± 0.287	22.480 ± 0.024	0.074 ± 0.012	94.8 ± 5.1	0.223	0.163	0.203	0.84
32.157 ± 0.380	22.548 ± 0.029	0.082 ± 0.015	100.2 ± 5.8	0.286	-0.022	0.269	0.84
32.869 ± 0.566	22.673 ± 0.044	0.083 ± 0.022	108.8 ± 8.4	0.312	0.194	0.400	0.84
NGC 703													
0.212 ± 0.000	16.938 ± 0.010	0.000 ± 0.000	0.0 ± 0.0	0.076	0.025	0.000	0.00	0.00	0.00	0.00	0.00	0.00	0.00
0.272 ± 0.057	17.013 ± 0.010	0.184 ± 0.242	56.9 ± 46.1	0.000	0.000	0.040	4.37	3.34	-2.21	1.42	0.30	-0.43	1.04
0.701 ± 0.036	17.187 ± 0.013	0.213 ± 0.057	41.1 ± 9.7	-0.057	-0.032	0.025	-0.52	3.53	-1.24	-1.58	1.31	-0.48	0.86
0.984 ± 0.009	17.408 ± 0.011	0.164 ± 0.011	46.4 ± 2.3	-0.051	-0.019	0.007	0.25	-0.79	-0.41	-0.02	0.43	-0.48	0.44
1.230 ± 0.013	17.603 ± 0.015	0.163 ± 0.013	50.0 ± 2.7	-0.038	0.000	0.009	-0.38	-2.33	0.50	0.15	0.10	-0.06	0.42
1.471 ± 0.020	17.721 ± 0.018	0.187 ± 0.016	51.4 ± 3.0	-0.025	0.019	0.014	-0.88	-3.29	1.74	-0.20	0.17	-0.02	0.36
1.720 ± 0.024	17.875 ± 0.023	0.191 ± 0.016	52.2 ± 3.0	-0.025	0.019	0.017	-1.26	-3.87	1.46	-0.63	-0.02	-0.10	0.30
1.918 ± 0.026	18.103 ± 0.026	0.149 ± 0.016	51.8 ± 3.6	-0.032	0.006	0.018	-0.81	-4.06	1.88	-0.42	0.21	-0.37	0.19
2.167 ± 0.035	18.288 ± 0.022	0.166 ± 0.019	50.6 ± 4.1	-0.025	0.006	0.025	-0.40	-5.19	3.04	-0.25	0.44	-0.52	0.23
2.427 ± 0.043	18.424 ± 0.023	0.132 ± 0.022	49.2 ± 5.4	-0.057	-0.038	0.030	0.55	-6.82	1.84	0.39	0.62	-0.38	0.23
2.738 ± 0.043	18.574 ± 0.021	0.111 ± 0.020	43.3 ± 5.7	-0.089	-0.089	0.030	3.15	-5.85	0.77	0.26	0.39	0.52	0.20
3.139 ± 0.044	18.728 ± 0.014	0.122 ± 0.018	38.8 ± 4.7	-0.121	-0.172	0.031	4.57	-4.36	0.19	-0.87	0.30	1.09	0.19
3.589 ± 0.038	18.905 ± 0.013	0.142 ± 0.013	37.6 ± 3.0	-0.165	-0.235	0.027	3.50	-2.38	0.12	-2.05	0.33	0.50	0.21
4.174 ± 0.033	19.092 ± 0.009	0.189 ± 0.009	40.5 ± 1.7	-0.204	-0.267	0.023	1.98	-1.92	-0.64	-2.38	0.12	-0.55	0.18
4.823 ± 0.027	19.274 ± 0.008	0.246 ± 0.006	43.4 ± 1.0	-0.223	-0.280	0.019	0.73	-1.44	-0.86	-1.87	0.24	-0.66	0.25
5.524 ± 0.020	19.427 ± 0.009	0.281 ± 0.004	45.2 ± 0.5	-0.210	-0.343	0.014	-0.37	-1.15	-0.02	-1.03	0.35	-0.50	0.30
6.143 ± 0.022	19.591 ± 0.009	0.292 ± 0.004	47.0 ± 0.5	-0.191	-0.363	0.016	-0.81	-0.83	-0.24	-0.81	0.16	-0.72	0.33
6.815 ± 0.022	19.764 ± 0.008	0.307 ± 0.003	47.5 ± 0.4	-0.197	-0.350	0.015	-0.56	-0.46	-0.12	-0.55	0.08	-0.69	0.31
7.501 ± 0.021	19.938 ± 0.008	0.320 ± 0.003	48.3 ± 0.4	-0.197	-0.337	0.015	-0.09	-0.31	-0.01	0.28	-0.31	-0.12	0.32
8.196 ± 0.020	20.114 ± 0.008	0.329 ± 0.002	48.2 ± 0.3	-0.216	-0.401	0.014	0.07	0.37	0.24	0.38	-0.13	-0.50	0.28
9.037 ± 0.025	20.281 ± 0.007	0.344 ± 0.003	47.3 ± 0.3	-0.254	-0.350	0.018	0.16	0.42	0.25	-0.08	-0.16	-0.14	0.35
9.811 ± 0.029	20.449 ± 0.008	0.345 ± 0.003	47.6 ± 0.4	-0.261	-0.331	0.021	-0.44	0.12	-0.53	-0.38	-0.14	0.26	0.38
10.671 ± 0.036	20.617 ± 0.009	0.355 ± 0.003	48.5 ± 0.4	-0.280	-0.293	0.025	0.29	-0.16	-0.89	-0.30	-0.26	-0.16	0.39
11.663 ± 0.041	20.781 ± 0.009	0.355 ± 0.003	48.4 ± 0.4	-0.223	-0.375	0.029	0.06	0.04	-0.51	0.28	-0.16	-0.02	0.40
12.447 ± 0.049	20.953 ± 0.011	0.348 ± 0.004	47.4 ± 0.5	-0.178	-0.407	0.035	0.42	-0.21	-0.84	0.04	-0.10	-0.19	0.48
13.450 ± 0.064	21.118 ± 0.012	0.359 ± 0.004	48.1 ± 0.5	-0.210	-0.350	0.045	-0.63	-1.30	-1.03	0.08	0.07	0.21	0.57
14.299 ± 0.080	21.280 ± 0.013	0.357 ± 0.005	48.3 ± 0.6	-0.337	-0.178	0.057	-0.91	-1.06	-1.01	0.50	-1.18	0.97	0.56
15.334 ± 0.096	21.441 ± 0.014	0.353 ± 0.006	49.0 ± 0.7	-0.254	-0.114	0.068	-0.50	-1.04	-1.27	0.86	-0.60	0.79	0.53
16.468 ± 0.134	21.595 ± 0.014	0.352 ± 0.008	48.5 ± 0.9	-0.153	-0.153	0.095	-0.23	-0.32	-2.05	0.78	-1.00	0.31	0.74
17.545 ± 0.133	21.750 ± 0.016	0.357 ± 0.007	48.6 ± 0.9	-0.045	-0.248	0.094	-0.06	-0.38	-1.09	0.50	0.41	0.05	0.73
18.840 ± 0.135	21.877 ± 0.020	0.371 ± 0.006	48.2 ± 0.8	-0.216	-0.127	0.096	0.26	0.07	-0.00	-0.77	-0.29	-1.59	0.84
19.715 ± 0.130	22.022 ± 0.021	0.370 ± 0.006	47.0 ± 0.7	-0.184	-0.235	0.092	0.48	0.95	0.17	-0.35	-0.09	-0.76	0.67
21.024 ± 0.155	22.190 ± 0.022	0.373 ± 0.007	48.2 ± 0.8	-0.331	-0.006	0.109	0.42	0.32	0.28	-0.06	0.74	-1.20	0.86
21.703 ± 0.182	22.322 ± 0.025	0.358 ± 0.008	49.1 ± 1.0	-0.566	0.197	0.129	-0.38	-0.71	-0.63	-1.26	0.88	-2.52	0.66
22.421 ± 0.244	22.445 ± 0.027	0.346 ± 0.010	49.1 ± 1.3	-0.541	0.159	0.173	-1.84	-0.30	-0.95	-1.89	0.56	-2.36	0.83
23.251 ± 0.279	22.567 ± 0.029	0.338 ± 0.011	48.3 ± 1.4	-0.108	-0.038	0.198	-0.42	0.49	0.11	-2.10	1.42	-1.67	1.18
24.075 ± 0.314	22.701 ± 0.040	0.327 ± 0.012	49.7 ± 1.6	-0.032	0.089	0.222	0.64	1.99	0.57	-2.20	-0.73	-1.26	1.17
24.759 ± 0.336	22.788 ± 0.046	0.332 ± 0.013	49.5 ± 1.7	-0.191	0.134	0.238	0.17	2.92	-0.75	-3.41	-0.42	-2.81	1.10
25.779 ± 0.375	22.824 ± 0.061	0.343 ± 0.014	48.6 ± 1.7	-0.191	0.191	0.265	-1.01	2.29	0.23	-3.92	-0.29	-3.46	1.25
26.132 ± 0.383	23.040 ± 0.062	0.349 ± 0.014	48.9 ± 1.7	-0.216	-0.019	0.271	-1.90	2.19	-0.85	-4.95	0.04	-2.85	1.15
27.680 ± 0.380	23.411 ± 0.062	0.354 ± 0.013	44.1 ± 1.6	0.070	-0.337	0.269	-1.73	3.97	-1.58	-5.02	-1.09	-2.60	1.14
NGC 708													
0.202 ± 0.000	18.222 ± 0.010	0.000 ± 0.000	90.0 ± 0.0	-0.145	-0.261	0.000	0.00	0.00	0.00	0.00	0.00	0.00	0.00
1.568 ± 0.072	18.351 ± 0.007	0.323 ± 0.044	78.1 ± 5.8	-0.000	0.000	0.051	-0.05	-0.84	-0.46	1.19	1.31	-0.77	0.87
2.855 ± 0.036	18.495 ± 0.006	0.187 ± 0.015	90.8 ± 2.7	-0.230	0.012	0.025	-0.74	-0.34	-0.10	0.22	-0.54	-0.33	0.43
3.275 ± 0.026	18.620 ± 0.006	0.145 ± 0.010	94.0 ± 2.2	-0.206	0.042	0.018	-0.26	-0.08	0.24	0.26	-0.26	0.17	0.30

TABLE 5—Continued

a [arcsec]	μ_R [mag arcsec $^{-2}$]	e	PA [°]	Δx_c [arcsec]	Δy_c [arcsec]	Err. ^a [arcsec]	a_3/a $\times 100$	b_3/a $\times 100$	a_4/a $\times 100$	b_4/a $\times 100$	a_6/a $\times 100$	b_6/a $\times 100$	Err. ^b
3.646 ± 0.022	18.722 ± 0.007	0.116 ± 0.008	98.8 ± 2.1	-0.212	0.055	0.015	0.06	-0.16	0.61	-0.14	0.38	-0.14	0.35
4.048 ± 0.022	18.829 ± 0.006	0.107 ± 0.007	99.2 ± 2.0	-0.224	0.073	0.015	0.15	-0.07	0.45	-0.38	0.42	-0.21	0.33
4.427 ± 0.022	18.923 ± 0.006	0.094 ± 0.006	99.5 ± 2.1	-0.212	0.103	0.016	0.29	0.56	0.27	-0.36	0.45	0.00	0.30
4.782 ± 0.021	19.020 ± 0.006	0.082 ± 0.006	98.9 ± 2.1	-0.188	0.121	0.015	0.17	0.19	0.19	0.04	0.17	0.20	0.29
5.152 ± 0.020	19.129 ± 0.006	0.074 ± 0.005	101.1 ± 2.1	-0.158	0.133	0.014	-0.22	0.09	-0.03	0.56	-0.08	0.13	0.29
5.538 ± 0.022	19.225 ± 0.006	0.067 ± 0.005	97.0 ± 2.4	-0.115	0.133	0.016	-0.49	0.17	-0.65	0.36	-0.12	-0.02	0.27
5.993 ± 0.043	19.325 ± 0.005	0.074 ± 0.010	95.1 ± 4.0	-0.061	0.164	0.031	-1.36	0.61	0.51	-0.26	0.66	0.19	0.71
6.361 ± 0.042	19.429 ± 0.008	0.059 ± 0.009	90.7 ± 4.5	-0.073	0.176	0.030	-1.40	-0.15	1.12	0.38	0.51	0.83	0.64
6.744 ± 0.036	19.514 ± 0.015	0.046 ± 0.007	86.2 ± 4.7	-0.127	0.164	0.026	-0.66	-0.89	-0.22	-1.12	0.32	-1.03	0.55
7.227 ± 0.026	19.609 ± 0.014	0.050 ± 0.005	80.7 ± 2.9	-0.109	0.170	0.019	0.10	-0.54	0.31	0.25	0.66	-0.36	0.35
7.676 ± 0.024	19.724 ± 0.005	0.043 ± 0.004	72.8 ± 2.6	-0.097	0.170	0.017	0.17	-0.10	-0.74	0.07	0.11	0.37	0.32
8.179 ± 0.026	19.838 ± 0.005	0.049 ± 0.004	59.6 ± 2.7	-0.085	0.182	0.019	0.06	-0.05	0.42	-0.02	0.11	0.04	0.37
8.764 ± 0.028	19.922 ± 0.005	0.058 ± 0.004	51.3 ± 2.2	-0.109	0.255	0.020	0.30	0.02	-0.25	-0.11	-0.13	-0.39	0.35
9.326 ± 0.029	20.016 ± 0.005	0.059 ± 0.004	50.8 ± 2.1	-0.085	0.273	0.020	0.75	0.16	-0.01	-0.41	0.63	-0.08	0.40
9.901 ± 0.033	20.124 ± 0.006	0.070 ± 0.004	48.2 ± 1.9	-0.061	0.315	0.023	0.37	0.24	0.45	-0.46	0.25	0.16	0.38
10.540 ± 0.046	20.219 ± 0.006	0.079 ± 0.006	51.2 ± 2.2	-0.067	0.303	0.032	0.81	-0.02	0.19	-0.11	-0.03	-0.11	0.43
11.233 ± 0.047	20.315 ± 0.006	0.085 ± 0.005	48.6 ± 2.0	0.018	0.285	0.033	-0.31	0.51	-0.29	0.53	-0.34	0.42	0.39
12.153 ± 0.052	20.416 ± 0.006	0.119 ± 0.005	46.3 ± 1.5	0.036	0.327	0.037	-0.33	0.08	0.33	-0.21	0.05	-0.55	0.42
12.825 ± 0.060	20.514 ± 0.006	0.108 ± 0.006	43.1 ± 1.7	0.055	0.285	0.042	-0.22	0.32	0.22	-0.19	-0.29	-0.57	0.45
13.862 ± 0.065	20.611 ± 0.006	0.137 ± 0.006	41.5 ± 1.4	0.103	0.158	0.046	0.11	-0.28	-0.58	-0.73	-0.19	-0.16	0.45
14.671 ± 0.064	20.714 ± 0.006	0.128 ± 0.005	40.9 ± 1.4	0.042	0.255	0.045	0.19	0.56	-0.42	-0.81	0.06	0.00	0.35
15.732 ± 0.075	20.814 ± 0.006	0.153 ± 0.006	45.3 ± 1.3	0.085	0.121	0.053	1.07	0.53	0.14	0.25	-0.20	0.48	0.49
16.819 ± 0.098	20.916 ± 0.006	0.152 ± 0.007	38.7 ± 1.6	0.139	0.297	0.069	0.66	-0.01	0.37	0.28	0.05	-0.11	0.57
17.808 ± 0.111	21.013 ± 0.007	0.151 ± 0.008	37.6 ± 1.7	0.188	0.273	0.078	-0.38	-0.27	-0.08	0.44	-0.11	-0.42	0.51
18.802 ± 0.105	21.102 ± 0.007	0.158 ± 0.007	36.4 ± 1.4	0.182	0.273	0.074	-0.15	-0.21	-0.38	0.47	0.63	-0.29	0.61
20.082 ± 0.133	21.199 ± 0.007	0.165 ± 0.008	32.0 ± 1.6	0.291	0.412	0.094	0.94	0.37	0.64	1.31	0.49	0.43	0.53
21.405 ± 0.133	21.290 ± 0.007	0.175 ± 0.007	32.1 ± 1.4	0.382	0.376	0.094	0.26	0.16	0.05	0.55	-0.43	0.48	0.53
22.640 ± 0.135	21.383 ± 0.007	0.186 ± 0.007	35.0 ± 1.3	0.564	0.224	0.095	0.57	-0.39	0.33	-0.20	-0.26	0.43	0.50
23.648 ± 0.151	21.471 ± 0.007	0.181 ± 0.007	39.8 ± 1.4	0.545	0.255	0.107	0.68	0.58	0.41	-0.31	0.02	-0.41	0.64
25.260 ± 0.210	21.541 ± 0.007	0.204 ± 0.009	41.1 ± 1.7	0.782	0.182	0.148	-0.25	0.05	-0.34	-0.62	1.13	0.59	0.70
26.649 ± 0.212	21.615 ± 0.007	0.210 ± 0.009	40.5 ± 1.5	0.636	0.073	0.150	-0.25	0.28	0.38	0.76	1.10	0.04	0.63
NGC 712													
0.212 ± 0.000	17.333 ± 0.010	0.000 ± 0.000	0.0 ± 0.0	-0.178	-0.273	0.000	0.00	0.00	0.00	0.00	0.00	0.00	0.00
0.605 ± 0.117	17.420 ± 0.015	0.242 ± 0.207	63.7 ± 32.3	0.000	0.000	0.083	3.99	2.42	2.82	3.93	2.82	0.17	1.56
1.030 ± 0.010	17.542 ± 0.015	0.112 ± 0.012	65.4 ± 3.5	-0.032	0.076	0.007	-0.58	0.85	0.58	1.03	0.69	0.12	0.28
1.374 ± 0.010	17.680 ± 0.009	0.108 ± 0.009	62.7 ± 2.7	-0.057	0.146	0.007	-1.30	0.75	0.17	0.11	-0.13	-0.31	0.35
1.685 ± 0.006	17.840 ± 0.015	0.107 ± 0.005	63.5 ± 1.4	-0.089	0.204	0.004	-0.87	0.45	0.01	-0.02	-0.04	-0.07	0.19
1.973 ± 0.004	17.976 ± 0.015	0.113 ± 0.003	66.2 ± 0.8	-0.121	0.261	0.003	-0.44	0.24	-0.13	-0.14	0.00	-0.16	0.14
2.273 ± 0.004	18.102 ± 0.010	0.120 ± 0.002	69.6 ± 0.6	-0.140	0.299	0.003	-0.28	0.21	-0.10	-0.36	0.09	0.06	0.11
2.584 ± 0.004	18.229 ± 0.010	0.136 ± 0.002	74.4 ± 0.4	-0.146	0.331	0.003	0.21	0.13	0.09	-0.32	-0.03	-0.21	0.11
2.925 ± 0.006	18.360 ± 0.008	0.151 ± 0.003	77.9 ± 0.6	-0.153	0.350	0.004	0.43	0.02	0.34	-0.61	-0.10	0.07	0.08
3.300 ± 0.009	18.488 ± 0.006	0.166 ± 0.003	81.2 ± 0.7	-0.146	0.356	0.006	0.87	-0.02	0.55	-0.63	-0.17	-0.15	0.09
3.779 ± 0.013	18.606 ± 0.007	0.202 ± 0.004	84.4 ± 0.7	-0.140	0.343	0.009	1.28	0.36	0.83	-0.46	0.09	-0.39	0.13
4.335 ± 0.013	18.735 ± 0.005	0.229 ± 0.003	85.6 ± 0.5	-0.146	0.324	0.009	1.25	0.54	0.72	-0.26	0.16	-0.30	0.09
4.912 ± 0.014	18.864 ± 0.005	0.243 ± 0.003	86.2 ± 0.5	-0.146	0.299	0.010	1.07	0.30	1.12	-0.47	0.11	-0.12	0.09
5.521 ± 0.014	18.996 ± 0.005	0.256 ± 0.003	86.7 ± 0.4	-0.140	0.280	0.010	0.99	-0.00	0.91	-0.39	0.11	0.03	0.11
6.177 ± 0.012	19.124 ± 0.004	0.269 ± 0.002	86.7 ± 0.3	-0.134	0.273	0.009	0.77	0.01	0.78	-0.29	0.20	0.07	0.09
6.845 ± 0.011	19.253 ± 0.004	0.276 ± 0.002	86.5 ± 0.2	-0.153	0.286	0.008	0.38	-0.15	0.77	-0.36	0.18	-0.16	0.09
7.520 ± 0.016	19.389 ± 0.004	0.277 ± 0.002	86.4 ± 0.3	-0.204	0.299	0.011	-0.03	-0.47	0.65	-0.65	0.06	-0.54	0.13
8.246 ± 0.023	19.520 ± 0.004	0.277 ± 0.003	86.6 ± 0.4	-0.223	0.299	0.016	-0.37	-0.80	0.54	-0.96	0.09	-0.76	0.18
9.217 ± 0.014	19.648 ± 0.003	0.299 ± 0.002	85.3 ± 0.2	-0.146	0.242	0.010	-0.05	0.05	0.52	-0.18	-0.14	-0.15	0.16
10.162 ± 0.014	19.774 ± 0.003	0.302 ± 0.001	85.1 ± 0.2	-0.114	0.165	0.010	0.17	0.36	0.50	-0.00	0.01	0.03	0.13
11.178 ± 0.014	19.904 ± 0.003	0.314 ± 0.001	85.2 ± 0.2	-0.114	0.102	0.010	0.09	0.18	0.28	-0.33	0.34	-0.16	0.12
12.197 ± 0.013	20.036 ± 0.003	0.326 ± 0.001	85.0 ± 0.1	-0.127	0.070	0.009	0.12	0.28	-0.07	-0.10	0.04	-0.06	0.12
13.183 ± 0.016	20.168 ± 0.003	0.334 ± 0.001	85.5 ± 0.1	-0.153	0.076	0.011	-0.01	0.31	-0.26	-0.16	0.27	-0.02	0.12
14.142 ± 0.015	20.298 ± 0.003	0.339 ± 0.001	85.5 ± 0.1	-0.127	0.108	0.011	0.17	0.14	-0.43	-0.15	0.03	-0.16	0.10
15.083 ± 0.017	20.427 ± 0.003	0.339 ± 0.001	85.3 ± 0.1	-0.146	0.134	0.012	0.34	0.16	-0.41	-0.07	0.04	-0.21	0.11
16.089 ± 0.026	20.555 ± 0.003	0.335 ± 0.002	85.2 ± 0.2	-0.223	0.165	0.019	0.31	0.01	-0.35	0.18	0.39	-0.25	0.16
17.139 ± 0.027	20.683 ± 0.003	0.337 ± 0.002	85.4 ± 0.2	-0.108	0.146	0.019	0.26	0.38	-0.35	0.30	0.06	-0.18	0.14
18.118 ± 0.025	20.811 ± 0.003	0.330 ± 0.001	85.4 ± 0.2	-0.095	0.178	0.018	0.26	0.44	-0.13	0.24	-0.05	-0.14	0.12
19.145 ± 0.027	20.940 ± 0.003	0.327 ± 0.001	84.8 ± 0.2	-0.070	0.178	0.019	0.23	0.34	-0.12	0.06	-0.18	0.02	0.15
20.061 ± 0.030	21.072 ± 0.003	0.321 ± 0.002	84.9 ± 0.2	-0.032	0.172	0.022	0.15	0.07	0.15	-0.00	-0.20	-0.08	0.17

TABLE 5—Continued

a [arcsec]	μ_R [mag arcsec $^{-2}$]	e	PA [$^{\circ}$]	Δx_c [arcsec]	Δy_c [arcsec]	Err. ^a [arcsec]	a_3/a $\times 100$	b_3/a $\times 100$	a_4/a $\times 100$	b_4/a $\times 100$	a_6/a $\times 100$	b_6/a $\times 100$	Err. ^b
NGC 759													
21.034 ± 0.038	21.203 ± 0.003	0.317 ± 0.002	85.0 ± 0.2	0.025	0.146	0.027	0.35	0.22	0.63	-0.38	0.17	-0.18	0.17
22.155 ± 0.042	21.331 ± 0.004	0.319 ± 0.002	85.1 ± 0.2	0.019	0.140	0.030	0.51	0.20	0.30	-0.10	-0.24	-0.28	0.17
23.126 ± 0.043	21.460 ± 0.005	0.321 ± 0.002	84.8 ± 0.2	0.051	0.140	0.030	0.30	0.01	0.05	0.16	-0.45	0.07	0.19
24.035 ± 0.055	21.593 ± 0.005	0.311 ± 0.002	84.3 ± 0.3	0.025	0.216	0.039	0.25	-0.00	0.11	-0.11	-0.19	-0.27	0.29
25.054 ± 0.067	21.718 ± 0.005	0.308 ± 0.003	84.3 ± 0.4	-0.159	0.223	0.047	0.17	-0.41	0.15	-0.10	-0.41	-0.50	0.32
25.905 ± 0.077	21.847 ± 0.005	0.292 ± 0.003	84.6 ± 0.4	-0.191	0.235	0.054	0.34	-0.25	-0.23	0.27	-0.22	0.29	0.33
26.996 ± 0.105	21.987 ± 0.005	0.286 ± 0.004	84.6 ± 0.6	-0.032	0.197	0.074	0.32	0.16	-0.30	0.15	0.42	0.56	0.45
27.976 ± 0.093	22.103 ± 0.006	0.276 ± 0.003	85.0 ± 0.5	-0.293	0.134	0.066	0.45	-0.15	0.12	0.35	0.44	0.86	0.32
29.305 ± 0.127	22.217 ± 0.006	0.284 ± 0.004	85.1 ± 0.6	-0.261	0.210	0.090	0.32
30.850 ± 0.087	22.342 ± 0.006	0.287 ± 0.003	84.3 ± 0.4	-0.223	0.305	0.062	0.32
32.483 ± 0.095	22.468 ± 0.006	0.282 ± 0.003	83.5 ± 0.4	-0.025	0.184	0.067	0.32
33.960 ± 0.122	22.594 ± 0.007	0.274 ± 0.004	84.2 ± 0.5	0.159	0.299	0.087	0.32
35.374 ± 0.187	22.711 ± 0.008	0.265 ± 0.006	84.6 ± 0.8	-0.000	0.032	0.132	0.32
36.883 ± 0.822	22.829 ± 0.008	0.262 ± 0.023	84.8 ± 3.4	-0.038	-0.025	0.581	0.32
38.794 ± 0.911	22.941 ± 0.008	0.260 ± 0.025	83.7 ± 3.7	0.102	0.159	0.644	0.32

TABLE 5—Continued

a [arcsec]	μ_R [mag arcsec $^{-2}$]	e	PA [$^{\circ}$]	Δx_c [arcsec]	Δy_c [arcsec]	Err. ^a [arcsec]	a_3/a $\times 100$	b_3/a $\times 100$	a_4/a $\times 100$	b_4/a $\times 100$	a_6/a $\times 100$	b_6/a $\times 100$	Err. ^b
7.042 ± 0.017	19.453 ± 0.003	0.074 ± 0.003	26.8 ± 1.3	-0.008	0.012	0.012	0.46
7.362 ± 0.026	19.535 ± 0.004	0.075 ± 0.005	27.4 ± 1.9	-0.014	0.014	0.018	0.46
7.690 ± 0.028	19.619 ± 0.003	0.067 ± 0.005	29.4 ± 2.1	-0.044	0.017	0.019	0.46
8.063 ± 0.031	19.704 ± 0.002	0.063 ± 0.005	29.5 ± 2.5	-0.017	0.053	0.022	0.46
8.505 ± 0.040	19.788 ± 0.003	0.063 ± 0.006	27.9 ± 3.0	-0.086	-0.014	0.028	0.46
9.045 ± 0.030	19.873 ± 0.003	0.077 ± 0.004	26.5 ± 1.8	-0.061	0.030	0.021	0.46
9.494 ± 0.038	19.957 ± 0.003	0.078 ± 0.005	28.4 ± 2.1	-0.070	0.036	0.027	0.46
9.851 ± 0.030	20.035 ± 0.003	0.065 ± 0.004	27.6 ± 1.9	0.003	0.032	0.021	0.46
10.223 ± 0.040	20.104 ± 0.003	0.060 ± 0.005	27.6 ± 2.6	-0.038	0.016	0.028	0.46
10.682 ± 0.046	20.176 ± 0.003	0.066 ± 0.006	26.4 ± 2.7	-0.029	-0.001	0.033	0.46
11.135 ± 0.052	20.252 ± 0.004	0.065 ± 0.006	27.0 ± 2.9	-0.034	0.034	0.037	0.46
11.632 ± 0.056	20.324 ± 0.005	0.079 ± 0.006	27.1 ± 2.5	-0.040	0.027	0.040	0.46
12.044 ± 0.072	20.391 ± 0.005	0.079 ± 0.008	28.9 ± 3.0	0.040	0.003	0.051	0.06	-0.12	0.81	-1.06	0.37	-0.85	0.41
12.451 ± 0.066	20.454 ± 0.005	0.073 ± 0.007	20.8 ± 3.0	0.043	0.033	0.047	0.41
12.951 ± 0.088	20.516 ± 0.005	0.080 ± 0.009	25.9 ± 3.4	0.050	-0.036	0.062	0.41
13.463 ± 0.069	20.577 ± 0.007	0.086 ± 0.007	27.4 ± 2.4	0.051	-0.112	0.049	0.41
13.783 ± 0.069	20.644 ± 0.007	0.081 ± 0.006	27.4 ± 2.5	0.092	-0.054	0.049	0.41
13.978 ± 0.020	20.700 ± 0.003	0.046 ± 0.002	24.2 ± 1.2	0.244	-0.204	0.014	0.16	-0.06	0.25	-0.42	0.28	-0.13	0.14
14.667 ± 0.023	20.800 ± 0.003	0.046 ± 0.002	27.6 ± 1.4	0.257	-0.197	0.016	0.13	-0.03	0.23	-0.47	0.22	-0.11	0.15
15.326 ± 0.026	20.897 ± 0.003	0.046 ± 0.002	27.0 ± 1.5	0.238	-0.147	0.018	-0.08	-0.23	0.11	-0.39	-0.14	0.01	0.16
16.091 ± 0.031	21.001 ± 0.003	0.049 ± 0.003	26.3 ± 1.6	0.200	-0.185	0.022	0.15	0.04	0.30	-0.55	-0.01	0.11	0.19
16.805 ± 0.038	21.104 ± 0.004	0.047 ± 0.003	26.8 ± 1.9	0.244	-0.223	0.027	-0.24	-0.00	0.24	-0.57	0.16	0.30	0.22
17.588 ± 0.037	21.198 ± 0.004	0.044 ± 0.003	30.0 ± 2.0	0.276	-0.172	0.026	-0.19	-0.14	0.22	-0.58	0.14	0.14	0.21
18.397 ± 0.042	21.293 ± 0.004	0.039 ± 0.003	34.9 ± 2.3	0.378	-0.159	0.030	0.18	0.05	0.03	-0.60	0.10	-0.18	0.22
19.557 ± 0.055	21.394 ± 0.004	0.055 ± 0.004	29.8 ± 2.1	0.136	-0.121	0.039	-0.43	0.08	-0.42	-0.21	0.41	0.14	0.25
20.549 ± 0.063	21.494 ± 0.004	0.055 ± 0.004	32.4 ± 2.2	0.168	-0.134	0.044	0.05	0.36	-0.65	-0.36	0.64	0.19	0.27
21.509 ± 0.081	21.588 ± 0.004	0.055 ± 0.005	21.9 ± 3.1	0.327	-0.312	0.057	0.27	0.64	0.09	-0.55	0.24	0.73	0.39
22.725 ± 0.087	21.681 ± 0.005	0.050 ± 0.005	24.6 ± 3.1	0.161	-0.134	0.062	0.47	0.00	-0.57	-0.85	-0.17	0.73	0.38
24.013 ± 0.089	21.777 ± 0.005	0.060 ± 0.005	28.2 ± 2.5	0.187	-0.089	0.063	0.19	-0.20	-1.02	-1.19	0.23	-0.08	0.44
24.996 ± 0.104	21.875 ± 0.005	0.050 ± 0.006	31.6 ± 3.4	0.212	-0.236	0.074	0.41	0.21	-0.69	-0.70	0.56	0.77	0.42
26.033 ± 0.110	21.967 ± 0.006	0.049 ± 0.006	31.5 ± 3.5	0.276	-0.166	0.078	0.09	0.03	-0.20	-0.90	0.93	0.76	0.44
27.361 ± 0.131	22.066 ± 0.005	0.047 ± 0.007	35.0 ± 4.1	0.314	-0.057	0.093	0.25	0.44	-0.69	-0.61	0.98	0.12	0.42
29.225 ± 0.100	22.184 ± 0.005	0.056 ± 0.005	32.0 ± 2.4	0.066	-0.153	0.070	0.42
30.560 ± 0.081	22.299 ± 0.005	0.053 ± 0.004	24.8 ± 2.0	0.085	-0.191	0.057	-0.11	-0.60	0.10	-1.15	0.20	0.13	0.25
31.656 ± 0.089	22.388 ± 0.006	0.044 ± 0.004	22.0 ± 2.5	-0.029	-0.293	0.063	0.11	-0.41	0.24	-1.00	0.16	-0.14	0.28
32.840 ± 0.123	22.473 ± 0.007	0.054 ± 0.005	19.4 ± 2.8	-0.093	-0.293	0.087	0.28
33.880 ± 0.175	22.560 ± 0.007	0.050 ± 0.007	19.0 ± 4.1	-0.195	-0.299	0.124	0.28
35.114 ± 0.346	22.646 ± 0.007	0.056 ± 0.013	20.4 ± 7.2	-0.118	-0.306	0.245	0.28
36.514 ± 0.548	22.733 ± 0.007	0.055 ± 0.020	16.4 ± 11.1	-0.048	-0.108	0.388	0.28
37.824 ± 0.746	22.830 ± 0.008	0.050 ± 0.027	17.4 ± 15.9	-0.074	-0.134	0.528	0.28
39.472 ± 0.579	22.950 ± 0.010	0.064 ± 0.019	18.4 ± 9.2	-0.106	-0.096	0.410	0.28
40.874 ± 0.196	23.055 ± 0.011	0.057 ± 0.006	20.5 ± 3.4	0.021	0.127	0.138	0.28
41.968 ± 0.386	23.135 ± 0.011	0.057 ± 0.012	22.9 ± 6.5	0.047	0.063	0.273	0.015	0.28

UGC 1308

0.017 ± 0.000	15.569 ± 0.010	0.005 ± 0.000	90.0 ± 0.0	0.032	-0.004	0.000	0.00	0.00	0.00	0.00	0.00	0.00	0.00
0.030 ± 0.007	15.652 ± 0.022	0.086 ± 0.322	61.3 ± 117.	0.000	0.000	0.005	-0.77	-5.73	-0.59	1.11	-2.73	0.28	1.33
0.078 ± 0.002	15.779 ± 0.022	0.205 ± 0.033	41.6 ± 5.8	-0.010	0.015	0.002	4.00	-3.61	-0.45	0.77	-0.53	0.42	0.41
0.137 ± 0.003	15.915 ± 0.007	0.171 ± 0.027	38.6 ± 5.4	-0.043	0.046	0.002	-5.68	-2.18	-3.62	0.80	0.76	-0.82	0.53
0.233 ± 0.005	16.039 ± 0.004	0.002 ± 0.031	109.7 ± 480.	-0.120	0.100	0.004	-6.19	-4.24	1.38	4.02	4.14	0.37	0.74
0.368 ± 0.005	16.154 ± 0.004	0.185 ± 0.015	130.0 ± 2.9	-0.170	0.121	0.003	-4.06	1.22	1.03	2.84	0.95	-0.99	0.88
0.482 ± 0.004	16.271 ± 0.003	0.204 ± 0.009	131.1 ± 1.6	-0.217	0.130	0.003	0.58	-0.63	-1.69	2.66	-1.85	-0.31	0.59
0.598 ± 0.005	16.386 ± 0.003	0.125 ± 0.011	144.8 ± 2.8	-0.292	0.137	0.004	-0.64	-5.06	-0.51	1.80	-0.82	0.81	0.55
0.780 ± 0.006	16.499 ± 0.003	0.218 ± 0.008	166.0 ± 1.4	-0.332	0.134	0.004	-1.85	-0.79	0.58	4.03	1.69	-0.75	0.70
0.929 ± 0.006	16.611 ± 0.003	0.208 ± 0.007	174.0 ± 1.2	-0.356	0.106	0.004	-0.18	-1.00	-0.04	2.14	1.46	-1.95	0.53
1.065 ± 0.006	16.723 ± 0.003	0.208 ± 0.006	174.9 ± 1.0	-0.370	0.098	0.004	-1.23	-0.64	1.00	-1.27	0.34	-0.42	0.56
1.194 ± 0.007	16.831 ± 0.002	0.144 ± 0.008	3.1 ± 1.7	-0.438	0.133	0.005	-3.57	0.40	-2.56	-0.41	-0.38	1.37	0.56
1.383 ± 0.010	16.936 ± 0.002	0.146 ± 0.009	178.0 ± 2.0	-0.496	0.187	0.007	-0.67	-0.66	-0.60	2.75	0.96	2.12	0.50
1.627 ± 0.011	17.039 ± 0.002	0.189 ± 0.008	165.5 ± 1.4	-0.530	0.255	0.008	0.81	-0.87	-0.60	1.53	0.04	0.20	0.58
1.860 ± 0.013	17.142 ± 0.002	0.168 ± 0.008	165.2 ± 1.7	-0.494	0.277	0.009	0.09	-0.80	-1.20	1.90	-0.12	0.64	0.43
2.020 ± 0.015	17.239 ± 0.002	0.117 ± 0.009	167.6 ± 2.5	-0.476	0.303	0.010	0.02	-0.05	-0.45	0.20	-0.22	2.02	0.38
2.301 ± 0.017	17.339 ± 0.002	0.161 ± 0.009	151.7 ± 1.9	-0.436	0.409	0.012	0.24	0.16	0.71	0.30	-0.27	0.78	0.57
2.589 ± 0.021	17.434 ± 0.002	0.124 ± 0.010	155.5 ± 2.6	-0.383	0.340	0.015	0.57

TABLE 5—Continued

a [arcsec]	μ_R [mag arcsec $^{-2}$]	e	PA [$^{\circ}$]	Δx_c [arcsec]	Δy_c [arcsec]	Err. ^a [arcsec]	a_3/a $\times 100$	b_3/a $\times 100$	a_4/a $\times 100$	b_4/a $\times 100$	a_6/a $\times 100$	b_6/a $\times 100$	Err. ^b
2.894 ± 0.033	17.469 ± 0.004	0.139 ± 0.014	157.3 ± 3.3	-0.381	0.292	0.023	-0.41	-0.55	2.23	-0.45	1.33	-0.45	0.34
3.169 ± 0.021	17.483 ± 0.004	0.142 ± 0.008	157.8 ± 1.9	-0.381	0.264	0.015	-0.52	-0.56	2.43	-0.78	1.36	-0.85	0.27
3.485 ± 0.015	17.598 ± 0.002	0.085 ± 0.006	165.4 ± 2.1	-0.199	0.134	0.011	0.27
3.819 ± 0.007	17.759 ± 0.002	0.023 ± 0.003	22.2 ± 3.4	0.050	0.005	0.005	0.27
4.084 ± 0.006	17.865 ± 0.002	0.028 ± 0.002	30.3 ± 2.7	0.061	-0.002	0.004	-0.20	-0.26	-0.26	0.27	-0.16	-0.10	0.13
4.346 ± 0.007	17.940 ± 0.002	0.018 ± 0.002	23.2 ± 3.3	0.072	-0.006	0.005	-0.04	-0.14	-0.15	-0.08	0.06	-0.34	0.17
4.604 ± 0.008	18.011 ± 0.002	0.016 ± 0.002	19.4 ± 4.3	0.091	0.018	0.006	0.05	-0.33	-0.45	-0.11	0.16	-0.11	0.21
4.852 ± 0.009	18.076 ± 0.002	0.012 ± 0.003	9.3 ± 6.5	0.090	0.021	0.006	0.13	0.11	-0.26	-0.17	0.22	0.02	0.19
5.126 ± 0.011	18.139 ± 0.002	0.011 ± 0.003	13.0 ± 8.1	0.099	0.032	0.008	0.19
5.378 ± 0.010	18.196 ± 0.002	0.006 ± 0.003	71.3 ± 12.9	0.100	0.034	0.007	0.08	0.05	0.63	0.26	0.08	-0.07	0.16
5.632 ± 0.012	18.250 ± 0.002	0.004 ± 0.003	76.0 ± 20.4	0.106	0.044	0.008	0.16
5.882 ± 0.012	18.301 ± 0.003	0.004 ± 0.003	92.7 ± 21.2	0.131	0.035	0.009	-0.03	0.03	0.19	-0.12	-0.28	0.20	0.24
6.154 ± 0.016	18.345 ± 0.003	0.004 ± 0.004	113.6 ± 24.9	0.137	0.041	0.011	0.24
6.463 ± 0.013	18.388 ± 0.003	0.016 ± 0.003	121.4 ± 5.1	0.172	0.022	0.009	0.24
6.739 ± 0.015	18.429 ± 0.003	0.019 ± 0.003	110.8 ± 4.8	0.163	0.027	0.011	0.47	0.26	-0.29	-0.05	0.29	0.55	0.17
7.007 ± 0.018	18.466 ± 0.004	0.026 ± 0.004	107.7 ± 3.9	0.190	0.041	0.013	0.17
7.247 ± 0.019	18.500 ± 0.004	0.025 ± 0.004	107.7 ± 4.3	0.191	0.059	0.013	0.17
7.456 ± 0.021	18.522 ± 0.005	0.027 ± 0.004	111.0 ± 4.3	0.198	0.065	0.015	0.59	0.17	0.01	0.31	0.26	0.69	0.23
7.640 ± 0.023	18.553 ± 0.006	0.026 ± 0.004	114.6 ± 4.7	0.200	0.066	0.016	0.23
7.796 ± 0.036	18.591 ± 0.007	0.021 ± 0.006	110.6 ± 8.7	0.220	0.024	0.025	0.23
7.984 ± 0.059	18.701 ± 0.009	0.072 ± 0.010	104.2 ± 4.2	0.760	0.272	0.042	0.84
8.484 ± 0.056	18.849 ± 0.008	0.050 ± 0.009	96.6 ± 5.4	0.626	0.196	0.039	0.84
9.650 ± 0.043	19.005 ± 0.008	0.092 ± 0.006	103.5 ± 2.0	0.855	0.240	0.031	0.07	0.11	-1.83	-0.29	-0.02	0.07	0.35
10.531 ± 0.071	19.160 ± 0.009	0.097 ± 0.009	102.3 ± 2.8	0.849	0.151	0.051	0.15	-0.07	-3.21	-0.85	-0.47	-0.46	0.39
11.486 ± 0.073	19.302 ± 0.009	0.087 ± 0.008	101.7 ± 2.9	0.836	0.170	0.051	0.04	-0.10	-1.66	-1.12	-0.03	-0.00	0.54
12.572 ± 0.089	19.454 ± 0.010	0.104 ± 0.009	106.0 ± 2.7	0.747	0.266	0.063	0.21	-0.18	-1.48	-1.09	-1.01	0.55	0.50
13.556 ± 0.094	19.591 ± 0.010	0.108 ± 0.009	107.0 ± 2.6	0.734	0.272	0.066	0.13	-0.02	-0.72	0.08	0.30	1.09	0.70
14.690 ± 0.151	19.744 ± 0.011	0.108 ± 0.013	101.3 ± 3.9	0.715	0.107	0.107	0.23	0.13	2.36	0.11	-0.86	1.66	0.73
15.651 ± 0.161	19.888 ± 0.012	0.103 ± 0.013	100.6 ± 4.1	0.639	0.075	0.114	0.01	0.00	1.03	-1.91	0.46	-0.06	0.64
16.692 ± 0.209	19.997 ± 0.013	0.117 ± 0.016	110.7 ± 4.3	0.416	0.329	0.148	0.23	-0.03	-1.43	-2.40	-2.15	-0.25	0.59
17.618 ± 0.214	20.146 ± 0.014	0.097 ± 0.015	100.1 ± 5.1	0.416	0.285	0.151	-0.01	0.01	0.28	-1.41	-0.12	-2.37	0.67
18.758 ± 0.234	20.283 ± 0.017	0.108 ± 0.016	99.0 ± 4.7	0.425	0.253	0.166	-0.06	0.06	0.63	0.51	-0.16	-1.84	0.74
19.848 ± 0.307	20.388 ± 0.017	0.111 ± 0.019	101.0 ± 5.7	0.435	0.253	0.217	0.74
20.981 ± 0.345	20.537 ± 0.018	0.093 ± 0.021	106.7 ± 7.2	0.435	0.253	0.244	0.74
22.380 ± 0.515	20.661 ± 0.023	0.105 ± 0.029	103.2 ± 8.9	0.435	0.253	0.364	0.74
23.338 ± 0.517	20.765 ± 0.022	0.118 ± 0.028	107.6 ± 7.6	0.435	0.253	0.365	0.74
25.848 ± 0.442	20.918 ± 0.022	0.165 ± 0.020	110.1 ± 4.2	0.435	0.253	0.312	0.74
26.847 ± 0.546	21.067 ± 0.031	0.151 ± 0.024	108.4 ± 5.5	0.435	0.253	0.386	0.74
27.828 ± 0.533	21.160 ± 0.031	0.163 ± 0.023	105.0 ± 4.8	0.524	0.266	0.377	0.74

^aError on the center coordinates derived from the residual rms of the ellipse fit to the isophotes: Err = rms_{fit}/ \sqrt{N} with $N \leq 128$ the number of fitted points of the isophote.^bError of Fourier coefficients defined as Err = $\sqrt{\frac{\sum_{i=10}^{N/2} (a_i^2 + b_i^2)}{N/2 - 10}} \times \frac{100}{a}$.

TABLE 6
STELLAR KINEMATICS OF THE SAMPLE GALAXIES

r [arcsec]	V [km s $^{-1}$]	σ [km s $^{-1}$]	H_3	H_4	PA [$^{\circ}$]	Run
IC 171						
-11.71	-8.8 ± 19.3	130.4 ± 24.0	0.033 ± 0.094	0.068 ± 0.114	10	2
-8.47	-3.5 ± 14.2	157.4 ± 17.2	0.036 ± 0.059	0.084 ± 0.073	10	2
-5.27	16.9 ± 12.8	192.1 ± 12.7	-0.042 ± 0.042	0.056 ± 0.043	10	2
-2.84	11.5 ± 8.7	191.1 ± 7.2	-0.006 ± 0.023	0.050 ± 0.026	10	2
-1.08	31.1 ± 3.7	178.9 ± 4.5	-0.024 ± 0.016	0.039 ± 0.018	10	2
-0.23	9.3 ± 3.6	160.4 ± 4.1	-0.019 ± 0.018	-0.010 ± 0.021	10	2
0.38	0.6 ± 3.7	157.7 ± 5.1	-0.016 ± 0.019	0.059 ± 0.023	10	2
0.98	-11.1 ± 8.0	170.3 ± 4.9	-0.024 ± 0.019	0.038 ± 0.021	10	2
2.12	-18.3 ± 5.7	189.8 ± 6.6	-0.053 ± 0.023	0.050 ± 0.025	10	2
3.94	-16.3 ± 9.3	178.0 ± 12.1	0.029 ± 0.046	0.034 ± 0.049	10	2
6.29	-23.8 ± 11.0	190.7 ± 13.1	0.003 ± 0.048	-0.001 ± 0.056	10	2
11.64	-31.9 ± 17.8	153.8 ± 23.5	-0.033 ± 0.090	0.069 ± 0.072	10	2
-20.54	143.5 ± 22.8	146.3 ± 27.1	0.012 ± 0.133	-0.021 ± 0.142	110	1
-12.32	159.1 ± 14.5	135.8 ± 17.9	0.038 ± 0.089	-0.014 ± 0.105	110	1
-9.11	143.5 ± 13.5	170.5 ± 15.3	-0.066 ± 0.066	-0.011 ± 0.072	110	1
-6.31	103.4 ± 8.2	186.2 ± 8.3	-0.026 ± 0.039	-0.071 ± 0.037	110	1
-3.98	62.0 ± 10.8	176.4 ± 8.1	-0.032 ± 0.033	0.008 ± 0.036	110	1
-2.49	70.0 ± 12.0	175.9 ± 6.7	-0.059 ± 0.029	-0.020 ± 0.032	110	1
-1.28	52.8 ± 7.7	176.9 ± 5.7	-0.081 ± 0.021	0.030 ± 0.024	110	1
-0.39	15.8 ± 8.3	172.5 ± 5.3	-0.058 ± 0.023	-0.023 ± 0.025	110	1
0.21	-19.5 ± 4.9	176.3 ± 5.2	-0.019 ± 0.020	0.023 ± 0.022	110	1
1.10	-40.0 ± 7.5	189.0 ± 4.8	0.024 ± 0.018	0.011 ± 0.019	110	1
2.31	-74.1 ± 13.0	176.8 ± 7.2	0.109 ± 0.026	0.048 ± 0.029	110	1
3.80	-112.9 ± 8.2	186.2 ± 7.5	0.118 ± 0.027	0.028 ± 0.030	110	1
5.89	-113.5 ± 8.7	199.7 ± 6.9	0.075 ± 0.032	-0.068 ± 0.031	110	1
9.32	-138.6 ± 11.4	172.3 ± 11.4	0.035 ± 0.040	0.045 ± 0.047	110	1
14.21	-158.4 ± 18.6	131.6 ± 15.6	-0.047 ± 0.065	0.008 ± 0.091	110	1
-13.85	121.4 ± 26.1	123.8 ± 33.7	0.005 ± 0.184	-0.029 ± 0.206	110	2
-8.82	118.9 ± 18.2	138.6 ± 22.9	0.006 ± 0.106	0.027 ± 0.099	110	2
-5.36	99.3 ± 18.3	163.2 ± 13.6	-0.028 ± 0.060	-0.011 ± 0.066	110	2
-2.80	93.7 ± 10.6	179.4 ± 11.6	-0.078 ± 0.039	0.067 ± 0.046	110	2
-1.32	47.5 ± 6.8	170.8 ± 7.0	-0.012 ± 0.025	0.051 ± 0.030	110	2
-0.46	28.7 ± 5.4	151.4 ± 6.2	0.011 ± 0.026	0.018 ± 0.031	110	2
0.15	-6.1 ± 6.0	153.8 ± 5.7	-0.021 ± 0.030	-0.048 ± 0.031	110	2
0.75	-40.6 ± 5.5	158.2 ± 7.0	0.024 ± 0.029	0.017 ± 0.034	110	2
1.62	-58.6 ± 9.9	178.3 ± 7.8	0.003 ± 0.030	0.008 ± 0.033	110	2
3.11	-97.9 ± 10.0	153.4 ± 11.5	0.031 ± 0.048	0.012 ± 0.058	110	2
5.71	-82.7 ± 12.2	164.2 ± 12.8	0.017 ± 0.050	0.034 ± 0.057	110	2
8.86	-98.1 ± 14.8	141.3 ± 16.8	-0.028 ± 0.085	-0.024 ± 0.097	110	2
12.26	-124.9 ± 20.9	120.8 ± 24.3	-0.022 ± 0.130	-0.013 ± 0.154	110	2
-12.15	143.7 ± 19.7	148.2 ± 24.9	-0.011 ± 0.108	0.019 ± 0.113	145	2
-7.28	115.7 ± 13.1	166.2 ± 13.9	-0.017 ± 0.066	-0.040 ± 0.068	145	2
-4.93	96.7 ± 10.4	163.2 ± 12.4	-0.044 ± 0.055	-0.021 ± 0.062	145	2
-2.71	79.7 ± 9.2	165.6 ± 7.4	-0.100 ± 0.028	0.052 ± 0.033	145	2
-1.00	40.4 ± 9.0	172.3 ± 4.3	-0.035 ± 0.018	0.011 ± 0.020	145	2
-0.14	10.8 ± 3.8	160.6 ± 4.4	0.009 ± 0.019	0.011 ± 0.022	145	2
0.46	-12.4 ± 3.7	163.2 ± 4.4	0.020 ± 0.019	0.007 ± 0.021	145	2
1.32	-42.4 ± 5.6	164.9 ± 3.8	0.069 ± 0.017	0.005 ± 0.018	145	2
2.78	-77.9 ± 5.0	178.5 ± 7.1	0.072 ± 0.023	0.070 ± 0.028	145	2
4.66	-79.7 ± 11.4	179.6 ± 9.4	0.041 ± 0.033	0.046 ± 0.038	145	2
6.73	-87.4 ± 10.1	176.0 ± 11.0	0.095 ± 0.035	0.073 ± 0.042	145	2
10.30	-89.9 ± 18.7	198.1 ± 19.3	0.022 ± 0.079	-0.042 ± 0.081	145	2
16.98	-97.4 ± 21.1	189.6 ± 22.7	0.079 ± 0.097	0.018 ± 0.091	145	2

NGC 679

TABLE 6—Continued

<i>r</i> [arcsec]	<i>V</i> [km s ⁻¹]	σ [km s ⁻¹]	<i>H</i> ₃	<i>H</i> ₄	PA [°]	Run
-14.75	-74.2 ± 29.5	186.8 ± 32.9	-0.032 ± 0.134	-0.007 ± 0.134	0	1
-10.93	-56.3 ± 17.4	170.9 ± 20.5	0.107 ± 0.081	-0.010 ± 0.092	0	1
-8.13	-24.2 ± 11.2	191.7 ± 12.9	0.030 ± 0.050	-0.005 ± 0.054	0	1
-5.78	-20.6 ± 8.5	203.4 ± 9.5	0.038 ± 0.037	-0.025 ± 0.041	0	1
-3.94	-21.5 ± 7.7	225.5 ± 6.0	0.020 ± 0.019	0.006 ± 0.022	0	1
-2.48	-21.8 ± 6.4	221.7 ± 5.5	0.004 ± 0.017	0.035 ± 0.019	0	1
-1.61	-25.9 ± 9.3	249.2 ± 6.0	0.011 ± 0.014	0.067 ± 0.016	0	1
-1.01	-14.4 ± 5.4	251.0 ± 4.7	0.014 ± 0.012	0.050 ± 0.014	0	1
-0.40	-11.9 ± 6.1	247.0 ± 4.2	-0.006 ± 0.012	0.029 ± 0.013	0	1
0.21	3.7 ± 4.4	244.2 ± 4.4	-0.012 ± 0.012	0.041 ± 0.013	0	1
0.81	18.8 ± 7.9	253.1 ± 5.6	-0.036 ± 0.014	0.025 ± 0.017	0	1
1.68	27.4 ± 5.4	243.3 ± 5.2	-0.011 ± 0.017	-0.005 ± 0.019	0	1
3.14	34.2 ± 6.2	226.8 ± 6.1	-0.034 ± 0.020	0.011 ± 0.021	0	1
4.98	34.0 ± 9.6	215.0 ± 11.7	-0.027 ± 0.034	0.046 ± 0.038	0	1
7.32	54.0 ± 10.3	192.9 ± 12.3	0.035 ± 0.046	0.005 ± 0.048	0	1
10.12	51.2 ± 18.6	146.7 ± 23.8	0.045 ± 0.089	0.004 ± 0.103	0	1
13.54	47.8 ± 30.3	227.9 ± 30.9	0.096 ± 0.076	0.036 ± 0.091	0	1
-6.05	-12.6 ± 23.6	230.0 ± 23.3	0.014 ± 0.070	-0.001 ± 0.082	0	2
-2.99	-37.9 ± 11.2	211.5 ± 11.6	0.034 ± 0.034	0.059 ± 0.037	0	2
-1.54	-12.4 ± 8.0	235.6 ± 7.0	0.026 ± 0.022	0.012 ± 0.024	0	2
-0.66	4.1 ± 6.6	227.6 ± 8.7	0.007 ± 0.024	0.061 ± 0.028	0	2
-0.06	12.8 ± 7.4	230.9 ± 8.3	-0.009 ± 0.026	0.088 ± 0.029	0	2
0.55	8.3 ± 7.6	246.0 ± 8.7	0.009 ± 0.025	0.012 ± 0.029	0	2
1.43	11.2 ± 8.4	247.9 ± 8.9	0.023 ± 0.022	0.044 ± 0.025	0	2
2.63	42.7 ± 10.1	240.7 ± 10.2	0.017 ± 0.030	0.030 ± 0.032	0	2
4.33	46.5 ± 14.1	238.3 ± 17.0	0.002 ± 0.038	0.089 ± 0.042	0	2
7.41	24.0 ± 18.9	191.3 ± 26.6	0.035 ± 0.084	0.052 ± 0.098	0	2
-10.17	-63.0 ± 15.7	155.5 ± 22.4	0.049 ± 0.082	0.057 ± 0.095	90	2
-6.60	-13.5 ± 20.9	236.5 ± 13.5	-0.041 ± 0.045	-0.020 ± 0.051	90	2
-3.50	-7.8 ± 9.2	230.5 ± 6.3	0.017 ± 0.018	0.026 ± 0.021	90	2
-1.82	-2.2 ± 6.3	247.4 ± 5.9	0.022 ± 0.014	0.082 ± 0.016	90	2
-0.96	2.8 ± 5.7	242.3 ± 4.8	0.009 ± 0.013	0.047 ± 0.015	90	2
-0.36	-5.4 ± 4.3	235.9 ± 4.5	0.021 ± 0.012	0.050 ± 0.014	90	2
0.25	-3.4 ± 4.8	232.2 ± 5.1	0.027 ± 0.014	0.045 ± 0.016	90	2
0.85	3.5 ± 6.5	234.3 ± 5.0	0.018 ± 0.014	0.053 ± 0.015	90	2
1.71	14.7 ± 5.5	233.9 ± 4.7	-0.049 ± 0.014	0.029 ± 0.016	90	2
3.39	18.4 ± 5.5	231.2 ± 6.7	0.033 ± 0.018	0.054 ± 0.021	90	2
6.49	27.0 ± 12.6	207.6 ± 16.4	0.011 ± 0.048	0.096 ± 0.049	90	2
10.08	28.4 ± 18.5	212.9 ± 22.3	0.003 ± 0.067	0.067 ± 0.072	90	2
-9.47	-65.4 ± 14.6	186.7 ± 19.4	-0.021 ± 0.068	0.054 ± 0.070	135	2
-5.65	-50.2 ± 12.2	217.8 ± 12.0	0.030 ± 0.037	0.037 ± 0.040	135	2
-2.95	-38.3 ± 6.0	225.0 ± 7.2	0.035 ± 0.021	0.055 ± 0.024	135	2
-1.49	-24.1 ± 5.3	245.6 ± 5.9	0.043 ± 0.015	0.057 ± 0.018	135	2
-0.63	-16.0 ± 4.2	253.1 ± 5.4	0.043 ± 0.014	0.031 ± 0.017	135	2
-0.02	7.3 ± 3.4	245.1 ± 4.5	0.042 ± 0.011	0.036 ± 0.014	135	2
0.58	21.3 ± 4.2	240.3 ± 4.2	0.039 ± 0.011	0.028 ± 0.014	135	2
1.19	20.1 ± 5.1	231.5 ± 4.7	0.005 ± 0.014	0.036 ± 0.016	135	2
1.80	15.0 ± 6.2	230.5 ± 5.9	-0.004 ± 0.015	0.061 ± 0.018	135	2
2.66	21.2 ± 5.4	250.0 ± 5.7	0.003 ± 0.016	0.046 ± 0.017	135	2
4.12	44.2 ± 6.8	222.4 ± 6.2	0.027 ± 0.020	0.012 ± 0.022	135	2
5.96	37.2 ± 9.1	223.5 ± 10.2	-0.037 ± 0.033	0.002 ± 0.038	135	2
8.53	27.6 ± 16.0	199.1 ± 15.4	0.044 ± 0.046	0.064 ± 0.050	135	2
NGC 687						
-9.77	-31.0 ± 19.0	228.2 ± 22.6	-0.013 ± 0.073	0.009 ± 0.079	0	1
-7.32	-16.3 ± 11.5	184.6 ± 18.5	0.035 ± 0.054	0.100 ± 0.065	0	1

TABLE 6—Continued

<i>r</i> [arcsec]	<i>V</i> [km s ⁻¹]	σ [km s ⁻¹]	<i>H</i> ₃	<i>H</i> ₄	PA [°]	Run
-4.99	-21.2 ± 12.6	209.9 ± 11.7	-0.030 ± 0.037	0.022 ± 0.042	0	1
-2.76	-1.3 ± 9.2	227.2 ± 7.8	0.002 ± 0.022	0.046 ± 0.024	0	1
-1.67	3.8 ± 6.7	231.0 ± 5.4	-0.013 ± 0.015	0.042 ± 0.017	0	1
-0.82	4.1 ± 4.9	244.2 ± 4.2	-0.006 ± 0.013	-0.001 ± 0.015	0	1
-0.21	3.3 ± 6.2	244.7 ± 4.1	-0.014 ± 0.012	0.014 ± 0.014	0	1
0.39	-4.3 ± 4.5	242.8 ± 4.2	0.001 ± 0.012	0.022 ± 0.014	0	1
1.25	-4.6 ± 7.0	224.5 ± 4.6	-0.029 ± 0.014	0.022 ± 0.016	0	1
2.71	-0.8 ± 5.7	225.2 ± 7.3	0.002 ± 0.022	0.044 ± 0.024	0	1
4.57	-18.9 ± 9.9	243.3 ± 9.3	-0.049 ± 0.033	-0.051 ± 0.035	0	1
6.89	-12.0 ± 20.7	225.2 ± 10.7	0.025 ± 0.046	-0.096 ± 0.046	0	1
-9.43	-4.0 ± 21.0	183.4 ± 27.3	-0.023 ± 0.093	0.027 ± 0.110	20	2
-6.73	-1.8 ± 13.9	184.5 ± 16.6	-0.041 ± 0.056	0.070 ± 0.062	20	2
-3.60	5.8 ± 9.0	206.0 ± 8.8	-0.004 ± 0.026	0.081 ± 0.029	20	2
-1.70	11.5 ± 7.6	231.9 ± 5.8	-0.006 ± 0.018	0.033 ± 0.019	20	2
-0.85	12.8 ± 4.2	231.7 ± 4.7	-0.016 ± 0.014	0.031 ± 0.016	20	2
-0.24	1.3 ± 3.7	244.0 ± 4.4	0.009 ± 0.013	0.022 ± 0.015	20	2
0.36	-11.1 ± 3.7	234.6 ± 4.4	0.016 ± 0.014	0.014 ± 0.015	20	2
0.97	-7.9 ± 4.4	236.8 ± 5.0	-0.004 ± 0.014	0.041 ± 0.015	20	2
1.82	-5.7 ± 4.7	224.7 ± 6.0	0.036 ± 0.017	0.076 ± 0.019	20	2
3.73	-6.0 ± 10.0	207.7 ± 8.6	-0.036 ± 0.027	0.065 ± 0.029	20	2
7.08	-44.0 ± 14.7	193.2 ± 20.1	0.012 ± 0.060	0.076 ± 0.069	20	2
-12.03	-85.7 ± 21.0	199.7 ± 24.7	0.016 ± 0.093	-0.012 ± 0.100	110	2
-6.97	-17.3 ± 10.7	213.2 ± 11.9	-0.012 ± 0.048	-0.030 ± 0.049	110	2
-3.83	-4.5 ± 6.1	230.8 ± 6.6	0.027 ± 0.020	0.017 ± 0.024	110	2
-1.90	-4.6 ± 4.5	237.3 ± 4.8	-0.005 ± 0.014	0.023 ± 0.016	110	2
-1.05	-11.4 ± 3.7	247.7 ± 4.2	-0.013 ± 0.012	0.010 ± 0.014	110	2
-0.44	0.1 ± 4.6	244.0 ± 4.0	-0.010 ± 0.013	-0.018 ± 0.014	110	2
0.16	4.7 ± 4.2	241.2 ± 4.6	-0.026 ± 0.014	0.015 ± 0.015	110	2
0.77	0.8 ± 6.2	241.8 ± 4.3	-0.031 ± 0.013	0.025 ± 0.014	110	2
1.62	2.4 ± 6.7	229.4 ± 6.1	-0.028 ± 0.017	0.076 ± 0.018	110	2
3.54	18.7 ± 7.5	213.9 ± 7.7	0.002 ± 0.024	0.050 ± 0.026	110	2
6.66	11.6 ± 10.7	216.1 ± 12.2	0.026 ± 0.044	-0.008 ± 0.048	110	2
12.25	30.3 ± 27.3	217.2 ± 28.3	0.009 ± 0.080	0.076 ± 0.081	110	2
NGC 703						
-7.84	-90.0 ± 16.7	135.5 ± 22.7	0.003 ± 0.108	0.001 ± 0.126	0	2
-5.12	-92.3 ± 18.6	153.4 ± 11.0	0.032 ± 0.053	-0.034 ± 0.058	0	2
-2.68	-98.2 ± 6.4	193.4 ± 8.4	0.045 ± 0.027	0.049 ± 0.031	0	2
-1.22	-51.5 ± 5.2	224.9 ± 5.1	0.043 ± 0.016	0.017 ± 0.019	0	2
-0.35	-14.3 ± 6.5	238.2 ± 5.9	-0.003 ± 0.019	-0.001 ± 0.022	0	2
0.51	26.8 ± 6.0	223.2 ± 5.0	-0.033 ± 0.016	0.008 ± 0.018	0	2
1.93	73.9 ± 6.3	195.9 ± 7.7	0.056 ± 0.026	0.046 ± 0.028	0	2
3.79	107.0 ± 11.7	187.9 ± 17.0	0.064 ± 0.051	0.105 ± 0.056	0	2
7.44	139.0 ± 17.2	119.7 ± 21.5	-0.015 ± 0.114	-0.012 ± 0.144	0	2
-8.96	-185.9 ± 12.5	121.0 ± 17.4	-0.051 ± 0.082	0.020 ± 0.106	45	1
-5.38	-189.2 ± 10.3	136.2 ± 9.7	0.020 ± 0.042	0.023 ± 0.052	45	1
-2.32	-145.4 ± 5.6	192.3 ± 6.3	0.105 ± 0.024	-0.007 ± 0.028	45	1
-0.88	-73.7 ± 4.3	227.6 ± 4.7	0.059 ± 0.015	0.009 ± 0.017	45	1
-0.01	5.6 ± 5.1	250.7 ± 5.9	-0.003 ± 0.015	0.036 ± 0.018	45	1
0.85	67.2 ± 4.3	222.5 ± 5.0	-0.064 ± 0.014	0.035 ± 0.016	45	1
2.30	157.4 ± 7.4	179.9 ± 6.3	-0.121 ± 0.025	0.000 ± 0.029	45	1
5.49	179.9 ± 6.9	156.6 ± 9.4	-0.055 ± 0.038	0.029 ± 0.044	45	1
9.18	184.4 ± 13.6	112.1 ± 19.0	-0.029 ± 0.096	0.034 ± 0.118	45	1
-8.33	10.3 ± 17.0	123.3 ± 24.8	-0.053 ± 0.074	0.007 ± 0.105	135	2
-5.53	1.4 ± 16.8	182.7 ± 19.1	-0.057 ± 0.068	0.023 ± 0.081	135	2
-2.71	3.3 ± 6.6	186.1 ± 6.8	-0.020 ± 0.025	0.027 ± 0.027	135	2
-1.00	3.2 ± 7.4	251.8 ± 5.2	-0.020 ± 0.014	0.039 ± 0.016	135	2

TABLE 6—Continued

<i>r</i> [arcsec]	<i>V</i> [km s ⁻¹]	σ [km s ⁻¹]	<i>H</i> ₃	<i>H</i> ₄	PA [°]	Run
-0.16	8.8 ± 7.2	246.9 ± 6.1	0.007 ± 0.018	0.001 ± 0.021	135	2
0.44	3.5 ± 7.0	253.6 ± 5.9	0.015 ± 0.016	0.016 ± 0.019	135	2
1.29	-0.9 ± 9.2	223.6 ± 6.7	0.038 ± 0.019	0.072 ± 0.020	135	2
3.82	-15.4 ± 11.5	188.3 ± 10.1	-0.036 ± 0.037	0.022 ± 0.041	135	2
8.13	-14.2 ± 19.6	126.0 ± 25.3	-0.061 ± 0.094	-0.025 ± 0.104	135	2
NGC 708						
-5.43	41.5 ± 21.7	226.4 ± 28.9	-0.015 ± 0.079	0.006 ± 0.090	0	1
-2.40	20.5 ± 15.3	205.8 ± 14.4	0.009 ± 0.047	0.018 ± 0.054	0	1
-0.37	-3.1 ± 9.9	220.7 ± 10.5	-0.030 ± 0.039	-0.043 ± 0.042	0	1
1.39	-27.4 ± 11.9	196.1 ± 13.0	0.025 ± 0.045	0.018 ± 0.050	0	1
4.16	-28.1 ± 13.3	207.1 ± 15.0	0.053 ± 0.056	-0.015 ± 0.060	0	1
8.56	-3.2 ± 23.5	173.7 ± 28.8	0.053 ± 0.092	-0.022 ± 0.119	0	1
-10.05	3.9 ± 24.6	210.7 ± 29.8	-0.012 ± 0.096	0.009 ± 0.114	40	2
-6.58	-1.2 ± 19.3	202.4 ± 17.4	0.047 ± 0.074	-0.088 ± 0.075	40	2
-4.13	4.9 ± 10.4	198.3 ± 11.1	0.025 ± 0.042	-0.012 ± 0.045	40	2
-2.42	-2.9 ± 7.9	199.3 ± 8.7	-0.035 ± 0.034	-0.019 ± 0.036	40	2
-1.23	-5.2 ± 9.0	226.8 ± 9.2	0.055 ± 0.030	-0.009 ± 0.035	40	2
-0.03	4.1 ± 9.6	225.7 ± 10.0	-0.012 ± 0.032	0.007 ± 0.036	40	2
1.19	-0.8 ± 9.8	208.7 ± 10.1	0.006 ± 0.035	0.013 ± 0.038	40	2
2.39	5.5 ± 16.5	201.0 ± 10.2	-0.030 ± 0.035	0.026 ± 0.038	40	2
3.85	3.5 ± 10.1	195.1 ± 10.5	0.033 ± 0.039	0.009 ± 0.042	40	2
7.06	-12.2 ± 14.4	192.0 ± 19.1	0.004 ± 0.063	0.051 ± 0.071	40	2
-9.50	-4.8 ± 18.8	131.2 ± 26.0	-0.014 ± 0.090	0.006 ± 0.104	130	2
-6.05	26.3 ± 10.3	206.7 ± 13.1	-0.006 ± 0.045	0.019 ± 0.048	130	2
-3.31	54.1 ± 10.9	181.3 ± 10.9	-0.060 ± 0.039	0.045 ± 0.044	130	2
-1.85	40.7 ± 11.5	200.0 ± 9.1	-0.066 ± 0.032	0.010 ± 0.036	130	2
-0.64	-3.2 ± 9.6	225.8 ± 8.7	0.013 ± 0.030	-0.033 ± 0.035	130	2
0.57	4.9 ± 7.4	214.4 ± 7.8	0.016 ± 0.030	-0.033 ± 0.031	130	2
1.77	-22.0 ± 8.9	211.8 ± 8.5	-0.002 ± 0.033	-0.018 ± 0.033	130	2
3.24	-60.3 ± 9.1	185.7 ± 8.7	0.120 ± 0.032	0.027 ± 0.035	130	2
5.54	-25.9 ± 14.9	194.3 ± 10.9	0.011 ± 0.041	0.012 ± 0.043	130	2
8.34	-10.1 ± 13.1	169.3 ± 15.5	-0.026 ± 0.068	-0.019 ± 0.074	130	2
NGC 712						
-15.11	242.2 ± 18.9	62.4 ± 39.9	-0.024 ± 0.118	0.008 ± 0.102	95	1
-10.64	231.8 ± 10.5	81.7 ± 14.6	-0.084 ± 0.077	0.054 ± 0.118	95	1
-6.32	194.6 ± 13.7	132.7 ± 10.4	-0.055 ± 0.047	0.026 ± 0.058	95	1
-3.98	145.5 ± 7.4	163.5 ± 8.4	-0.048 ± 0.032	0.043 ± 0.037	95	1
-2.49	122.3 ± 7.0	174.8 ± 8.4	-0.071 ± 0.030	0.030 ± 0.035	95	1
-1.27	76.2 ± 6.9	206.8 ± 6.5	-0.078 ± 0.022	0.024 ± 0.024	95	1
-0.40	27.7 ± 7.2	208.6 ± 6.0	-0.062 ± 0.021	-0.002 ± 0.024	95	1
0.21	-7.7 ± 8.4	226.4 ± 6.8	-0.027 ± 0.020	0.031 ± 0.023	95	1
0.82	-47.9 ± 10.0	217.5 ± 6.2	0.039 ± 0.022	0.002 ± 0.024	95	1
1.69	-83.6 ± 7.2	187.9 ± 6.4	0.050 ± 0.022	0.048 ± 0.024	95	1
2.91	-122.6 ± 13.7	184.6 ± 7.9	0.051 ± 0.027	0.042 ± 0.031	95	1
4.40	-149.3 ± 6.7	159.9 ± 9.8	0.053 ± 0.032	0.097 ± 0.040	95	1
6.75	-181.4 ± 7.8	141.2 ± 10.7	0.063 ± 0.041	0.059 ± 0.054	95	1
11.25	-228.1 ± 8.9	110.1 ± 13.4	0.057 ± 0.063	0.042 ± 0.082	95	1
15.77	-220.0 ± 19.8	140.5 ± 26.4	0.045 ± 0.102	0.040 ± 0.129	95	1
-8.07	143.2 ± 13.1	112.6 ± 19.1	-0.020 ± 0.101	0.026 ± 0.126	125	2
-5.19	128.3 ± 8.3	133.1 ± 12.7	-0.075 ± 0.053	0.079 ± 0.066	125	2
-2.64	92.3 ± 6.9	173.9 ± 10.4	-0.028 ± 0.031	0.144 ± 0.036	125	2
-1.15	43.0 ± 6.0	201.7 ± 6.2	-0.059 ± 0.020	0.048 ± 0.021	125	2
-0.29	18.8 ± 5.5	211.7 ± 7.3	-0.024 ± 0.022	0.034 ± 0.027	125	2
0.32	-20.3 ± 5.4	219.6 ± 6.6	0.017 ± 0.022	0.015 ± 0.023	125	2

TABLE 6—Continued

<i>r</i> [arcsec]	<i>V</i> [km s ⁻¹]	σ [km s ⁻¹]	<i>H</i> ₃	<i>H</i> ₄	PA [°]	Run
1.19	-63.4 ± 8.3	204.1 ± 6.1	0.057 ± 0.020	0.049 ± 0.022	125	2
2.65	-97.8 ± 7.0	186.1 ± 8.8	0.057 ± 0.030	0.063 ± 0.033	125	2
5.24	-121.9 ± 15.6	151.7 ± 12.9	0.014 ± 0.044	0.110 ± 0.054	125	2
8.68	-122.0 ± 13.3	122.6 ± 17.1	0.050 ± 0.076	0.084 ± 0.086	125	2
-7.70	20.3 ± 19.0	150.1 ± 23.1	0.031 ± 0.083	0.071 ± 0.099	170	2
-4.77	6.5 ± 11.7	189.5 ± 15.6	0.038 ± 0.048	0.088 ± 0.052	170	2
-2.53	-6.4 ± 6.8	191.3 ± 8.8	0.014 ± 0.028	0.068 ± 0.032	170	2
-0.82	19.2 ± 5.4	200.3 ± 5.0	0.030 ± 0.017	0.023 ± 0.019	170	2
0.03	7.1 ± 5.2	217.6 ± 6.0	0.036 ± 0.020	-0.001 ± 0.023	170	2
0.88	-18.9 ± 5.4	220.1 ± 5.7	-0.001 ± 0.018	0.043 ± 0.019	170	2
2.57	-1.6 ± 7.9	164.3 ± 9.8	-0.020 ± 0.031	0.120 ± 0.039	170	2
4.82	-28.0 ± 16.5	134.6 ± 17.5	-0.010 ± 0.064	0.118 ± 0.074	170	2
8.18	2.0 ± 16.0	94.4 ± 20.0	0.049 ± 0.106	0.044 ± 0.148	170	2
NGC 759						
-8.36	-12.3 ± 13.6	176.9 ± 17.9	-0.010 ± 0.069	0.022 ± 0.077	11	1
-5.79	-27.5 ± 12.4	218.3 ± 15.1	-0.053 ± 0.045	0.034 ± 0.050	11	1
-3.56	-60.4 ± 9.5	202.7 ± 11.0	0.039 ± 0.029	0.096 ± 0.033	11	1
-1.86	-51.6 ± 8.9	222.5 ± 6.8	0.088 ± 0.021	0.033 ± 0.024	11	1
-1.00	-32.5 ± 7.2	235.0 ± 6.3	0.043 ± 0.018	0.032 ± 0.020	11	1
-0.39	-8.3 ± 8.4	239.3 ± 6.5	0.002 ± 0.018	0.051 ± 0.020	11	1
0.22	23.6 ± 10.5	236.1 ± 7.0	0.004 ± 0.017	0.067 ± 0.020	11	1
0.82	33.0 ± 11.7	234.2 ± 7.3	0.014 ± 0.020	0.045 ± 0.023	11	1
1.69	50.0 ± 11.5	224.4 ± 9.4	-0.022 ± 0.022	0.095 ± 0.024	11	1
3.15	49.4 ± 10.7	212.1 ± 8.3	-0.098 ± 0.026	0.033 ± 0.030	11	1
5.00	33.9 ± 11.5	215.2 ± 13.1	0.002 ± 0.044	0.027 ± 0.047	11	1
7.32	2.8 ± 14.1	206.0 ± 16.2	-0.026 ± 0.055	0.023 ± 0.061	11	1
-8.51	2.4 ± 16.2	220.1 ± 21.0	0.050 ± 0.061	0.020 ± 0.074	100	2
-5.35	21.7 ± 15.1	214.2 ± 21.5	-0.060 ± 0.057	0.109 ± 0.062	100	2
-3.08	23.1 ± 7.3	205.5 ± 11.1	-0.021 ± 0.031	0.137 ± 0.033	100	2
-1.40	-4.9 ± 6.1	215.3 ± 7.5	-0.029 ± 0.020	0.109 ± 0.022	100	2
-0.55	3.9 ± 4.9	207.3 ± 7.3	0.037 ± 0.020	0.086 ± 0.023	100	2
0.06	1.3 ± 5.1	210.3 ± 6.9	0.057 ± 0.021	0.049 ± 0.024	100	2
0.67	-1.6 ± 4.9	211.8 ± 7.4	0.047 ± 0.019	0.107 ± 0.022	100	2
1.53	-13.4 ± 8.4	213.0 ± 7.7	0.010 ± 0.020	0.099 ± 0.022	100	2
3.20	-2.0 ± 11.9	217.2 ± 8.6	0.031 ± 0.026	0.053 ± 0.028	100	2
5.45	5.4 ± 12.9	210.4 ± 16.0	-0.073 ± 0.048	0.005 ± 0.062	100	2
7.78	-36.2 ± 17.7	233.4 ± 17.5	-0.077 ± 0.058	-0.029 ± 0.067	100	2
-9.56	53.9 ± 24.9	196.2 ± 26.0	0.022 ± 0.084	0.024 ± 0.097	145	2
-6.87	6.7 ± 14.8	231.0 ± 15.2	0.017 ± 0.051	-0.006 ± 0.055	145	2
-4.79	-18.3 ± 13.0	248.4 ± 17.0	0.020 ± 0.037	0.083 ± 0.042	145	2
-2.92	-33.6 ± 9.1	223.1 ± 8.2	0.049 ± 0.025	0.030 ± 0.028	145	2
-1.47	-21.6 ± 6.6	242.0 ± 7.2	0.051 ± 0.017	0.073 ± 0.019	145	2
-0.61	-8.0 ± 5.5	238.8 ± 6.7	0.009 ± 0.019	0.031 ± 0.021	145	2
-0.00	-0.1 ± 5.8	228.1 ± 7.1	0.001 ± 0.019	0.065 ± 0.021	145	2
0.60	8.5 ± 5.7	234.4 ± 7.4	-0.020 ± 0.018	0.082 ± 0.021	145	2
1.47	26.9 ± 8.1	222.3 ± 7.1	0.008 ± 0.020	0.084 ± 0.022	145	2
2.93	27.6 ± 8.3	214.1 ± 9.4	0.012 ± 0.026	0.093 ± 0.030	145	2
4.78	60.3 ± 21.6	240.9 ± 18.3	-0.014 ± 0.043	0.158 ± 0.044	145	2
7.10	35.7 ± 16.8	205.7 ± 20.0	-0.004 ± 0.058	0.074 ± 0.057	145	2
9.81	67.3 ± 20.7	174.0 ± 28.2	-0.022 ± 0.102	0.034 ± 0.114	145	2
UGC 1308						
-9.41	-24.6 ± 20.1	146.9 ± 28.2	-0.025 ± 0.119	0.009 ± 0.148	28	1
-6.33	-31.9 ± 13.6	185.1 ± 16.8	0.034 ± 0.067	-0.000 ± 0.071	28	1
-3.77	-23.7 ± 9.7	185.0 ± 12.9	0.068 ± 0.045	0.034 ± 0.051	28	1

TABLE 6—*Continued*

r [arcsec]	V [km s $^{-1}$]	σ [km s $^{-1}$]	H_3	H_4	PA [$^{\circ}$]	Run
-2.30	-41.9 \pm 10.0	220.3 \pm 13.2	-0.002 \pm 0.037	0.063 \pm 0.039	28	1
-1.08	-1.7 \pm 9.6	203.4 \pm 12.0	-0.018 \pm 0.036	0.057 \pm 0.041	28	1
-0.20	6.2 \pm 11.2	215.6 \pm 11.3	-0.008 \pm 0.034	0.044 \pm 0.039	28	1
0.41	21.2 \pm 10.3	230.8 \pm 11.9	-0.016 \pm 0.034	0.037 \pm 0.040	28	1
1.30	21.4 \pm 8.0	193.6 \pm 11.1	-0.003 \pm 0.036	0.026 \pm 0.042	28	1
2.50	18.6 \pm 9.9	197.9 \pm 11.7	-0.071 \pm 0.042	-0.004 \pm 0.049	28	1
3.97	23.8 \pm 11.6	209.8 \pm 14.1	-0.052 \pm 0.048	0.013 \pm 0.054	28	1
7.20	0.4 \pm 18.2	188.7 \pm 21.5	-0.062 \pm 0.069	0.033 \pm 0.086	28	1
10.49	32.0 \pm 25.3	79.6 \pm 41.3	0.007 \pm 0.149	-0.003 \pm 0.154	28	1
-5.59	-5.3 \pm 29.9	224.8 \pm 32.7	0.050 \pm 0.092	0.017 \pm 0.108	28	2
-3.18	2.5 \pm 15.1	237.4 \pm 17.3	-0.022 \pm 0.052	0.017 \pm 0.058	28	2
-1.44	-21.7 \pm 14.5	219.6 \pm 17.8	-0.015 \pm 0.055	0.048 \pm 0.060	28	2
-0.26	12.8 \pm 11.0	202.5 \pm 14.4	-0.075 \pm 0.046	0.056 \pm 0.053	28	2
0.92	-17.5 \pm 14.5	206.4 \pm 19.3	-0.013 \pm 0.051	0.080 \pm 0.057	28	2
2.81	27.7 \pm 15.6	187.6 \pm 17.5	0.006 \pm 0.063	0.022 \pm 0.070	28	2
4.67	1.5 \pm 23.7	200.8 \pm 24.9	0.006 \pm 0.106	-0.059 \pm 0.099	28	2
-10.97	10.1 \pm 20.5	199.2 \pm 23.8	0.040 \pm 0.084	-0.004 \pm 0.094	120	2
-5.42	-16.7 \pm 10.2	192.4 \pm 13.4	-0.011 \pm 0.048	0.029 \pm 0.051	120	2
-2.88	-8.7 \pm 8.9	187.3 \pm 9.8	0.021 \pm 0.033	0.044 \pm 0.037	120	2
-1.42	5.3 \pm 6.5	204.8 \pm 8.4	0.063 \pm 0.026	0.044 \pm 0.031	120	2
-0.54	1.3 \pm 6.4	220.4 \pm 8.6	0.012 \pm 0.024	0.057 \pm 0.027	120	2
0.07	6.5 \pm 6.4	222.0 \pm 7.9	-0.078 \pm 0.024	0.028 \pm 0.027	120	2
0.67	1.7 \pm 10.4	238.3 \pm 8.8	-0.009 \pm 0.024	0.039 \pm 0.028	120	2
1.56	-8.8 \pm 7.6	209.8 \pm 9.2	0.010 \pm 0.025	0.104 \pm 0.027	120	2
2.77	2.0 \pm 10.7	193.3 \pm 9.0	-0.004 \pm 0.035	0.001 \pm 0.038	120	2
4.25	-1.0 \pm 9.3	213.9 \pm 13.3	0.023 \pm 0.037	0.088 \pm 0.038	120	2
6.00	8.7 \pm 9.8	171.0 \pm 13.8	0.009 \pm 0.048	0.053 \pm 0.056	120	2

TABLE 7
IONIZED-GAS KINEMATICS OF THE SAMPLE GALAXIES

r [arcsec]	V [km s $^{-1}$]	σ [km s $^{-1}$]	PA [$^{\circ}$]	Run
IC 171				
-7.34	138.4 \pm 14.8	0.0 \pm 24.9	0	4
-6.11	146.2 \pm 15.4	75.4 \pm 21.0	0	4
-4.88	123.1 \pm 23.5	88.6 \pm 29.3	0	4
-3.65	85.8 \pm 16.2	78.6 \pm 21.6	0	4
-2.42	54.8 \pm 13.7	82.1 \pm 18.3	0	4
-1.19	12.4 \pm 12.1	93.4 \pm 16.0	0	4
0.04	-16.9 \pm 32.8	104.0 \pm 38.6	0	4
1.27	-36.9 \pm 30.4	81.8 \pm 38.5	0	4
2.50	-42.2 \pm 21.3	76.1 \pm 28.2	0	4
3.73	-103.2 \pm 10.1	34.8 \pm 21.4	0	4
4.96	-103.0 \pm 8.8	52.3 \pm 15.2	0	4
6.19	-112.3 \pm 13.7	56.9 \pm 21.2	0	4
7.42	-146.3 \pm 12.5	24.9 \pm 33.7	0	4
NGC 703				
-2.46	-125.2 \pm 31.3	137.7 \pm 33.5	0	4
-1.23	-75.5 \pm 20.4	223.6 \pm 18.1	0	4
0.00	30.0 \pm 66.0	259.6 \pm 53.7	0	4
1.23	90.4 \pm 36.3	176.2 \pm 62.0	0	4
2.46	80.2 \pm 25.1	0.0 \pm 114.0	0	4
NGC 708				
-4.92	-161.3 \pm 18.5	125.2 \pm 21.3	0	4
-3.69	-162.5 \pm 6.9	116.8 \pm 10.3	0	4
-2.87	-141.1 \pm 3.6	120.2 \pm 7.9	0	4
-1.23	-96.7 \pm 3.6	144.6 \pm 7.8	0	4
0.00	1.6 \pm 4.3	189.8 \pm 7.9	0	4
1.23	88.7 \pm 2.8	146.7 \pm 7.5	0	4
2.46	145.7 \pm 3.3	103.6 \pm 7.8	0	4
3.69	191.8 \pm 2.7	85.9 \pm 7.6	0	4
4.92	218.2 \pm 4.0	78.9 \pm 8.5	0	4
6.15	257.5 \pm 5.4	78.9 \pm 9.7	0	4
7.38	267.4 \pm 4.3	73.6 \pm 8.9	0	4
8.61	284.1 \pm 12.2	89.4 \pm 16.2	0	4
20.09	302.6 \pm 15.1	48.0 \pm 25.3	0	4
-18.86	-261.9 \pm 15.2	56.8 \pm 23.3	40	4
-17.22	-263.2 \pm 10.5	44.0 \pm 19.2	40	4
-15.99	-251.4 \pm 12.0	81.0 \pm 16.4	40	4
-14.76	-220.5 \pm 11.1	89.7 \pm 15.1	40	4
-13.53	-193.9 \pm 6.3	86.2 \pm 10.3	40	4
-12.30	-193.1 \pm 4.2	84.4 \pm 8.6	40	4
-11.07	-183.7 \pm 3.9	87.8 \pm 8.3	40	4
-9.84	-180.7 \pm 4.0	91.3 \pm 8.4	40	4
-8.61	-169.5 \pm 4.1	88.0 \pm 8.4	40	4
-7.38	-152.6 \pm 3.5	70.5 \pm 8.2	40	4
-6.15	-158.5 \pm 3.3	81.9 \pm 8.0	40	4
-4.92	-158.1 \pm 4.2	91.1 \pm 8.5	40	4
-3.69	-126.7 \pm 6.9	129.3 \pm 10.2	40	4
-2.46	-79.8 \pm 5.9	135.7 \pm 9.3	40	4
-1.23	-45.8 \pm 3.8	160.2 \pm 7.8	40	4
0.00	0.0 \pm 2.7	172.1 \pm 7.3	40	4
1.23	48.4 \pm 4.0	156.2 \pm 7.9	40	4
2.46	105.9 \pm 6.5	127.6 \pm 9.9	40	4

TABLE 7—*Continued*

<i>r</i> [arcsec]	<i>V</i> [km s ⁻¹]	σ [km s ⁻¹]	PA [°]	Run
3.69	162.0 ± 8.6	114.0 ± 11.8	40	4
5.33	192.6 ± 20.3	131.9 ± 23.0	40	4
-6.77	-190.9 ± 15.6	114.4 ± 18.8	130	4
-5.54	-178.0 ± 8.0	106.8 ± 11.4	130	4
-4.31	-163.6 ± 6.9	130.5 ± 10.1	130	4
-3.08	-114.8 ± 6.4	139.5 ± 9.6	130	4
-1.85	-79.2 ± 5.1	141.4 ± 8.7	130	4
-0.62	-42.1 ± 3.9	153.8 ± 7.9	130	4
0.61	52.7 ± 3.4	177.9 ± 7.5	130	4
1.84	154.3 ± 2.9	161.8 ± 7.4	130	4
3.07	187.5 ± 4.5	119.0 ± 8.5	130	4
4.30	179.0 ± 8.8	108.5 ± 12.1	130	4
5.53	177.1 ± 8.6	79.9 ± 12.8	130	4
6.76	186.6 ± 5.8	90.0 ± 9.8	130	4
7.99	194.0 ± 7.0	83.0 ± 11.1	130	4
9.22	212.8 ± 12.5	122.6 ± 15.3	130	4
14.55	290.0 ± 11.9	70.5 ± 17.2	130	4
16.60	286.6 ± 27.3	60.1 ± 39.4	130	4
NGC 712				
-5.29	-23.8 ± 21.3	76.6 ± 28.1	0	4
-2.42	-40.0 ± 12.0	98.0 ± 15.6	0	4
-1.19	-10.7 ± 41.2	154.9 ± 41.5	0	4
0.04	1.6 ± 22.8	167.5 ± 118.1	0	4
1.27	33.1 ± 40.2	106.2 ± 46.5	0	4
2.50	19.4 ± 16.9	70.7 ± 23.3	0	4
5.37	20.5 ± 30.8	28.5 ± 73.0	0	4
NGC 759				
-5.41	-152.7 ± 6.1	55.6 ± 11.3	0	4
-3.77	-163.3 ± 2.2	46.7 ± 7.8	0	4
-2.54	-153.3 ± 2.3	57.7 ± 7.6	0	4
-1.31	-112.9 ± 4.6	111.8 ± 8.6	0	4
-0.08	4.4 ± 10.8	172.2 ± 12.2	0	4
1.15	122.4 ± 4.0	104.1 ± 8.3	0	4
2.38	148.7 ± 3.7	64.4 ± 8.5	0	4
3.61	146.1 ± 2.5	51.1 ± 7.9	0	4
5.66	160.4 ± 5.3	53.9 ± 10.5	0	4
-5.45	52.3 ± 4.1	53.6 ± 9.2	100	4
-3.81	49.8 ± 2.4	58.6 ± 7.7	100	4
-2.58	48.9 ± 5.5	99.6 ± 9.4	100	4
-1.35	40.8 ± 5.4	137.8 ± 8.9	100	4
-0.12	4.8 ± 9.9	161.8 ± 11.8	100	4
1.11	-28.7 ± 6.3	127.0 ± 9.6	100	4
2.34	-49.1 ± 2.9	83.5 ± 7.7	100	4
3.57	-56.7 ± 2.8	47.1 ± 8.3	100	4
5.21	-62.1 ± 6.8	37.2 ± 14.8	100	4
-5.49	-84.4 ± 7.4	66.1 ± 12.2	145	4
-3.85	-75.5 ± 4.7	86.5 ± 8.9	145	4
-2.62	-66.6 ± 4.4	115.1 ± 8.5	145	4
-1.39	-38.1 ± 3.9	152.1 ± 7.9	145	4
-0.16	-2.2 ± 9.0	164.7 ± 11.0	145	4
1.07	57.2 ± 7.8	133.3 ± 10.8	145	4
2.30	70.3 ± 3.1	93.6 ± 7.8	145	4
3.53	73.5 ± 3.4	72.0 ± 8.2	145	4
5.17	65.9 ± 5.9	64.3 ± 10.6	145	4

TABLE 7—*Continued*

<i>r</i> [arcsec]	<i>V</i> [km s ⁻¹]	σ [km s ⁻¹]	PA [°]	Run
UGC 1308				
-4.02	149.7 ± 46.7	66.2 ± 63.9	0	4
-1.15	143.2 ± 24.4	130.7 ± 27.1	0	4
0.08	0.0 ± 78.0	180.1 ± 73.8	0	4
1.31	-71.2 ± 41.9	87.1 ± 51.5	0	4
2.54	-74.2 ± 39.3	48.5 ± 63.4	0	4

TABLE 8
LINE-STRENGTH INDICES OF THE SAMPLE GALAXIES

<i>r</i> [arcsec]	H β [Å]	[MgFe] [Å]	$\langle \text{Fe} \rangle$ [Å]	Mgb [Å]	Mg ₂ [mag]	PA [°]	Run
IC 171							
-11.71	2.571 ± 0.518	3.004 ± 0.562	2.086 ± 0.566	4.326 ± 0.445	0.264 ± 0.014	10	2
-8.47	1.410 ± 0.294	3.287 ± 0.376	2.603 ± 0.352	4.151 ± 0.388	0.247 ± 0.010	10	2
-5.27	1.754 ± 0.223	3.394 ± 0.281	2.635 ± 0.263	4.371 ± 0.289	0.256 ± 0.007	10	2
-2.84	1.804 ± 0.176	3.386 ± 0.157	2.632 ± 0.149	4.357 ± 0.159	0.268 ± 0.004	10	2
-1.08	1.792 ± 0.145	3.367 ± 0.119	2.634 ± 0.111	4.303 ± 0.123	0.266 ± 0.003	10	2
-0.23	2.322 ± 0.136	2.908 ± 0.130	2.157 ± 0.126	3.920 ± 0.122	0.250 ± 0.003	10	2
0.38	2.585 ± 0.148	3.056 ± 0.168	2.404 ± 0.167	3.884 ± 0.157	0.269 ± 0.004	10	2
0.98	2.409 ± 0.259	3.342 ± 0.196	2.770 ± 0.195	4.031 ± 0.191	0.242 ± 0.005	10	2
2.12	2.241 ± 0.242	3.471 ± 0.244	2.819 ± 0.230	4.273 ± 0.253	0.253 ± 0.006	10	2
3.94	1.329 ± 0.216	3.000 ± 0.301	2.117 ± 0.277	4.249 ± 0.297	0.292 ± 0.008	10	2
6.29	2.011 ± 0.252	2.733 ± 0.343	2.097 ± 0.325	3.561 ± 0.344	0.263 ± 0.009	10	2
11.64	1.204 ± 0.421	2.995 ± 0.542	2.151 ± 0.505	4.170 ± 0.529	0.260 ± 0.014	10	2
-20.54	...	3.085 ± 0.785	2.445 ± 0.817	3.892 ± 0.680	0.207 ± 0.019	110	1
-12.32	1.382 ± 0.493	2.851 ± 0.470	2.502 ± 0.434	3.248 ± 0.508	0.243 ± 0.012	110	1
-9.11	1.790 ± 0.420	3.225 ± 0.402	2.883 ± 0.380	3.608 ± 0.425	0.236 ± 0.010	110	1
-6.31	1.350 ± 0.195	3.049 ± 0.238	2.404 ± 0.235	3.866 ± 0.225	0.243 ± 0.006	110	1
-3.98	1.279 ± 0.157	3.442 ± 0.185	2.962 ± 0.180	4.000 ± 0.187	0.249 ± 0.005	110	1
-2.49	1.494 ± 0.149	3.314 ± 0.179	2.702 ± 0.176	4.066 ± 0.174	0.258 ± 0.005	110	1
-1.28	1.687 ± 0.114	3.309 ± 0.138	2.779 ± 0.136	3.941 ± 0.137	0.263 ± 0.004	110	1
-0.39	1.834 ± 0.124	3.564 ± 0.152	2.988 ± 0.147	4.251 ± 0.153	0.267 ± 0.004	110	1
0.21	1.997 ± 0.111	3.635 ± 0.134	3.155 ± 0.130	4.187 ± 0.136	0.259 ± 0.003	110	1
1.10	1.527 ± 0.108	3.472 ± 0.128	3.046 ± 0.124	3.957 ± 0.131	0.258 ± 0.003	110	1
2.31	1.518 ± 0.152	3.068 ± 0.170	2.772 ± 0.163	3.396 ± 0.178	0.251 ± 0.005	110	1
3.80	1.288 ± 0.167	3.257 ± 0.192	2.841 ± 0.184	3.734 ± 0.198	0.253 ± 0.005	110	1
5.89	1.822 ± 0.185	3.408 ± 0.229	2.692 ± 0.219	4.314 ± 0.229	0.253 ± 0.006	110	1
9.32	1.326 ± 0.217	3.256 ± 0.264	2.752 ± 0.256	3.852 ± 0.268	0.243 ± 0.007	110	1
14.21	...	3.320 ± 0.500	3.118 ± 0.529	3.535 ± 0.464	0.238 ± 0.014	110	1
-13.85	...	3.014 ± 1.013	2.351 ± 0.939	3.862 ± 1.053	0.248 ± 0.024	110	2
-8.82	1.454 ± 0.595	2.830 ± 0.675	2.164 ± 0.629	3.700 ± 0.690	0.258 ± 0.016	110	2
-5.36	1.637 ± 0.339	2.853 ± 0.275	2.390 ± 0.284	3.406 ± 0.253	0.239 ± 0.010	110	2
-2.80	1.708 ± 0.265	3.082 ± 0.209	2.642 ± 0.215	3.594 ± 0.196	0.247 ± 0.007	110	2
-1.32	1.681 ± 0.188	3.128 ± 0.148	2.488 ± 0.149	3.931 ± 0.137	0.265 ± 0.005	110	2
-0.46	1.451 ± 0.174	2.996 ± 0.147	2.348 ± 0.145	3.822 ± 0.140	0.267 ± 0.005	110	2
0.15	1.786 ± 0.178	3.044 ± 0.164	2.354 ± 0.164	3.935 ± 0.152	0.267 ± 0.006	110	2
0.75	2.245 ± 0.189	3.057 ± 0.197	2.368 ± 0.198	3.947 ± 0.179	0.274 ± 0.006	110	2
1.62	1.985 ± 0.229	3.078 ± 0.242	2.556 ± 0.248	3.705 ± 0.224	0.277 ± 0.008	110	2
3.11	1.616 ± 0.267	3.158 ± 0.278	2.480 ± 0.278	4.020 ± 0.258	0.269 ± 0.009	110	2
5.71	1.310 ± 0.275	3.186 ± 0.322	2.259 ± 0.312	4.492 ± 0.287	0.264 ± 0.010	110	2
8.86	0.765 ± 0.496	3.119 ± 0.533	2.696 ± 0.514	3.610 ± 0.546	0.263 ± 0.016	110	2
12.26	...	3.011 ± 0.761	2.474 ± 0.730	3.663 ± 0.772	0.261 ± 0.023	110	2
-12.15	1.801 ± 0.469	2.619 ± 0.533	2.153 ± 0.556	3.185 ± 0.474	0.255 ± 0.013	145	2
-7.28	2.359 ± 0.332	3.100 ± 0.367	2.651 ± 0.386	3.625 ± 0.331	0.257 ± 0.009	145	2
-4.93	1.495 ± 0.233	2.561 ± 0.284	1.818 ± 0.285	3.609 ± 0.236	0.250 ± 0.006	145	2
-2.71	1.123 ± 0.160	2.981 ± 0.156	2.272 ± 0.157	3.911 ± 0.141	0.248 ± 0.005	145	2
-1.00	1.607 ± 0.151	3.161 ± 0.137	2.516 ± 0.138	3.971 ± 0.128	0.246 ± 0.004	145	2
-0.14	2.296 ± 0.122	3.014 ± 0.127	2.222 ± 0.125	4.087 ± 0.115	0.252 ± 0.004	145	2
0.46	1.909 ± 0.120	3.114 ± 0.141	2.291 ± 0.138	4.231 ± 0.128	0.271 ± 0.004	145	2
1.32	2.074 ± 0.133	3.273 ± 0.162	2.648 ± 0.164	4.046 ± 0.150	0.279 ± 0.005	145	2
2.78	1.600 ± 0.139	3.365 ± 0.176	2.687 ± 0.179	4.214 ± 0.159	0.273 ± 0.005	145	2
4.66	1.341 ± 0.155	3.486 ± 0.202	2.813 ± 0.215	4.320 ± 0.171	0.278 ± 0.004	145	2
6.73	1.879 ± 0.159	3.397 ± 0.217	2.542 ± 0.225	4.541 ± 0.177	0.262 ± 0.005	145	2
10.30	2.012 ± 0.291	3.292 ± 0.389	2.488 ± 0.396	4.355 ± 0.337	0.259 ± 0.006	145	2
16.98	1.898 ± 0.455	3.043 ± 0.523	2.347 ± 0.530	3.944 ± 0.465	0.268 ± 0.013	145	2

NGC 679

TABLE 8—Continued

<i>r</i> [arcsec]	H β [Å]	[MgFe] [Å]	$\langle \text{Fe} \rangle$ [Å]	Mgb [Å]	Mg ₂ [mag]	PA [°]	Run
-14.75	2.299 ± 0.478	2.367 ± 0.719	1.546 ± 0.613	3.623 ± 0.766	0.248 ± 0.021	0	1
-10.93	1.517 ± 0.373	2.877 ± 0.556	1.831 ± 0.469	4.522 ± 0.588	0.270 ± 0.016	0	1
-8.13	1.442 ± 0.260	3.652 ± 0.299	2.543 ± 0.292	5.244 ± 0.257	0.271 ± 0.009	0	1
-5.78	1.109 ± 0.227	3.332 ± 0.209	2.327 ± 0.203	4.770 ± 0.183	0.262 ± 0.006	0	1
-3.94	1.751 ± 0.214	3.608 ± 0.122	2.601 ± 0.118	5.006 ± 0.111	0.275 ± 0.003	0	1
-2.48	1.513 ± 0.198	3.456 ± 0.101	2.579 ± 0.098	4.632 ± 0.094	0.278 ± 0.003	0	1
-1.61	1.591 ± 0.188	3.604 ± 0.090	2.690 ± 0.087	4.828 ± 0.084	0.289 ± 0.002	0	1
-1.01	1.452 ± 0.182	3.579 ± 0.083	2.670 ± 0.082	4.798 ± 0.076	0.285 ± 0.002	0	1
-0.40	1.807 ± 0.177	3.602 ± 0.084	2.666 ± 0.083	4.867 ± 0.076	0.281 ± 0.002	0	1
0.21	1.989 ± 0.113	3.631 ± 0.112	2.760 ± 0.103	4.776 ± 0.117	0.294 ± 0.003	0	1
0.81	2.081 ± 0.249	3.491 ± 0.088	2.678 ± 0.085	4.550 ± 0.087	0.262 ± 0.003	0	1
1.68	2.208 ± 0.258	3.471 ± 0.095	2.559 ± 0.098	4.706 ± 0.078	0.263 ± 0.003	0	1
3.14	2.491 ± 0.300	3.470 ± 0.110	2.487 ± 0.108	4.842 ± 0.098	0.256 ± 0.003	0	1
4.98	1.677 ± 0.270	3.415 ± 0.256	2.515 ± 0.260	4.635 ± 0.217	0.281 ± 0.007	0	1
7.32	1.448 ± 0.223	3.243 ± 0.314	2.374 ± 0.314	4.430 ± 0.272	0.294 ± 0.009	0	1
10.12	1.294 ± 0.402	2.966 ± 0.587	2.067 ± 0.530	4.257 ± 0.591	0.260 ± 0.015	0	1
13.54	0.960 ± 0.487	2.589 ± 0.721	1.819 ± 0.646	3.684 ± 0.746	0.279 ± 0.019	0	1
-6.05	2.218 ± 0.544	3.253 ± 0.513	2.558 ± 0.463	4.138 ± 0.555	0.267 ± 0.023	0	2
-2.99	2.311 ± 0.319	3.442 ± 0.321	2.406 ± 0.328	4.923 ± 0.246	0.282 ± 0.012	0	2
-1.54	2.090 ± 0.318	3.380 ± 0.313	2.538 ± 0.331	4.502 ± 0.247	0.274 ± 0.007	0	2
-0.66	2.116 ± 0.260	3.483 ± 0.257	2.549 ± 0.284	4.759 ± 0.174	0.292 ± 0.005	0	2
-0.06	2.051 ± 0.310	3.184 ± 0.309	2.221 ± 0.310	4.566 ± 0.250	0.290 ± 0.007	0	2
0.55	2.312 ± 0.318	3.499 ± 0.307	2.731 ± 0.330	4.483 ± 0.245	0.297 ± 0.007	0	2
1.43	2.458 ± 0.326	3.803 ± 0.307	3.022 ± 0.336	4.785 ± 0.242	0.283 ± 0.008	0	2
2.63	2.458 ± 0.377	3.550 ± 0.371	2.683 ± 0.387	4.696 ± 0.306	0.231 ± 0.014	0	2
4.33	2.224 ± 0.415	3.865 ± 0.442	3.042 ± 0.435	4.911 ± 0.419	0.304 ± 0.012	0	2
7.41	2.150 ± 0.578	3.923 ± 0.523	3.114 ± 0.484	4.941 ± 0.550	0.282 ± 0.025	0	2
-10.17	1.553 ± 0.504	2.794 ± 0.515	1.940 ± 0.474	4.024 ± 0.500	0.243 ± 0.012	90	2
-6.60	1.679 ± 0.332	3.278 ± 0.360	2.482 ± 0.353	4.328 ± 0.337	0.247 ± 0.008	90	2
-3.50	1.588 ± 0.168	3.505 ± 0.163	2.645 ± 0.141	4.645 ± 0.184	0.277 ± 0.005	90	2
-1.82	1.609 ± 0.171	3.661 ± 0.168	2.830 ± 0.148	4.735 ± 0.187	0.294 ± 0.005	90	2
-0.96	1.678 ± 0.169	3.679 ± 0.162	2.724 ± 0.145	4.968 ± 0.175	0.295 ± 0.004	90	2
-0.36	1.774 ± 0.175	3.576 ± 0.171	2.675 ± 0.154	4.780 ± 0.182	0.285 ± 0.004	90	2
0.25	1.797 ± 0.190	3.470 ± 0.189	2.650 ± 0.172	4.545 ± 0.201	0.281 ± 0.005	90	2
0.85	1.735 ± 0.163	3.583 ± 0.176	2.696 ± 0.160	4.761 ± 0.186	0.289 ± 0.005	90	2
1.71	1.582 ± 0.149	3.615 ± 0.170	2.694 ± 0.155	4.851 ± 0.179	0.298 ± 0.004	90	2
3.39	1.751 ± 0.165	3.517 ± 0.183	2.667 ± 0.167	4.638 ± 0.192	0.289 ± 0.005	90	2
6.49	2.129 ± 0.336	3.097 ± 0.357	2.369 ± 0.328	4.050 ± 0.374	0.298 ± 0.009	90	2
10.08	1.342 ± 0.453	3.184 ± 0.476	2.632 ± 0.452	3.850 ± 0.492	0.279 ± 0.012	90	2
-9.47	1.102 ± 0.501	3.111 ± 0.474	2.287 ± 0.437	4.231 ± 0.483	0.272 ± 0.012	135	2
-5.65	1.302 ± 0.304	3.412 ± 0.289	2.407 ± 0.262	4.837 ± 0.293	0.293 ± 0.007	135	2
-2.95	1.692 ± 0.171	3.411 ± 0.205	2.478 ± 0.203	4.695 ± 0.180	0.283 ± 0.004	135	2
-1.49	1.877 ± 0.161	3.426 ± 0.185	2.560 ± 0.185	4.586 ± 0.162	0.286 ± 0.004	135	2
-0.63	1.485 ± 0.134	3.565 ± 0.153	2.751 ± 0.155	4.620 ± 0.136	0.287 ± 0.003	135	2
-0.02	1.545 ± 0.103	3.544 ± 0.121	2.659 ± 0.121	4.724 ± 0.107	0.282 ± 0.002	135	2
0.58	1.845 ± 0.092	3.394 ± 0.111	2.539 ± 0.112	4.535 ± 0.098	0.284 ± 0.002	135	2
1.19	1.889 ± 0.091	3.410 ± 0.111	2.574 ± 0.110	4.517 ± 0.100	0.293 ± 0.002	135	2
1.80	1.548 ± 0.097	3.424 ± 0.126	2.540 ± 0.123	4.615 ± 0.114	0.307 ± 0.003	135	2
2.66	1.647 ± 0.108	3.548 ± 0.144	2.723 ± 0.145	4.623 ± 0.131	0.307 ± 0.003	135	2
4.12	1.525 ± 0.130	3.513 ± 0.171	2.710 ± 0.170	4.554 ± 0.158	0.302 ± 0.004	135	2
5.96	1.546 ± 0.214	3.589 ± 0.246	2.741 ± 0.228	4.700 ± 0.254	0.301 ± 0.007	135	2
8.53	2.180 ± 0.302	3.404 ± 0.348	2.474 ± 0.318	4.683 ± 0.356	0.284 ± 0.010	135	2
NGC 687							
-9.77	1.116 ± 0.485	3.473 ± 0.647	2.648 ± 0.667	4.556 ± 0.550	0.255 ± 0.015	0	1
-7.32	1.917 ± 0.283	2.968 ± 0.359	2.081 ± 0.350	4.232 ± 0.314	0.251 ± 0.009	0	1

TABLE 8—Continued

<i>r</i> [arcsec]	H β [Å]	[MgFe] [Å]	$\langle \text{Fe} \rangle$ [Å]	Mgb [Å]	Mg ₂ [mag]	PA [°]	Run
-4.99	2.161 ± 0.220	3.329 ± 0.266	2.750 ± 0.272	4.031 ± 0.247	0.257 ± 0.007	0	1
-2.76	1.898 ± 0.124	3.333 ± 0.182	2.367 ± 0.173	4.692 ± 0.170	0.274 ± 0.004	0	1
-1.67	1.593 ± 0.092	3.329 ± 0.134	2.386 ± 0.128	4.645 ± 0.125	0.297 ± 0.003	0	1
-0.82	1.633 ± 0.083	3.508 ± 0.108	2.612 ± 0.104	4.713 ± 0.104	0.307 ± 0.003	0	1
-0.21	1.538 ± 0.078	3.540 ± 0.099	2.598 ± 0.095	4.824 ± 0.095	0.298 ± 0.002	0	1
0.39	1.443 ± 0.085	3.503 ± 0.106	2.630 ± 0.102	4.664 ± 0.101	0.291 ± 0.003	0	1
1.25	1.768 ± 0.104	3.298 ± 0.127	2.422 ± 0.122	4.490 ± 0.120	0.290 ± 0.003	0	1
2.71	1.571 ± 0.135	3.153 ± 0.169	2.381 ± 0.165	4.175 ± 0.159	0.260 ± 0.004	0	1
4.57	1.783 ± 0.219	3.295 ± 0.231	2.617 ± 0.247	4.148 ± 0.191	0.246 ± 0.006	0	1
6.89	2.014 ± 0.296	3.213 ± 0.312	2.488 ± 0.333	4.148 ± 0.251	0.236 ± 0.008	0	1
-9.43	1.694 ± 0.575	3.107 ± 0.632	2.337 ± 0.641	4.131 ± 0.548	0.219 ± 0.014	20	2
-6.73	1.012 ± 0.363	3.110 ± 0.338	2.349 ± 0.331	4.117 ± 0.316	0.234 ± 0.009	20	2
-3.60	1.814 ± 0.159	3.124 ± 0.174	2.388 ± 0.169	4.086 ± 0.166	0.243 ± 0.004	20	2
-1.70	1.738 ± 0.127	3.573 ± 0.135	2.752 ± 0.132	4.637 ± 0.128	0.267 ± 0.003	20	2
-0.85	1.714 ± 0.101	3.420 ± 0.109	2.564 ± 0.106	4.563 ± 0.103	0.276 ± 0.003	20	2
-0.24	1.754 ± 0.116	3.462 ± 0.130	2.679 ± 0.127	4.474 ± 0.124	0.284 ± 0.003	20	2
0.36	1.663 ± 0.116	3.397 ± 0.140	2.608 ± 0.137	4.425 ± 0.134	0.290 ± 0.003	20	2
0.97	1.460 ± 0.110	3.569 ± 0.137	2.762 ± 0.134	4.611 ± 0.131	0.307 ± 0.003	20	2
1.82	1.492 ± 0.135	3.434 ± 0.167	2.605 ± 0.162	4.529 ± 0.159	0.299 ± 0.004	20	2
3.73	1.672 ± 0.179	3.263 ± 0.209	2.457 ± 0.203	4.334 ± 0.197	0.279 ± 0.005	20	2
7.08	1.771 ± 0.307	2.632 ± 0.347	1.732 ± 0.324	4.001 ± 0.309	0.253 ± 0.010	20	2
-12.03	1.012 ± 0.385	3.236 ± 0.460	2.952 ± 0.506	3.547 ± 0.399	0.223 ± 0.014	110	2
-6.97	1.075 ± 0.235	2.898 ± 0.282	2.153 ± 0.291	3.900 ± 0.233	0.256 ± 0.008	110	2
-3.83	1.968 ± 0.207	3.372 ± 0.179	2.519 ± 0.176	4.512 ± 0.162	0.263 ± 0.005	110	2
-1.90	1.845 ± 0.133	3.598 ± 0.110	2.775 ± 0.110	4.664 ± 0.101	0.291 ± 0.003	110	2
-1.05	1.862 ± 0.128	3.715 ± 0.105	2.874 ± 0.104	4.801 ± 0.098	0.309 ± 0.003	110	2
-0.44	1.877 ± 0.177	3.562 ± 0.145	2.758 ± 0.141	4.599 ± 0.140	0.318 ± 0.004	110	2
0.16	1.860 ± 0.204	3.503 ± 0.172	2.766 ± 0.167	4.437 ± 0.166	0.318 ± 0.005	110	2
0.77	1.500 ± 0.153	3.657 ± 0.136	2.947 ± 0.134	4.537 ± 0.130	0.324 ± 0.004	110	2
1.62	1.372 ± 0.158	3.455 ± 0.146	2.638 ± 0.142	4.523 ± 0.139	0.313 ± 0.004	110	2
3.54	1.585 ± 0.188	3.061 ± 0.170	2.297 ± 0.162	4.079 ± 0.166	0.287 ± 0.005	110	2
6.66	1.902 ± 0.243	2.807 ± 0.272	2.256 ± 0.266	3.493 ± 0.266	0.277 ± 0.009	110	2
12.25	...	3.172 ± 0.488	2.354 ± 0.469	4.273 ± 0.464	0.287 ± 0.015	110	2
NGC 703							
-7.84	0.691 ± 0.558	2.526 ± 0.531	1.529 ± 0.489	4.172 ± 0.420	0.250 ± 0.012	0	2
-5.12	1.881 ± 0.319	3.051 ± 0.275	2.376 ± 0.282	3.917 ± 0.241	0.237 ± 0.007	0	2
-2.68	2.192 ± 0.239	3.091 ± 0.223	2.156 ± 0.212	4.431 ± 0.204	0.287 ± 0.006	0	2
-1.22	1.306 ± 0.167	3.502 ± 0.150	2.417 ± 0.142	5.074 ± 0.136	0.313 ± 0.004	0	2
-0.35	1.575 ± 0.168	3.619 ± 0.165	2.544 ± 0.159	5.149 ± 0.149	0.313 ± 0.004	0	2
0.51	1.440 ± 0.157	3.561 ± 0.159	2.623 ± 0.156	4.834 ± 0.146	0.303 ± 0.004	0	2
1.93	1.194 ± 0.197	3.488 ± 0.195	2.536 ± 0.187	4.798 ± 0.182	0.297 ± 0.005	0	2
3.79	2.109 ± 0.360	3.003 ± 0.347	2.362 ± 0.355	3.818 ± 0.309	0.269 ± 0.008	0	2
7.44	1.391 ± 0.640	2.383 ± 0.683	1.267 ± 0.579	4.483 ± 0.524	0.261 ± 0.015	0	2
-8.96	1.213 ± 0.425	3.056 ± 0.506	2.155 ± 0.498	4.332 ± 0.434	0.236 ± 0.014	45	1
-5.38	2.239 ± 0.210	3.009 ± 0.243	2.105 ± 0.243	4.299 ± 0.197	0.254 ± 0.005	45	1
-2.32	1.999 ± 0.138	3.083 ± 0.165	2.098 ± 0.164	4.531 ± 0.132	0.263 ± 0.003	45	1
-0.88	1.897 ± 0.111	3.562 ± 0.130	2.551 ± 0.132	4.973 ± 0.106	0.296 ± 0.003	45	1
-0.01	1.332 ± 0.110	3.787 ± 0.141	2.750 ± 0.144	5.215 ± 0.115	0.307 ± 0.003	45	1
0.85	1.707 ± 0.099	3.431 ± 0.125	2.470 ± 0.126	4.765 ± 0.104	0.280 ± 0.003	45	1
2.30	2.173 ± 0.141	3.112 ± 0.173	2.169 ± 0.171	4.465 ± 0.144	0.274 ± 0.004	45	1
5.49	1.066 ± 0.192	2.974 ± 0.233	2.188 ± 0.236	4.043 ± 0.197	0.243 ± 0.005	45	1
9.18	1.335 ± 0.396	2.544 ± 0.482	1.645 ± 0.427	3.934 ± 0.472	0.235 ± 0.012	45	1
-8.33	0.667 ± 0.655	2.852 ± 0.659	1.842 ± 0.655	4.416 ± 0.473	0.220 ± 0.019	135	2
-5.53	1.463 ± 0.360	3.203 ± 0.520	2.087 ± 0.481	4.917 ± 0.464	0.247 ± 0.013	135	2
-2.71	0.770 ± 0.171	3.247 ± 0.188	2.284 ± 0.181	4.614 ± 0.169	0.240 ± 0.005	135	2
-1.00	1.432 ± 0.149	3.785 ± 0.164	2.801 ± 0.161	5.114 ± 0.151	0.288 ± 0.004	135	2

TABLE 8—Continued

<i>r</i> [arcsec]	H β [Å]	[MgFe] [Å]	$\langle \text{Fe} \rangle$ [Å]	Mgb [Å]	Mg ₂ [mag]	PA [°]	Run
-0.16	1.143 ± 0.128	3.594 ± 0.151	2.567 ± 0.147	5.031 ± 0.137	0.285 ± 0.004	135	2
0.44	1.204 ± 0.116	3.597 ± 0.153	2.831 ± 0.153	4.570 ± 0.141	0.285 ± 0.004	135	2
1.29	3.797 ± 0.170	3.544 ± 0.243	2.732 ± 0.244	4.597 ± 0.219	0.294 ± 0.006	135	2
3.82	0.867 ± 0.230	3.606 ± 0.312	2.663 ± 0.307	4.881 ± 0.281	0.268 ± 0.008	135	2
8.13	...	3.736 ± 0.703	2.563 ± 0.701	5.446 ± 0.561	0.266 ± 0.027	135	2
NGC 708							
-5.43	1.794 ± 0.550	3.631 ± 0.668	2.600 ± 0.670	5.072 ± 0.559	0.317 ± 0.017	0	1
-2.40	1.557 ± 0.309	4.070 ± 0.364	2.752 ± 0.346	6.018 ± 0.322	0.311 ± 0.010	0	1
-0.37	1.665 ± 0.273	3.503 ± 0.335	2.150 ± 0.303	5.708 ± 0.286	0.293 ± 0.009	0	1
1.39	1.713 ± 0.292	3.891 ± 0.327	2.521 ± 0.301	6.006 ± 0.292	0.309 ± 0.009	0	1
4.16	1.557 ± 0.355	3.457 ± 0.395	2.333 ± 0.369	5.120 ± 0.363	0.287 ± 0.011	0	1
8.56	1.627 ± 0.513	2.468 ± 0.783	1.352 ± 0.681	4.506 ± 0.591	0.284 ± 0.019	0	1
-10.05	1.713 ± 0.789	2.774 ± 0.861	1.341 ± 0.680	5.740 ± 0.652	0.326 ± 0.018	40	2
-6.58	2.345 ± 0.533	3.072 ± 0.581	1.956 ± 0.556	4.826 ± 0.453	0.301 ± 0.014	40	2
-4.13	1.922 ± 0.338	3.067 ± 0.315	1.897 ± 0.278	4.960 ± 0.292	0.318 ± 0.008	40	2
-2.42	1.530 ± 0.300	3.449 ± 0.263	2.313 ± 0.238	5.144 ± 0.255	0.335 ± 0.007	40	2
-1.23	1.605 ± 0.294	3.645 ± 0.249	2.386 ± 0.224	5.568 ± 0.239	0.333 ± 0.006	40	2
-0.03	1.695 ± 0.316	3.478 ± 0.258	2.527 ± 0.246	4.786 ± 0.243	0.341 ± 0.007	40	2
1.19	1.695 ± 0.297	3.520 ± 0.268	2.200 ± 0.241	5.632 ± 0.241	0.336 ± 0.007	40	2
2.39	1.204 ± 0.294	3.454 ± 0.266	2.438 ± 0.249	4.893 ± 0.255	0.329 ± 0.007	40	2
3.85	1.107 ± 0.320	3.457 ± 0.289	2.496 ± 0.272	4.787 ± 0.279	0.340 ± 0.008	40	2
7.06	1.340 ± 0.432	3.473 ± 0.407	2.338 ± 0.376	5.159 ± 0.379	0.364 ± 0.010	40	2
-9.50	...	2.989 ± 0.678	1.814 ± 0.605	4.925 ± 0.592	0.274 ± 0.019	130	2
-6.05	1.382 ± 0.322	3.373 ± 0.321	2.103 ± 0.283	5.410 ± 0.304	0.310 ± 0.009	130	2
-3.31	1.641 ± 0.271	3.484 ± 0.252	2.480 ± 0.229	4.893 ± 0.257	0.322 ± 0.007	130	2
-1.85	1.126 ± 0.235	3.755 ± 0.237	2.627 ± 0.219	5.368 ± 0.231	0.321 ± 0.007	130	2
-0.64	1.428 ± 0.252	3.746 ± 0.249	2.760 ± 0.236	5.085 ± 0.241	0.339 ± 0.007	130	2
0.57	1.672 ± 0.269	3.448 ± 0.234	2.501 ± 0.220	4.755 ± 0.227	0.332 ± 0.007	130	2
1.77	1.475 ± 0.261	3.488 ± 0.247	2.403 ± 0.226	5.064 ± 0.240	0.323 ± 0.007	130	2
3.24	0.852 ± 0.217	3.532 ± 0.231	2.467 ± 0.212	5.058 ± 0.227	0.329 ± 0.006	130	2
5.54	1.094 ± 0.263	3.299 ± 0.297	2.314 ± 0.277	4.703 ± 0.284	0.322 ± 0.008	130	2
8.34	...	3.602 ± 0.581	2.303 ± 0.543	5.635 ± 0.489	0.327 ± 0.016	130	2
NGC 712							
-15.11	1.810 ± 0.661	2.834 ± 0.703	2.043 ± 0.689	3.931 ± 0.627	0.259 ± 0.020	95	1
-10.64	1.866 ± 0.258	2.987 ± 0.315	2.090 ± 0.317	4.269 ± 0.254	0.242 ± 0.008	95	1
-6.32	2.056 ± 0.204	3.155 ± 0.239	2.307 ± 0.248	4.314 ± 0.189	0.262 ± 0.006	95	1
-3.98	1.132 ± 0.156	3.093 ± 0.192	2.231 ± 0.199	4.287 ± 0.152	0.256 ± 0.005	95	1
-2.49	1.393 ± 0.141	2.985 ± 0.182	1.975 ± 0.181	4.509 ± 0.138	0.256 ± 0.004	95	1
-1.27	1.892 ± 0.108	3.224 ± 0.141	2.282 ± 0.144	4.554 ± 0.111	0.272 ± 0.003	95	1
-0.40	1.891 ± 0.112	3.329 ± 0.141	2.536 ± 0.145	4.369 ± 0.121	0.265 ± 0.004	95	1
0.21	1.567 ± 0.108	3.400 ± 0.140	2.606 ± 0.142	4.435 ± 0.124	0.265 ± 0.004	95	1
0.82	1.333 ± 0.110	3.446 ± 0.142	2.510 ± 0.138	4.730 ± 0.129	0.269 ± 0.004	95	1
1.69	1.673 ± 0.112	3.149 ± 0.137	2.276 ± 0.130	4.356 ± 0.131	0.258 ± 0.004	95	1
2.91	1.734 ± 0.153	3.427 ± 0.187	2.455 ± 0.175	4.785 ± 0.181	0.259 ± 0.005	95	1
4.40	1.099 ± 0.164	3.255 ± 0.198	2.294 ± 0.182	4.617 ± 0.196	0.260 ± 0.005	95	1
6.75	2.368 ± 0.188	3.152 ± 0.220	2.400 ± 0.203	4.140 ± 0.228	0.245 ± 0.006	95	1
11.25	1.701 ± 0.264	3.068 ± 0.296	2.327 ± 0.271	4.044 ± 0.310	0.246 ± 0.009	95	1
15.77	2.123 ± 0.556	3.117 ± 0.585	2.109 ± 0.562	4.606 ± 0.502	0.253 ± 0.018	95	1
-8.07	1.275 ± 0.440	2.827 ± 0.615	1.841 ± 0.572	4.342 ± 0.542	0.250 ± 0.013	125	2
-5.19	1.519 ± 0.336	2.974 ± 0.373	2.259 ± 0.370	3.916 ± 0.342	0.247 ± 0.009	125	2
-2.64	1.427 ± 0.223	3.093 ± 0.245	2.152 ± 0.237	4.446 ± 0.215	0.265 ± 0.005	125	2
-1.15	1.584 ± 0.341	3.118 ± 0.356	2.295 ± 0.350	4.236 ± 0.322	0.276 ± 0.008	125	2
-0.29	1.611 ± 0.201	3.361 ± 0.210	2.468 ± 0.210	4.577 ± 0.183	0.275 ± 0.004	125	2
0.32	1.888 ± 0.182	3.304 ± 0.221	2.363 ± 0.223	4.619 ± 0.182	0.271 ± 0.004	125	2

TABLE 8—Continued

<i>r</i> [arcsec]	H β [Å]	[MgFe] [Å]	$\langle \text{Fe} \rangle$ [Å]	Mgb [Å]	Mg ₂ [mag]	PA [°]	Run
1.19	1.425 ± 0.201	3.339 ± 0.266	2.478 ± 0.275	4.498 ± 0.218	0.278 ± 0.005	125	2
2.65	1.480 ± 0.234	3.195 ± 0.322	2.236 ± 0.327	4.565 ± 0.255	0.283 ± 0.005	125	2
5.24	0.857 ± 0.304	3.089 ± 0.390	2.196 ± 0.406	4.344 ± 0.295	0.266 ± 0.007	125	2
8.68	1.960 ± 0.446	3.285 ± 0.569	2.635 ± 0.525	4.095 ± 0.603	0.292 ± 0.015	125	2
-7.70	1.630 ± 0.453	3.031 ± 0.551	1.878 ± 0.496	4.891 ± 0.488	0.305 ± 0.015	170	2
-4.77	1.062 ± 0.354	3.575 ± 0.388	2.741 ± 0.375	4.662 ± 0.373	0.298 ± 0.011	170	2
-2.53	0.811 ± 0.168	3.341 ± 0.159	2.671 ± 0.155	4.179 ± 0.155	0.289 ± 0.005	170	2
-0.82	1.661 ± 0.119	3.424 ± 0.109	2.407 ± 0.103	4.871 ± 0.103	0.305 ± 0.003	170	2
0.03	1.627 ± 0.143	3.366 ± 0.157	2.469 ± 0.151	4.590 ± 0.147	0.301 ± 0.004	170	2
0.88	1.207 ± 0.169	3.634 ± 0.201	2.907 ± 0.203	4.542 ± 0.187	0.324 ± 0.005	170	2
2.57	1.719 ± 0.189	3.200 ± 0.217	2.463 ± 0.214	4.156 ± 0.202	0.305 ± 0.006	170	2
4.82	0.825 ± 0.390	3.346 ± 0.447	2.238 ± 0.422	5.002 ± 0.394	0.310 ± 0.013	170	2
8.18	2.017 ± 0.541	3.248 ± 0.572	2.418 ± 0.557	4.362 ± 0.531	0.303 ± 0.017	170	2
NGC 759							
-8.36	1.627 ± 0.346	3.413 ± 0.418	2.775 ± 0.439	4.196 ± 0.365	0.254 ± 0.012	11	1
-5.79	1.076 ± 0.266	3.413 ± 0.332	2.744 ± 0.339	4.245 ± 0.303	0.252 ± 0.009	11	1
-3.56	1.488 ± 0.130	3.076 ± 0.178	2.309 ± 0.162	4.098 ± 0.187	0.238 ± 0.004	11	1
-1.86	2.078 ± 0.097	2.996 ± 0.140	2.107 ± 0.125	4.261 ± 0.146	0.242 ± 0.003	11	1
-1.00	2.105 ± 0.095	3.280 ± 0.139	2.433 ± 0.127	4.423 ± 0.144	0.241 ± 0.003	11	1
-0.39	2.413 ± 0.113	3.273 ± 0.153	2.335 ± 0.139	4.587 ± 0.157	0.235 ± 0.003	11	1
0.22	2.462 ± 0.106	3.090 ± 0.144	2.218 ± 0.131	4.305 ± 0.149	0.233 ± 0.003	11	1
0.82	2.296 ± 0.117	3.000 ± 0.154	2.183 ± 0.149	4.121 ± 0.142	0.243 ± 0.003	11	1
1.69	2.122 ± 0.109	2.933 ± 0.143	2.113 ± 0.138	4.069 ± 0.132	0.244 ± 0.003	11	1
3.15	1.601 ± 0.136	3.048 ± 0.177	2.154 ± 0.168	4.312 ± 0.164	0.252 ± 0.004	11	1
5.00	1.434 ± 0.234	3.374 ± 0.285	2.383 ± 0.286	4.776 ± 0.236	0.269 ± 0.007	11	1
7.32	1.458 ± 0.281	3.776 ± 0.360	2.897 ± 0.372	4.920 ± 0.307	0.264 ± 0.009	11	1
-8.51	1.547 ± 0.488	3.174 ± 0.562	2.232 ± 0.510	4.512 ± 0.568	0.301 ± 0.014	100	2
-5.35	1.699 ± 0.389	3.149 ± 0.453	2.046 ± 0.401	4.845 ± 0.446	0.314 ± 0.011	100	2
-3.08	2.409 ± 0.204	2.952 ± 0.208	2.356 ± 0.201	3.698 ± 0.207	0.282 ± 0.006	100	2
-1.40	2.438 ± 0.158	3.144 ± 0.167	2.323 ± 0.160	4.254 ± 0.159	0.288 ± 0.005	100	2
-0.55	2.279 ± 0.177	3.066 ± 0.184	2.229 ± 0.177	4.216 ± 0.170	0.294 ± 0.005	100	2
0.06	2.166 ± 0.206	3.032 ± 0.222	2.142 ± 0.214	4.293 ± 0.202	0.296 ± 0.006	100	2
0.67	2.465 ± 0.201	3.089 ± 0.226	2.239 ± 0.224	4.263 ± 0.199	0.294 ± 0.006	100	2
1.53	2.256 ± 0.190	3.111 ± 0.224	2.363 ± 0.226	4.094 ± 0.200	0.286 ± 0.006	100	2
3.20	2.167 ± 0.216	3.084 ± 0.259	2.295 ± 0.257	4.144 ± 0.231	0.287 ± 0.007	100	2
5.45	1.043 ± 0.263	2.970 ± 0.417	2.306 ± 0.398	3.826 ± 0.416	0.305 ± 0.010	100	2
7.78	2.125 ± 0.334	3.681 ± 0.553	3.078 ± 0.532	4.401 ± 0.562	0.321 ± 0.013	100	2
-9.56	2.527 ± 0.624	2.822 ± 0.618	1.894 ± 0.570	4.205 ± 0.576	0.264 ± 0.015	145	2
-6.87	1.877 ± 0.441	3.085 ± 0.397	2.354 ± 0.389	4.042 ± 0.373	0.274 ± 0.011	145	2
-4.79	2.363 ± 0.358	3.410 ± 0.323	2.471 ± 0.311	4.705 ± 0.298	0.257 ± 0.009	145	2
-2.92	2.149 ± 0.183	3.135 ± 0.197	2.240 ± 0.179	4.387 ± 0.201	0.250 ± 0.006	145	2
-1.47	1.780 ± 0.147	3.231 ± 0.157	2.327 ± 0.144	4.484 ± 0.160	0.251 ± 0.005	145	2
-0.61	2.224 ± 0.129	3.164 ± 0.148	2.248 ± 0.137	4.452 ± 0.147	0.242 ± 0.004	145	2
-0.00	2.304 ± 0.119	3.006 ± 0.150	2.080 ± 0.137	4.342 ± 0.147	0.250 ± 0.004	145	2
0.60	2.164 ± 0.126	3.154 ± 0.166	2.301 ± 0.154	4.323 ± 0.165	0.266 ± 0.005	145	2
1.47	2.173 ± 0.126	3.206 ± 0.167	2.404 ± 0.157	4.275 ± 0.167	0.268 ± 0.005	145	2
2.93	2.081 ± 0.158	3.203 ± 0.208	2.285 ± 0.191	4.489 ± 0.210	0.280 ± 0.006	145	2
4.78	2.121 ± 0.330	3.523 ± 0.355	2.369 ± 0.330	5.239 ± 0.325	0.307 ± 0.010	145	2
7.10	1.980 ± 0.449	3.583 ± 0.451	2.607 ± 0.433	4.926 ± 0.422	0.296 ± 0.014	145	2
9.81	1.992 ± 0.666	3.180 ± 0.702	2.018 ± 0.637	5.011 ± 0.631	0.282 ± 0.017	145	2
UGC 1308							
-9.41	1.007 ± 0.475	2.158 ± 0.754	1.280 ± 0.673	3.639 ± 0.628	0.232 ± 0.020	28	1
-6.33	0.499 ± 0.317	2.881 ± 0.583	1.880 ± 0.583	4.415 ± 0.417	0.249 ± 0.014	28	1
-3.77	0.851 ± 0.228	3.002 ± 0.416	1.867 ± 0.401	4.827 ± 0.301	0.260 ± 0.010	28	1

TABLE 8—Continued

r [arcsec]	$H\beta$ [Å]	[MgFe] [Å]	$\langle \text{Fe} \rangle$ [Å]	Mgb [Å]	Mg_2 [mag]	PA [°]	Run
-2.30	1.404 ± 0.207	3.513 ± 0.351	2.631 ± 0.370	4.690 ± 0.279	0.268 ± 0.009	28	1
-1.08	0.948 ± 0.178	3.421 ± 0.294	2.410 ± 0.301	4.855 ± 0.229	0.273 ± 0.008	28	1
-0.20	0.950 ± 0.174	3.463 ± 0.291	2.444 ± 0.302	4.907 ± 0.219	0.283 ± 0.007	28	1
0.41	1.334 ± 0.192	3.654 ± 0.332	2.568 ± 0.347	5.200 ± 0.241	0.272 ± 0.007	28	1
1.30	1.886 ± 0.175	3.234 ± 0.284	2.215 ± 0.295	4.721 ± 0.201	0.276 ± 0.007	28	1
2.50	1.356 ± 0.194	3.163 ± 0.354	2.119 ± 0.364	4.721 ± 0.245	0.274 ± 0.008	28	1
3.97	1.837 ± 0.235	3.223 ± 0.420	2.421 ± 0.459	4.291 ± 0.305	0.266 ± 0.010	28	1
7.20	1.368 ± 0.293	3.061 ± 0.544	2.135 ± 0.575	4.389 ± 0.380	0.222 ± 0.013	28	1
10.49	1.158 ± 0.590	3.045 ± 0.876	1.883 ± 0.825	4.926 ± 0.677	0.196 ± 0.025	28	1
-5.59	1.305 ± 0.924	2.613 ± 1.043	1.593 ± 0.941	4.289 ± 0.891	0.249 ± 0.028	28	2
-3.18	1.954 ± 0.405	3.810 ± 0.486	2.705 ± 0.492	5.366 ± 0.394	0.262 ± 0.014	28	2
-1.44	0.832 ± 0.356	3.227 ± 0.400	2.186 ± 0.395	4.764 ± 0.321	0.259 ± 0.011	28	2
-0.26	1.194 ± 0.298	3.798 ± 0.345	2.826 ± 0.355	5.103 ± 0.287	0.254 ± 0.011	28	2
0.92	1.869 ± 0.343	3.914 ± 0.442	2.902 ± 0.453	5.278 ± 0.368	0.277 ± 0.013	28	2
2.81	1.432 ± 0.429	3.517 ± 0.538	2.764 ± 0.562	4.474 ± 0.460	0.281 ± 0.016	28	2
4.67	1.185 ± 0.639	3.632 ± 0.879	2.557 ± 0.781	5.159 ± 0.922	0.295 ± 0.025	28	2
-10.97	1.550 ± 0.532	3.310 ± 0.552	2.639 ± 0.554	4.151 ± 0.512	0.270 ± 0.020	120	2
-5.42	1.268 ± 0.270	3.207 ± 0.340	2.337 ± 0.323	4.400 ± 0.324	0.269 ± 0.011	120	2
-2.88	1.407 ± 0.193	3.520 ± 0.238	2.643 ± 0.231	4.689 ± 0.225	0.265 ± 0.008	120	2
-1.42	1.235 ± 0.153	3.597 ± 0.189	2.701 ± 0.182	4.791 ± 0.181	0.278 ± 0.006	120	2
-0.54	1.291 ± 0.147	3.616 ± 0.192	2.797 ± 0.187	4.674 ± 0.183	0.283 ± 0.006	120	2
0.07	1.325 ± 0.148	3.377 ± 0.203	2.410 ± 0.197	4.730 ± 0.182	0.284 ± 0.006	120	2
0.67	1.172 ± 0.153	3.707 ± 0.219	2.658 ± 0.213	5.170 ± 0.196	0.293 ± 0.006	120	2
1.56	0.785 ± 0.170	3.572 ± 0.253	2.462 ± 0.243	5.180 ± 0.223	0.291 ± 0.007	120	2
2.77	1.801 ± 0.187	3.197 ± 0.258	2.397 ± 0.248	4.263 ± 0.246	0.272 ± 0.007	120	2
4.25	1.283 ± 0.231	3.220 ± 0.327	2.355 ± 0.313	4.403 ± 0.309	0.264 ± 0.009	120	2
6.00	1.091 ± 0.314	2.969 ± 0.376	2.202 ± 0.367	4.004 ± 0.346	0.234 ± 0.008	120	2